UNIVERSITY OF EXETER

DOCTORAL THESIS

Time resolved and time average imaging of magnetic nano-structures

---

Author:
Erick Omar Burgos Parra

Supervisor:
Prof. Robert J. Hicken
Prof. Feodor Ogrin

A thesis submitted in fulfillment of the requirements
for the degree of Doctor of Philosophy in Physics

in the

EPSRC Centre for doctoral training in metamaterials
Department of Physics and Astronomy

August, 2018

TIME RESOLVED AND TIME-AVERAGE IMAGING OF MAGNETIC NANO-STRUCTURES

Submitted by Erick Omar Burgos Parra to the University of Exeter as a thesis for the degree of Doctor of Philosophy in Physics, August 2018 This thesis is available for Library use on the understanding that it is copyright material and that no quotation from the thesis may be published without proper acknowledgement.

I certify that all material in this thesis which is not my own work has been identified and that no material has previously been submitted and approved for the award of a degree by this or any other University.

Erick Omar Burgos Parra
August, 2018

"Do. Or do not. There is no try."

Yoda

Acknowledgements

I could have easily finished this thesis one week before the time that I did, but I'm terrible at sitting behind a desk for more than 20 minutes straight. Even more so if there are more interesting things to do like new experiments, travelling to conferences or just hanging out with my wife. However, as a certain spider said, "great power comes with great responsibility". And I believe that I have a great power: the power to change things. I can make people happy if they have had a bad day, I can help others with my words or my actions if they are struggling, I can make people think about the world that surronds them while I teach them science. I have the power to push further, the edges of that small sphere that we call "knowledge" (although I don't know if I actually "know" something). I feel that I even have the power to change this society! I would love to do that. But every idea needs a plan to become more than an idea. And a plan needs to be divided into steps to be accomplished. Once all the steps are completed, then and only then an idea stops being an idea and becomes a reality. And the next step in my plan is getting my PhD, so here I'm, writing this thesis.

There is plenty, lots and lots of people that I would like to thank. Without them I would not have been able to be where I'm now. Some of them have names, some of them are faceless: from those men or women that work tirelessly around the city so I can get food, medicine, beer and all the commodities that I *need* so I *just* have to worry about studying and do my research, to those who were crucial in my formation as a scientist, such as Kremer, Moraga, Fuenzalida, Muñoz, Flores, Morales, Dinator and so many others than I can't remember now. To all of them who are part of this not usually fair and not constantly rewarding system, thank you very much.

I would like to acknowledge several people in particular. To begin with I would like to thank my PhD supervisors, Rob Hicken and Feodor Ogrin. Their advice, wisdom and constant support has been crucial for me and for the success of my studies during these four years. Both have being incredibly important to my development as a scientist and the cornerstone of all my achievements during my PhD. Thank you very much for all that you have taught me.

I would also like to thank to all the staff that helped me make the experiments presented in this thesis possible. The most important after my supervisors is Dr. Paul Keatley. He is one of the most friendly and smart scientists than I know. Without his knowledge and support during my first years, I would not have been able to even start working on my project. Thank you very much for being such a good person, academia needs more people like you. I also want to thank Dr. Nicolas Jaouen and Dr. Horia Popsecu from SOLEIL synchrotron, Dr. Flora Yakhou-Harris from the European Synchrotron Radiation Facility (ESRF), and Dr. Adriana Figueroa and Professor Gerrit van der Laan from Diamond light source. All of these are amazing facilities to do science. Their support was key to the success of our beamtimes and made those 120 hours of work per experiment easier to endure.

I have made really good friends during this PhD and I would like to thank them all for being there at the right time and at the right place. Thank you for all those amazing conversations about politics, music, food, taboo topics and those plenty of well-used hours laughing on memes, partying or just bathing in the sun (whenever the sun decided to come out): Sathya, Lauren, Christopher and Rayko. A special mention to Nick with whom besides all the other things mentioned before, I spent more or less two months doing experiments at synchrotrons around Europe. Man, those days would have been really long without you there. Thank you for all the *yeeeeeee*.

I have a special place in my heart for those who have shared the house with me at some point during these years: Santiago, Henry, Cony, Alba, Sergio, Sathya and Nithya. It is not easy to move house (and country) so it is better when you share the place where you live with those that you love. These guys have been my family and they will always be, no matter where we are. I will be always be thankful for all the joy that you have brought into my life.

Quiero agradecer eternamente a mi madre, quien ademas de haberme dado la vida y los recursos para ser el hombre que soy, me ha dado su apoyo incondicional para realizarme profesionalmente. No existe un hijo más agradecido en el mundo que yo. También a mi hermana por ser uno de mis más importantes pilares en la vida y luchar mirando de frente a todas las adversidades de la vida. No tendré jamás la mitad de tu fortaleza ni con todos los titulos del mundo. Gracias por existir. Y a mi Peti, gracias por la vida, la que nos diste y la que nos enseñaste.

Finally, I want to thank my wife, best friend and the love of my life Gloria. Since the beginning of this journey she has been there, supporting me through thick and thin. Without you here, all this would have been much, much more difficult. Thank you for all your love and support during these four years. You complete me and make me a better person every day. Together we can face any challenge, make any idea real. And for that, I will always be thankful.

Contents

List of Figures

List of Tables

To the love of my life and best friend, Gloria.

Chapter 1

Introduction

The ability of a ferromagnet to maintain its magnetic state in the absence of an external magnetic field has made ferromagnetic materials an important subject of study in physics since the end of the 19^{th} century. Moreover, ferromagnetic materials are the cornerstone for data storage systems such as magnetic tapes, magnetic disk drives and magnetic random access memory. The discovery of the Giant Magneto Resistance (GMR) in 1988 suggested that, since the magnetic state of the electrical conductor has an important effect upon the current flow, there may also be an inverse influence of the current upon the magnetization. In this effect, predicted in 1989 [1] by Slonczewski and called Spin Transfer Torque, angular momentum transferred by a spin polarized current can exert a torque on the magnetization of a ferromagnetic material, changing the local magnetization and stimulating the precession of the magnetic moments, generating microwave signals. This provides a new method of manipulating magnetization without applying an external field. Large polarized currents lead to spin transfer effects which are the driving force for the magnetic dynamics of devices known as Spin Transfer Oscillators (STO). In this new kind of nano-device the emission of microwaves is stimulated by a DC electrical current and measured as a change in the output voltage due the GMR effect. The specific characteristics of these devices such as working frequency and DC current ranges, microwave emission linewidth, and maximum emission power among others, are given by the design and size of the device, and the nature of the magnetic oscillations producing the emission.

Among the multiple types of STO that now exist , I have focused my research upon three of them: Spin Transfer Vortex Oscillators (STVO), Single Layer Spin Transfer Oscillators (SL-STO) and Orthogonal Pseudo Spin Valves. Within STVOs and SL-STOs we can nucleate what is called a magnetic vortex. A magnetic vortex is a curling of the in-plane of a magnetic layer with its centre pointing out of the magnetization plane. The gyration of this vortex due to STT produces a microwave emission < 1GHz with a greater emission power than that produced by the precession of magnetic moments in STOs. The phase-locked synchronisation of multiple vortices is expected to exhibit enhanced microwaved power and phase stability compared to a single vortex device, providing a solution to the drawbacks of the STO in the low frequency regime. On the other hand, Orthogonal Pseudo Spin Valves promote the nucleation of magnetic dissipative solitons, also called magnetic droplets. This type of magnetic structure has an opposite out of plane magnetization to the layer that contains it. Compared to the microwave emission of magnetic vortices , magnetic droplets have a higher frequency range and emission power. However, their nucleation is subject to large external fields being applied to the sample.

In this thesis, I electrically characterized these devices and applied magnetic imaging techniques in order to go further in the understanding of the spatial features and dynamic behaviour of these magnetic structures. It is not possible to acquire this knowledge by only using electrical characterization. Understanding the magnetization dynamics in these devices is crucial for the design of STO based devices while imaging studies are required to prove the existence of these magnetic structures, as in case of the magnetic droplet.

In chapter 2 I will introduce the background concepts of magnetism that are relevant to this thesis. I will go from the basics principles of ferromagnetism, its quantum mechanical treatment, and the theory that explain the dynamics of the magnetisation. I will also present the state of the art in experimental research in the field of spin transfer oscillators. My aim is to give the basic background needed to understand the results presented in this thesis.

In chapter 3 I will introduce the two main experimental techniques used for imaging the magnetisation of the devices presented: Holography with Extended Reference by Autocorrelation Linear Differential Operator (HERALDO) and Time Resolved Scanning Kerr Microscopy (TRSKM). I will revise the theoretical background concepts and the development of the techniques in order to demostrate the uniqueness of each technique and how they were used in this thesis. It is interesting to note that while MOKE is a well-known and widely-used technique, far fewer laboratories in the world area able to perform time resolved measurements using MOKE, with the University of Exeter being one of them. Furthermore, HERALDO is a novel technique that is used for the first time to image magnetic structures within multilayer systems in this thesis, which is a milestone in the development of the techinque.

In chapter 4 I present an investigation of the magnetization dynamics of a SL-STO. Electrical transport measurements provided an initial characterization of the device. We then used HERALDO for the first time to investigate the magnetization dynamics in an intermediate layer of a multilayer stack. We present time averaged measurements of the magnetisation of a magnetic vortex formed underneath a nano contact (NC) positioned on top of the multilayer, using a combination of x-ray holography and x-ray magnetic circular dichroism. The results presented in this chapter have been published [2].

In chapter 5 I present the first direct measurement at the time of a magnetic dissipative droplet, using holography with extended reference autocorrelation by linear differential operator (HERALDO). I studied the out of plane magnetisation of the free layer under a NC within an orthogonal pseudo spin salve. The results presented in this chapter have been published [3]

In chapter 6 I present and study STVO devices with pairs of NCs of 100 nm diameter and centre-to-centre separation D = 200 to 1100 nm, by a combination of electrical measurements and time-resolved scanning Kerr microscopy (TRSKM). It will be shown that the dynamic behaviour of vortices and anti vortices changes when the distances between the NCs within the devices is changed.

Chapter 2

Theoretical Background and literature review

2.1 Ferromagnetism: a basic approach

A ferromagnetic material differs from a diamagnetic or paramagnetic material by the way in which the dipole moment per unit volume, called the *magnetisation* $\vec{M}$, may be non-zero when the applied magnetic $\vec{H} = 0$. In other words it may possess a spontaneous magnetisation. For modest applied fields the magnetisation of a paramagnetic or diamagnetic material is linearly proportional to $\vec{H}$, while for a ferromagnetic material, in general:

$$\vec{M} \neq \chi \vec{H}. \tag{2.1}$$

Actually, for a ferromagnet, $\vec{M}$ is not even a single-valued function of $\vec{H}$, and its value depends on the history of the applied field. If we plot the component of $\vec{M}$ in the direction of $\vec{H}$ as a function of H we will obtain a *hysteresis loop* as shown in Fig. 2.1.

At higher values of the applied field, the magnetisation tends towards the *saturation magnetisation*, M_s. This is the maximum or minimum value of $\vec{M}$ (depending on the direction of $\vec{H}$), and in this state, all the magnetisation lies parallel to the external field.

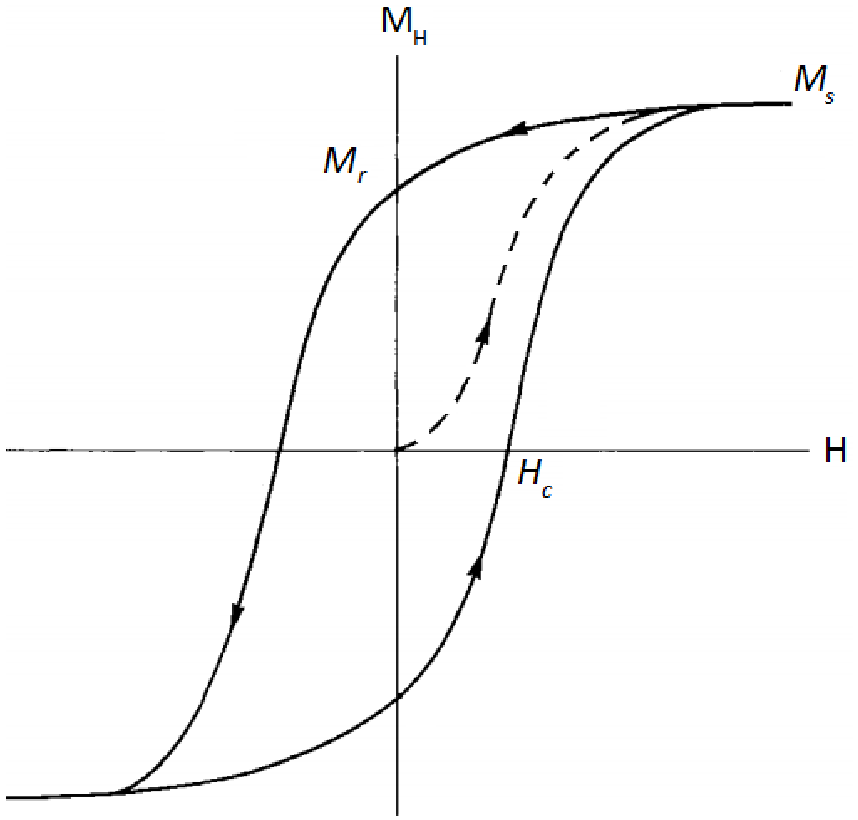

FIGURE 2.1: Schematic representation of the *limiting* hysteresis curve of a typical ferromagnetic material, displaying also the virgin curve (dashed). Also shown are the remanence, M_r, the saturation magnetisation, M_s, and the coercivity, H_c. Reproduced and modified from [4].

If we set $\vec{H} = 0$, the value of $\vec{M}$ will in general be non-zero. This value of $\vec{M}$ is called the *remanent magnetisation*. In order to obtain $\vec{M} = 0$ it is necessary to apply a field, called the *coercivity* or *coercive force*, in the direction opposite to that used to saturate the magnetisation of the sample. Materials with high coercivity are magnetically *hard* while those with low coercivity are magnetically *soft*.

The coercive field can change from sample to sample and its value depends upon how fast the external field is swept [6], the anisotropy of the sample [7, 8], or the quantity of material [9] among other factors. On the other hand, the saturation magnetisation is an intrinsic property of the material and does not depend on the sample characteristics. However, M_s depends strongly upon the temperature. A figure of M_s as a function of temperature for most ferromagnetic materials is plotted in Fig.2.2. T_c is the

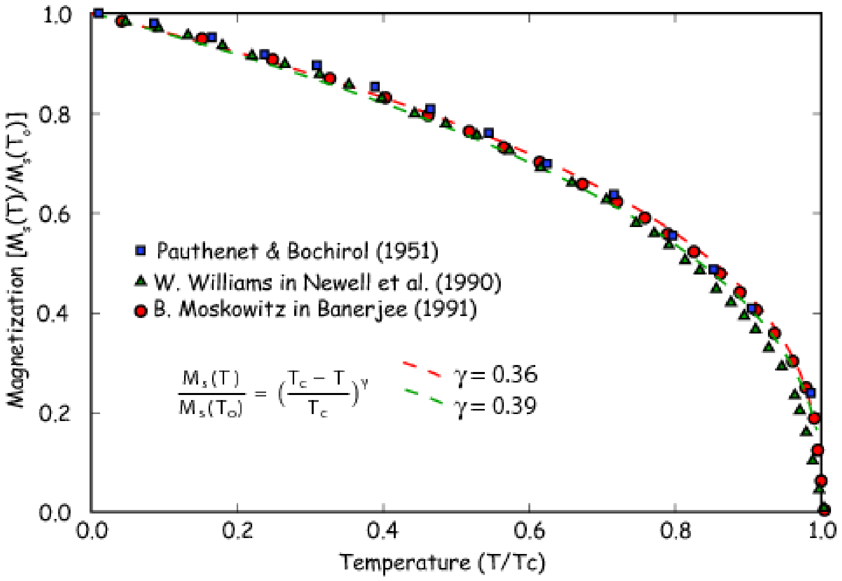

FIGURE 2.2: Saturation magnetisation as a function of temperature. M_s is normalized with respect to the value at zero temperature. The temperature is normalized to T_c value for the the material. When plotted this way, all ferrromagnets seem to exhibit a similar temperature dependence. (from [5])

so-called *Curie Temperature* and is the temperature at which $M_s = 0$ for zero external field. For temperatures greater than T_c a ferromagnet behaves as a paramagnet and its magnetisation depends upon the applied field.

In an attempt to explain this behaviour, Weiss in 1907 [10] proposed a theory that explained both the hysteresis behaviour and the temperature dependence. He assumed the presence of a molecular field within the ferromagnetic material that aligns the dipole magnetic moments against the randomizing influence of thermal fluctuations. This explains the temperature dependence of the magnetisation. Above the Curie temperature, the thermal fluctuations are sufficiently large so as to misalign the magnetic moments and lead to zero magnetisation of the sample. However, this does not explain why the magnetisation depends strongly on the *history* the applied field. To explain this, Weiss assumed the existence of *domains* in the ferromagnetic material, formed by magnetic moments that align in the same direction. Each domain has magnetisation equal to the M_s value, but not all the domains have their magnetisation pointing in the same direction. In fact, the total magnetisation of the sample is the *average* of the domain magnetisation in the direction in which the magnetisation is measured. At zero field, for a demagnetized material, the average of the magnetisation is zero. At constant temperature, an increase in the applied field will increase the alignment of the domains in the field direction until saturation is achieved, where the domains all have magnetisation parallel to the external field. In order to demagnetize the sample again, it is not sufficient to turn off the external field, because this "molecular" field will keep the magnetic moments aligned. Rather it is necessary to apply a finite field in the opposite direction, called the coercive field, to disorder the magnetisation of the domains and return the sample to a demagnetized state. All these assumptions were stated by Weiss without any justification or explanation of the origin of the molecular field, or of how the domains form. Although many difficulties arose in quantitative calculations when these qualitative premises were applied, back in the early 20^{th} century, now these assumptions are well accepted facts and are the underlying principles of the theory of ferromagnetism. The force which acts to align the spins is now known as the *exchange interaction*, while magnetic domains have been clearly observed by many means.

2.2 Classical approximation

Ferromagnetism is by nature a quantum mechanical effect, and so a quantum theoretical treatment should lead to correct and experimentally observed results. However, it is possible to make semi-classical approximations and in some cases this is the only feasible choice. Within this context, we now review some basics concepts of the quasi-classical theory of ferromagnetism.

2.2.1 Paramagnetism

In the words of Aharoni [11] :"It is necessary to understand paramagnetism before trying to understand ferromagnetism", so let us take a look to the quasi-classical theory of paramagnetism. We start by considering an ensemble of atoms, where each atom has a fixed magnetic moment $\vec{m}$ with magnitude given by

$$m = g\mu_B S\,, \tag{2.2}$$

where g is the spectroscopic splitting factor, S the spin quantum number and μ_B is known as the *Bohr magneton* and is given by

$$\mu_B = \frac{|e|\hbar}{2m_e c}\,. \tag{2.3}$$

At applied field $\vec{H}$ the magnetic moments interact with this field with energy $-\vec{m}\cdot\vec{H}$ but not with each other. Let us choose a field applied in the $\hat{z}$ direction, so that the average moment parallel to the $\hat{z}$ direction at temperature T is given from statistical mechanics by

$$\langle m_z \rangle = \frac{\sum m_z e^{m_z \beta H}}{\sum e^{m_z \beta H}}\,, \tag{2.4}$$

with $\beta = 1/K_B T$. Knowing that S_z can take values from $-S$ to S in integer or half-integer steps, the eq. (2.4) can be rewritten as

$$\langle S_z \rangle = \frac{\langle m_z \rangle}{g\mu_B} = \frac{\sum_{n=-S}^{S} g\mu_B n e^{g\mu_B \beta H n}}{\sum_{n=-S}^{S} e^{g\mu_B \beta H n}}\,. \tag{2.5}$$

The result of the summation within eq. (2.5) is an exercise solved in dozens of books [11] and the solution is

$$\frac{\langle S_z \rangle}{S} = \frac{2S+1}{2S}\coth\left(\frac{2S+1}{2S}\eta\right) - \frac{1}{2S}\coth\left(\frac{\eta}{2S}\right) = B_S(\eta). \tag{2.6}$$

with $\eta = g\mu_B SH/K_B T$. $B_S(\eta)$ in equation 2.6 is called the *Brillouin function*. For small values of the argument

$$\cosh x = \frac{1}{x} + \frac{x}{3} + \mathcal{O}(x^3). \tag{2.7}$$

Therefore, eq. (2.6) becomes

$$B_S(\eta) = \frac{S+1}{3S}\eta + \mathcal{O}(x^3). \tag{2.8}$$

In this way and for values of H that are not too large, the average value of the magnetisation in the direction of the field is

$$\langle m_z \rangle = g\mu_B \langle S_z \rangle = \frac{(g\mu_B)^2 S(S+1)}{3k_B T} H. \tag{2.9}$$

In eq. (2.9) the magnetisation is linear in the field, as is the case for most paramagnets. The susceptibility is defined as

$$\chi = \frac{\partial \langle M_z \rangle}{\partial H} = \frac{N \partial \langle m_z \rangle}{\partial H} = \frac{(g\mu_B)^2 S(S+1)}{3k_B T} \tag{2.10}$$

where N is the number of spins per unit volume. The dependence of χ upon the temperature is known as the *Curie law* which agrees with the experiments for all known paramagnets. If we consider large fields, $B_S(\pm\infty) = \pm 1$ which means that the magnetisation saturates and does not increase further with the field. Nevertheless, a sufficiently large value of H is usually not available for this region to be reached at room temperature.

So far, we have described paramagnetism and we have proved the linear dependence of the magnetisation upon the field and that the susceptibility is independent of H for values of H that are not too high. Although χ may depend upon H in some paramagnets, $\chi(H)$ is a well-defined, single-valued function and does not depend of the history on H as in ferromagnets.

2.2.2 Ferromagnetism

Let us now consider the interaction between atomic spins in magnetic materials. Through this interaction each spin tries to align other spins in its own direction. This is the case for *ferromagnetic* materials. This interaction, called the *exchange interaction*, can be described by an *exchange energy* proportional to $\vec{S}_i \cdot \vec{S}_j$ between spin $\vec{S}_i$ and spin $\vec{S}_j$. If we apply an external field $\vec{H}$, the total energy of the system is thus

$$E = -\sum_{ij,i\neq j} J_{ij}\vec{S}_i \cdot \vec{S}_j - \sum_i g\mu_B\vec{S}_i \cdot \vec{H}\,. \tag{2.11}$$

The coefficients J_{ij} are called the *exchange integrals* and their sign defines the type of interaction between the spins: for positive values of J_{ij}, parallel spins have lower energy than antiparallel spins and vice versa. In ferromagnetic materials $J_{ij} > 0$ and in antiferromagnetic materials, $J_{ij} < 0$. Due to the nature of the system, an ensemble of atoms, many bodies are involved and it is necessary to approximate the interaction between spins by introducing a *mean field approximation*. This method consists of choosing one arbitrary spin and considering its statistics in more detail while the values of the other spins are just replaced by their mean value. After making some calculations for this *special* spin, we go a step back and say that on average this special spin is no different from the others, thus we may obtain the value of the mean field. Let us consider $\vec{S}_i$ to be the special spin and replace all the other $\vec{S}_j$ spins by their mean value, $\langle S_j\rangle$. Thus

$$E = -2\sum_j J_{ij}\vec{S}_i \cdot \langle\vec{S}_j\rangle - \sum_i g\mu_b\vec{S}_i \cdot \vec{H} = -\vec{S}_i \cdot \vec{H}_i\,, \tag{2.12}$$

where

$$\vec{H}_i = 2\sum_j J_{ij}\langle\vec{S}_j\rangle + g\mu_B\vec{H}\,. \tag{2.13}$$

As we can see, the exchange interaction between the spins is now equivalent to an interaction of each spin with an effective field $\vec{H}_i$, which is non zero even when the external field $\vec{H}$ vanishes. We have transformed the problem of interacting spins to isolated spins interacting with an applied field, which is the problem of paramagnetism treated previously. With appropriate normalisation, the z-component of $\vec{S}_i$ is seen to become

$$\langle S_{iz} \rangle = SB_s \left(\frac{SH_i}{k_B T} \right) , \tag{2.14}$$

where H_i is defined in eq. (2.13) and $B_s(x)$ is the Brillouin function. Now, if we take S_i to be a spin that is no different to the other spins within the summation in eq. (2.13), then there is no reason to use i and j to label the spins and eq. (2.14) becomes

$$\langle S_z \rangle = SB_s \left(\frac{S}{k_B T} \left[2 \langle S_z \rangle \sum_j J_{ij} + g \mu_B H \right] \right) . \tag{2.15}$$

The last assumption that we need to make is that $J_{ij} = 1$ for spins which are nearest neighbours in the crystal, and $J_{ij} = 0$ otherwise. Therefore, if p is the number of nearest neighbours, we can re-write the transcendental eq. (2.15) as

$$\frac{\langle S_z \rangle}{S} = B_s \left(\frac{g \mu_B S H}{k_B T} + \left[\frac{2S^2}{k_B t} pJ \right] \frac{\langle S_z \rangle}{S} \right) . \tag{2.16}$$

So far we have described the magnetisation of a ferromagnetic material in an external magnetic field H. If $H = 0$, there is no direction in space that defines the z-axis. It is then sufficient to assume that $H = 0$ is the end of a process in which a finite field is applied, and then slowly reduced to zero, which is the usual experimental process.

2.2.3 Quantum approach and exchange integrals

The magnetism in magnetic materials arises from two contributions to the magnetic moment of the atom, those due to the orbital angular momentum and the intrinsic spin angular momentum of the electrons. As defined in eq. (2.2) the magnetic moment includes the spectroscopic splitting factor (Landé factor in atomic physics) g

$$g = 1 + \frac{J(J+1) + S(S+1) - L(L+1)}{2J(J+1)}, \tag{2.17}$$

where for a pure spin contribution $L = 0$, $J = S$ and therefore $g = 2$, which is twice the value for a purely orbital contribution where $S = 0$, and $J = L$. In most ferromagnets, the orbital contribution is negligibly small because electric fields within the lattice orient the plane of the orbits with crystallographic directions making L_z average to zero or almost zero. The unfilled orbitals in the d-shell in the transition metals and in the f-shell in the rare earth contain the spin which dominates the magnetic moment and is responsible for the ferromagnetism.

There is a direct interaction between spins associated with ions at the lattice sites for which there is no classical analogue. This interaction arises from the overlap of the electronic wave functions which describe the electrons in quantum mechanics. Consider a system of N electrons which are bound to M atoms. The eigenfunction for the i-th electron with $\boldsymbol{\rho}_j$ coordinates (with the spin included in these coordinates) bound to the j-th atom will be $\varphi_i(\boldsymbol{\rho}_j)$. In order to write down the eigenfunction that describes all the N electrons, we must consider the Pauli exclusion principle. To achieve, this the eigenfunction should be anti-symmetric with respect to the interchange of two of the electrons. The linear combination with this property is

$$\psi = \frac{det[\varphi_k]}{\sqrt{N!}}\,. \tag{2.18}$$

It is assumed that the set of eigenfunctions φ_i is orthonormal. It is also assumed that the electrons of the inner shells are tightly bound to their nuclei, and only the wave functions of the electrons in the outer shell interact with each other. Therefore, the Hamiltonian of the system of N electrons is

$$\mathcal{H} = \sum_{i=1}^{N} \mathcal{H}_i + \frac{1}{2} \sum_{i,j\&i\neq j}^{N} \frac{e^2}{r_{ij}} + \mathcal{H}_c\,, \tag{2.19}$$

where $\mathcal{H}_c$ is the Hamiltonian operating on the ion cores, r_{ij} is the distance between electrons i and j and

$$\mathcal{H} = -\frac{\hbar^2}{2m_e}\nabla^2 + V_i\,. \tag{2.20}$$

With the equations 2.19 and 2.18, the energy of the system can be written as

$$\mathcal{E} = \int \psi^* \mathcal{H} \psi d\tau_1 d\tau_2 \ldots d\tau_N = \frac{1}{N!} \int det[\varphi_{k'}]^* \mathcal{H} det[\varphi_k] d\tau_1 d\tau_2 \ldots d\tau_N \tag{2.21}$$

$$\begin{aligned}\mathcal{E} &= \frac{1}{N!} \sum_{i=1}^{N} \int det[\varphi_{k'}^*] \mathcal{H}_i det[\varphi_k] d\tau_1 d\tau_2 \ldots d\tau_N \\ &+ \frac{1}{2} \sum_{i,j\&i\neq j}^{N} \frac{1}{N!} \int det[\varphi_{k'}^*] \frac{e^2}{r_{ij}} det[\varphi_k] d\tau_1 d\tau_2 \ldots d\tau_N \\ &+ \frac{1}{N!} \int det[\varphi_{k'}^*] \mathcal{H}_j det[\varphi_k] d\tau_1 d\tau_2 \ldots d\tau_N\end{aligned} \tag{2.22}$$

After some calculations and taking into account some properties of the determinant and the orthogonality condition given by

$$\int \varphi_i^*(\boldsymbol{\rho}_l) \varphi_j(\boldsymbol{\rho}_l) d\tau_k = \delta_{ij} \tag{2.23}$$

where δ_{ij} is the Kronecker symbol, we can write the energy of the electrons outside the core as

$$\begin{aligned}\mathcal{E} =& \sum_{k=1}^{N} \frac{1}{N!} \int \varphi_k^*(\boldsymbol{\rho}_1)\mathcal{H}_1\varphi_k(\boldsymbol{\rho}_1)d\tau_1 \\ &+ \frac{1}{2}\sum_{k,k'=1\&k\neq k'}^{N} \int |\varphi_k^*(\boldsymbol{\rho}_1)|^2\frac{e^2}{r_{ij}}|\varphi_{k'}(\boldsymbol{\rho}_1)|^2 d\tau_1 d\tau_2 \\ &- \frac{1}{2}\sum_{k,k'=1\&k\neq k'}^{N} \int \varphi_k^*(\boldsymbol{\rho}_1)\varphi_{k'}^*(\boldsymbol{\rho}_2)\frac{e^2}{r_{ij}}\varphi_k^*(\boldsymbol{\rho}_1)\varphi_{k'}^*(\boldsymbol{\rho}_2)d\tau_1 d\tau_2\end{aligned} \tag{2.24}$$

Let us analyse the eq. (2.24). The first term represents the energy of the electrons when they are separated from each other and do not interact. The second summation is the Coulomb interaction between a pair of electrons, summed over all the pairs. The final summation is called the *exchange energy* term and the integrals which appear within it are called the *exchange integrals*. Note that this last summation can be considered as a correction to the classical Coulomb interaction and arises from the quantum nature of the electrons and the Pauli principle.

The eq. (2.24), plus the term which accounts for the electrons in the ion cores, can fully describe the electrons in the atoms and their behaviour, but the integrals can be evaluated only if all the functions $\varphi_k(\boldsymbol{\rho}_i)$ are known, which is hardly ever the case. It is not the aim of this review to go further into the calculations of these integrals, rather the aim is to explain where the exchange interaction between the spins comes from. The importance of the computation of exchange integrals lies in the fact that in general, for almost any reasonable assumption about the values of the functions φ_i, the computation leads to a negative exchange integral even when it is known from experiments that for Fe, Co and Ni (ferromagnetic materials) the value must be positive. The first calculations made taking, for example, the eigenfunctions of Cr and Fe (nearly the same) the calculation yields the same sign [12] even though for Cr the sign must be negative and for Fe positive. Further calculations [13] already have yielded the right sign, but the magnitude of the exchange integral still differs considerably from the experimental value. In these days, it is still a big computational effort to calculate this exchange integral accurately and the state of the art research aim to develop the codes using Density Functional Theory and many-body methods [14]

2.3 Magnetics Domains

As said before, the existence of magnetic domains is a well established fact since they have been observed by numerous techniques. For instance, when polarised light is reflected from a magnetised surface, its plane of polarisation is observed to change and detection of the polarisation change can reveal the different orientations of the magnetisation at the surface within the various domains. This is the called the Magneto Optical Kerr Effect (MOKE) [15]. Scanning optical microscopy [16] can be used to increase the resolution of the MOKE. Alternatively, to study these domains with almost atomic scale resolution, scanning electron microscopy with polarised electrons [17] and magnetic force microscopy [18] may be used.

Regardless of the fact that domains exist, the reason for their existence cannot be obtained from the Heisenberg Hamiltonian itself because this is isotropic and real magnets are not. If no other energy besides the isotropic Heisenberg Halmitonian exists, it would have been impossible to measure any magnetism in zero field applied, which clearly contradicts the most basic experiments in ferromagnetic samples. Thus, along with the exchange energy, it is necessary to introduce other types of energies as *magnetoelastic*, and *anisotropy energies*. The domain structure on a ferromagnet arise fundamentally from the balance of these energies.

2.3.1 Magnetostatic energy

The magnetostatic energy arise from the magnetostatic interactions, which represent the way the magnetic moments interact within the entire magnetic body. The magnetostatic field $\vec{H}_m$ at a given location within the body depends on the contributions from the whole magnetisation vector field and an appropriated $\vec{H}_m$ can be obtained from the Maxwell equations for a magnetized medium

$$\nabla \cdot \vec{H}_m = -\nabla \cdot \vec{M} \quad \text{in}\, \Omega\,, \tag{2.25}$$

$$\nabla \cdot \vec{H}_m = 0 \qquad\qquad \text{in}\, \Omega_c\,, \tag{2.26}$$

$$\nabla \times \vec{H}_m = 0\,, \tag{2.27}$$

with the following conditions at the body discontinuity surface $\partial\Omega$

$$\vec{n} \cdot \left[\vec{H}_m\right]_{\partial\Omega} = \vec{n} \cdot \vec{M}\,, \tag{2.28}$$

$$\vec{n} \times \left[\vec{H}_m\right]_{\partial\Omega} = 0\,, \tag{2.29}$$

where $\vec{n}$ is normal to the boundary $\partial\Omega$ of the sample, and $\left[\vec{H}_m\right]_{\partial\Omega}$ is the jump of the vector field $\vec{H}_m$ across $\partial\Omega$. Then, the energy density of the magnetostatic field is given by

$$E_m = \int_{\Omega_{\text{inf}}} \frac{1}{2}\mu_0 \vec{H}_m \cdot \vec{H}_m dV\,, \tag{2.30}$$

where Ω_{inf} refers to the whole space. Taking the magnetostatic field composed by the applied field $\vec{B}_m$ and the magnetisation field $\vec{M}$

$$\vec{H}_m = \frac{\vec{B}_m}{\mu_0} - \vec{M}\,, \tag{2.31}$$

eq. (2.30) becomes

$$E_m = \int_{\Omega_{\text{inf}}} \frac{1}{2}\mu_0 \vec{H}_m \cdot \left(\frac{\vec{B}_m}{\mu_0} - \vec{M}\right)\,. \tag{2.32}$$

The first term of equation (2.30) vanishes owing to the integral orthogonality of $\vec{B}_m$ and $\vec{H}_M$. Thus, the magnetostatic free energy is given by:

$$E_m = -\frac{1}{2}\mu_0 \int_{\Omega_{\text{inf}}} \vec{M} \cdot \vec{H}_m dV \,. \tag{2.33}$$

The magnetostatic energy term is mainly responsible for the existence of the magnetic domains and it *prefers* the subdivision of a ferromagnet into domains. A theoretical demostration of this fact is nicely presented in reference [11]. Figure 2.3 shows how, in order to minimize the magnetostatic energy, a single domain divides into smaller domains. In the Figure 2.3 (a) the exchange energy is minimized as all the magnetic moments in the atoms are aligned in the same direction, but the magnetostatic energy is large. Reducing the size of the domains by half and introducing opposite directions for the magnetisation in neighbouring domains (Figure 2.3 (b)) there is a decrease in the magnetostatic energy but an increase in the exchange energy since the magnetisation is not uniform within the domain wall. This division of the domains will continue until the increase in the exchange energy exceeds the reduction of the magnetostatic energy. The lowest energy configuration of the domains occurs for a closure domain state which is shown in Figure 2.3 (d).

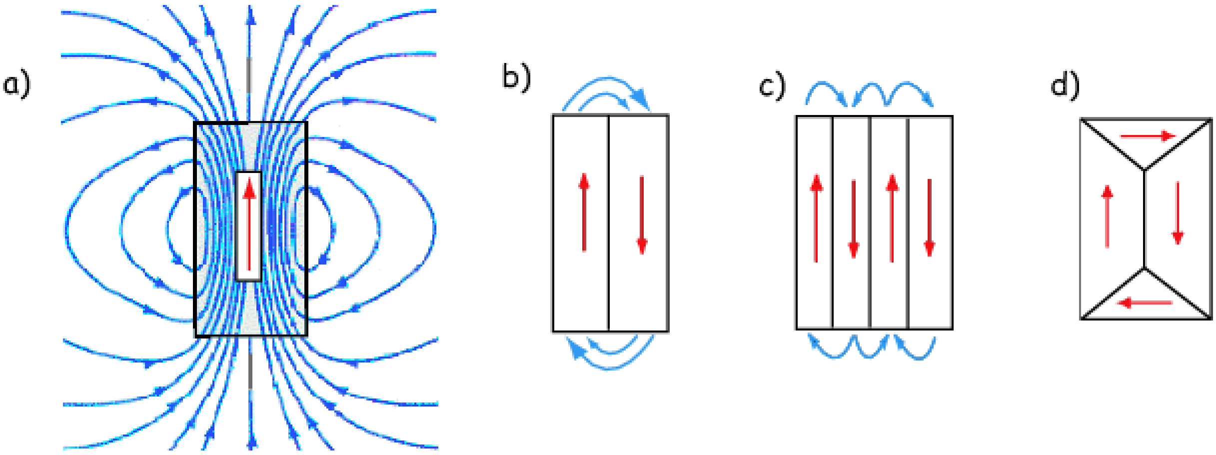

FIGURE 2.3: Magnetic domains. In (a) the magnetisation is saturated in the direction of the red arrow. In this case, the exchange energy is minimal while the magnetostatic energy is large due the magnetic surface charge. In order to reduce the magnetostatic energy magnetic domains appear in the material as shown in (b) and (c). The reduction in the magnetisation energy competes with the increasing exchange energy due the formation of the walls between the domains. This competition limits the formation of the domains. (d) Closure domains act to minimise the magnetostatic energy by eliminating the magnetic surface charge. (from [4])

2.3.2 Anisotropy Energy

Let us take a single-crystal ferromagnet with cubic symmetry, without defects. The *magnetocrystalline* anisotropy is the preferential alignment of atomic magnetic moments along a particular crystal direction, which arises from coupling between the orbital and spin momentums [19]. This direction is called *easy axis* and therefore the other axes are called *hard axes*. As an illustrative example, the anisotropy energy E_a per unit volume for a cubic crystal is given by

$$E_a = K_1 \left(\alpha_1^2 \alpha_2^2 + \alpha_2^2 \alpha_3^2 + \alpha_3^2 \alpha_1^2 \right) , \tag{2.34}$$

where K_1 is a constant known as anisotropy constant, and α_1 , α_2 , and α_3 are the cosines of the angles made by the magnetisation vector with the crystal axes x, y, and z. Figure

2.4 (from [20]) shows the value of the cubic magnetic anisotropy, K_1, at room temperature for different compositions of Fe in an= 3 nm layer of an alloy called Permalloy (Fe_xNi_{1-x}). This thin film has its easy axis in-plane, where anti-parallel magnetisations directions are crystallographically equivalent. This allows the formation of closure domains as it can be seen in Figure 2.3.

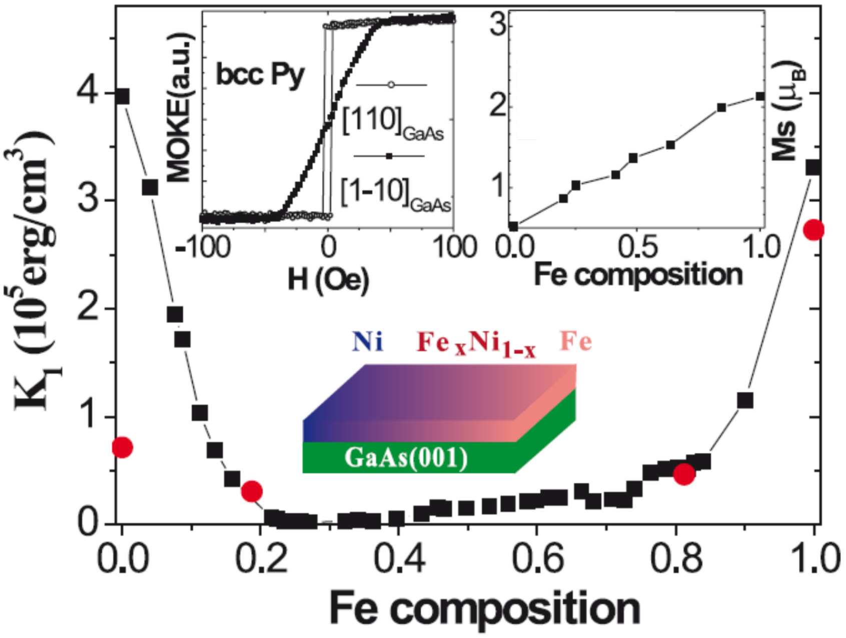

FIGURE 2.4: Cubic magnetic anisotropy constant as a function of iron concentration on a 3 nm thich bcc Fe_xNi_{1-x} composition wedge (see inset), at 300 K. Red circles are the calculated K_1 values. A representative hysteresis loop for bbc $Fe_{0.25}Ni_{0.75}$ is shown in the inset. Averaged magnetic moment per atom in bcc Fe_xNi_{1-x} is also measured by vibrant sample magnetometer as a function of iron concentration. Modified from [20].

Other forms of anisotropy besides the magnetocrystalline are the *magnetostriction, shape anisotropy, surface anisotropy* and *induced anisotropy*. *Magnetostriction* is the physical shrinking or expansion of a ferromagnet in the direction of the magnetisation when this is magnetised by an external field. *Shape anisotropy*, which arises from the shape of the sample creates a demagnetising field that is not equal in all directions, and creates more easy axis than that predicted by the magnetocrystalline anisotropy by itself. *Surface anisotropy* takes into account the different effects at the surface of the magnetic film. For instance, at a surface the spin has a nearest neighbour on one side and none on the other side (or a non-magnetic material), so that the exchange and anisotropy energy there cannot be the same as in the bulk[21–23]. Finally *induced anisotropy* can be obtained by tilting the sample at the moment of its deposition or applying magnetic or electric fields[24] in order to create a uniaxial anisotropy in the plane of the film. The problems of a deformable body, or shape, or induced anisotropy are not part of this thesis and their effects will be often ignored.

While the magnitude of the magnetisation is determined almost only by the exchange energy, the direction of the magnetisation is only determined by the anisotropy energy, pointing always in the direction for which the anisotropy energy is a minimum.

Finally, the increase in the value of the magnetisation in a sample is the result of two independent processes suggested by R. Becker [25]: 1) the increase in size of the domains, with magnetisation favourably aligned with respect to the external applied field at the expense of the unfavourably oriented domains, or 2) the rotation of the magnetisation direction towards the applied field, as can be seen in Figure 2.5. The preferred process depends upon the intensity of the applied field. The dynamics of these closure domains formed in squares of 2×2 μm of Permalloy was investigated by N. Bukin and I in reference [26]. While a large part of that work was done by me during the first year of my PhD, I did not included it as a result chapter for not being related to the rest of the results chapters.

2.4 Giant Magnetoresistance

The property of a ferromagnet to maintain a magnetic state in absence of an external magnetic field has made these materials an important subject of study in physics since the end of the 19^{th} century. Moreover, ferromagnetic materials are the cornerstone of the current data storage systems like magnetic tapes, magnetic disk drives and magnetic random access memory.

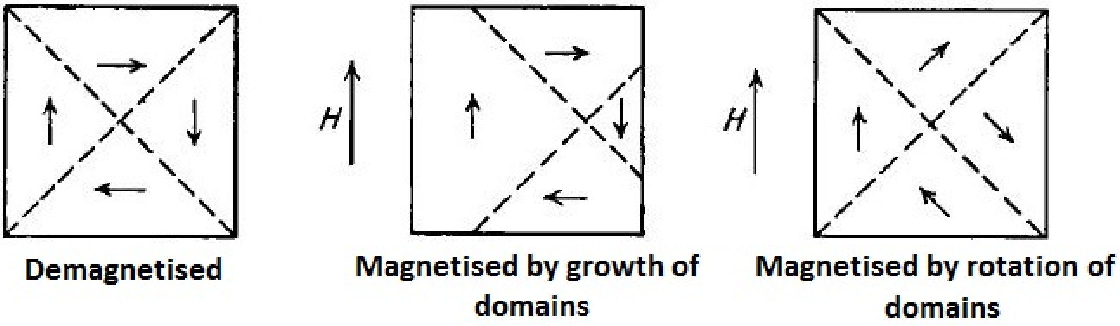

FIGURE 2.5: Fundamental process of the magnetisation (from [4])

The crucial step for the application of the ferromagnetics materials in technological devices was done by two different groups (Fert [27] and Grünberg [28]) in 1988. This was the discovery of the Giant Magneto Resistance (GMR). The GMR is an enhancement of the magneto resistance effect, which is the property of certain materials to change their resistance in the presence of an external magnetic field.

Let us take the simplest model of a conducting ferromagnet, which is the *sd* model proposed by Mott [29] in 1936. In ferromagnets , the number of valence electrons with spins up and down can be unbalanced, leading to a polarisation P along a particular axis $\hat{p}$:

$$P = \frac{(n_{\uparrow} - n_{\downarrow})}{(n_{\uparrow} + n_{\downarrow})} \tag{2.35}$$

Mott considered transition metals consisting of mobile s electrons that carry most of the current and partially filled d shells, which contains most of the polarisation. For metals such as Fe, Co, and Ni, which are relevant materials in the fabrication of most multilayer devices including the one in this thesis, the values of magnetic moment per atom at 0K are 2.22, 1.72, and $0.61\mu_B$ respectively. This corresponds to more electron spins parallel to the magnetisation axis (*majority* electrons) than anti-parallel (*minority* electrons). Calculating the spin-dependent band density of states shown in Figure 2.7 (b), we can see that there are more minority spins than majority spins at the Fermi

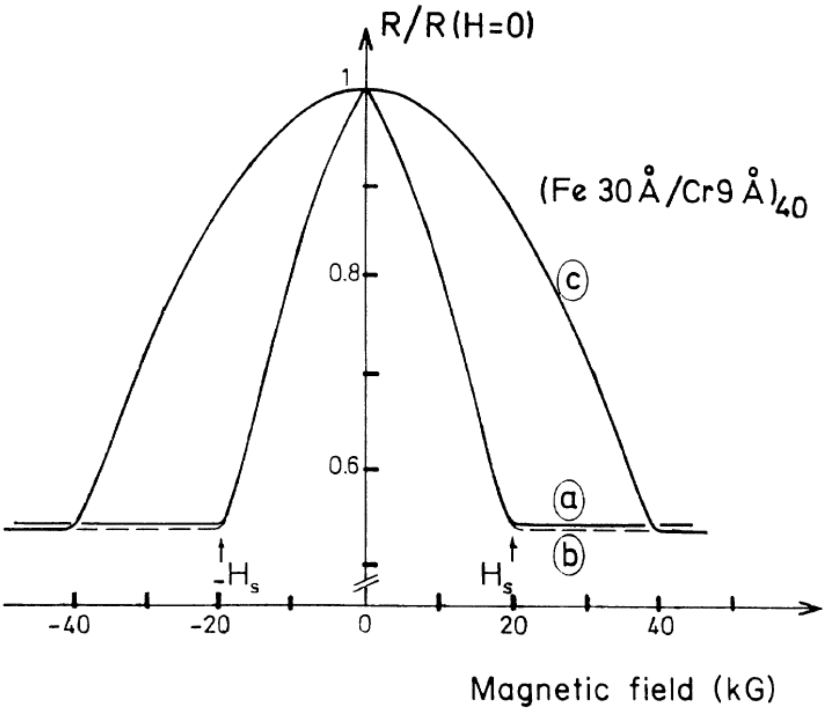

FIGURE 2.6: Magneto Resistance at different directions of the external magnetic field applied. The magnetic field is the layer plane along the current direction (a), in the layer plane perpendicular to the current (b), or perpendicular to the layer plane (c).

surface because the minority *d* bands are at the Fermi surface. The conductivity of a ferromagnet at the Fermi surface is dominated by the majority *s*-like electrons. The fact that most of the electron scattering events preserve spin direction means that majority electrons scatter into other majority states and vice versa. As we can see from Figures 2.7 (a) and (b) there is a larger density of minority states at the Fermi surface, which results in a greater number of scattering events (*sd* scattering) of minority states. This causes the conductance in the minority state s-band to be considerably smaller than for electrons in the majority state. Let us take a couple of ferromagnetic layers with opposite magnetisation in contact. In this case, under a rigid band model both states, minority and majority electrons, are similar but shifted by additional energy (Figure 2.7 (a)). This potential barrier between regions causes strong scattering since there is a large potential step for spins that go from being majority to minority and vice

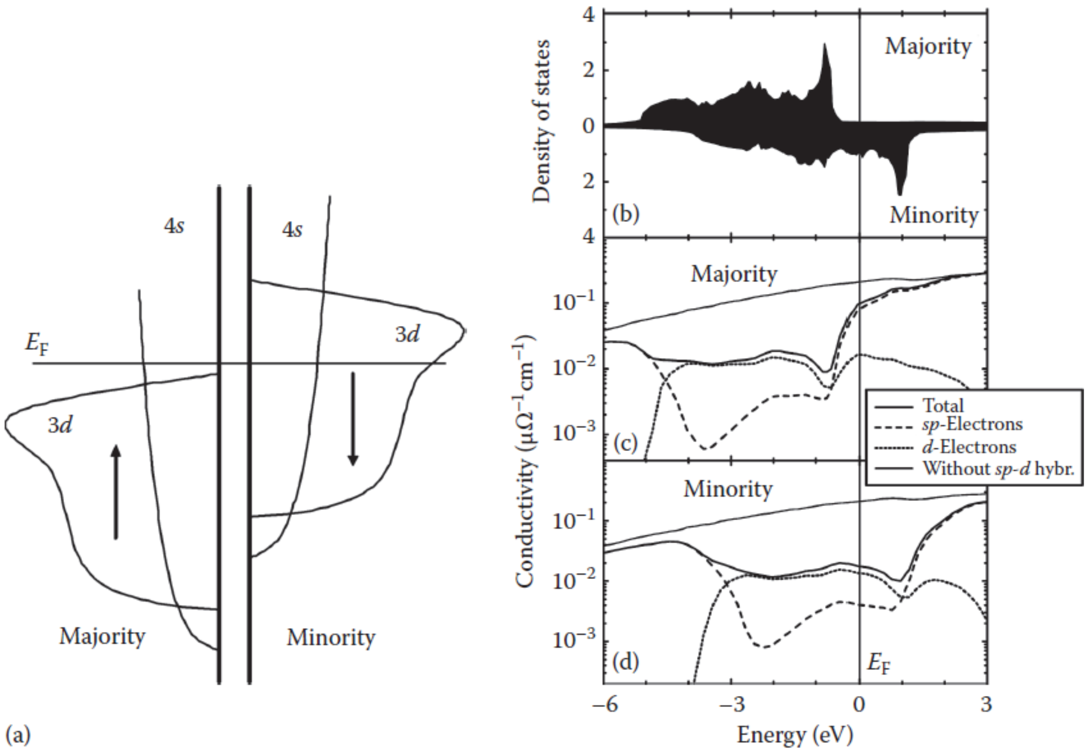

FIGURE 2.7: (a) Schematic density of states for a transition metal. (b) Calculated density of states for majority electrons in fcc Co. (c) Conductivity of majority electrons. (d) Conductivity of minority electrons. At the Fermi surface, most of the current is carried by majority sp electrons. (from [30]).

versa. This leads to a higher resistance than a system where the two ferromagnetic layer magnetisation is parallel. The device resistance is given by

$$R = \frac{(R_{ap} + R_p) - (R_{ap} - R_p)\cos\theta_m}{2}, \tag{2.36}$$

where R_{ap} and R_p are the device resistances in the antipararlell and parallel configuration respectively and θ_m is the angle between the polariser and the free layer, as it can be seen in Figure 2.8.

To understand this behaviour, consider a metallic thin film made of (001)Fe/(001)Cr superlattices with an anti-ferromagnetic coupling between them, as is shown by Fert *et al.* [27]. The multilayer resistance is measured in a presence of different values of external magnetic field. The results of these measurements show a decrease of the resistivity, compared with resistivity at zero field, with the increase of the external magnetic field, as is shown in Fig. 2.6.

When the external field is off, both layers presents anti-parallel magnetisation and the interface between them presents a scattering potential for those electrons which have a spin anti-parallel to that surface. When a magnetic field is applied gradually both layers align their magnetisation, suppressing the scattering potential due to the anti-parallel magnetisation interface, increasing the conductions of those electrons, which have a parallel spin to the magnetisation and decreasing the resistivity in the material. This work, together with that by Grünberg *et al.* [28] was so important for the actual understanding of the spin effects and for the development of a new technology based on ferromagnetic multilayer devices, that won the Nobel Prize for Physics in 2007.

The influence of the magnetisation on the current flow, which leads to the GMR, suggests that there may also be a reverse influence from the current to the magnetisation. In 1996, Slonczewski [31] and Berger [32] predicted this effect, now called spin transfer torque effect. The origin of the spin torque can be understood taking a multilayer system of a ferromagnetic (FM_1) -non ferromagnetic (NFM) -ferromagnetic (FM_2) layers as shown in Figure 2.8. We note that an NFM spacer has been added. In order to avoid the strong exchange coupling between the surfaces of the ferromagnets, we can introduce a spacer. This allow us to obtain a sharp change in the magnetisation between ferromagnetic layers. In this thesis, we used the most common choice of spacer layer: Cu, which at room temperature has a spin-flip relaxation of $\lambda_{sf} = 100 - 400$ nm [33]. The thickness of the spacer must be less than λ_{sf}. Here, C_a and C_b regions are non magnetic contacts. Also consider the magnetisation of (FM_1) in M_1 direction and (FM_2) in M_2 direction, not parallel to each other. A current of electrons goes from C_a to C_b passing through the stack. When the electrons are in the region C_a their spins are not oriented in any preferential direction and we say that they are *unpolarised* . After passing the region FM_1 the spin current is *polarised* by M_1 in the M_1 direction, remains polarized in neighbouring non-magnetic layers , and when they pass through the region FM_2 it is polarised by M_2 in the M_2 direction. Due to the conservation of the angular momentum, the change in angular momentum after passing through M_2 can be explained as an absorption of this angular momentum by the local magnetic moments in FM_2. This absorption can be viewed as an effective torque retreated with a green arrow in Figure 2.8. FM_2 is considered the free layer and usually is built relatively thin and with a low intrinsic Gilbert damping making it easily susceptible to the influence of STT. A common material chosen for this layer is the permalloy ($Ni_{81}Fe_{19}$). On the other hand, FM_2 is considered the fixed layer and is usually thicker than the free one. This layer polarises the initially unpolarised electron current.

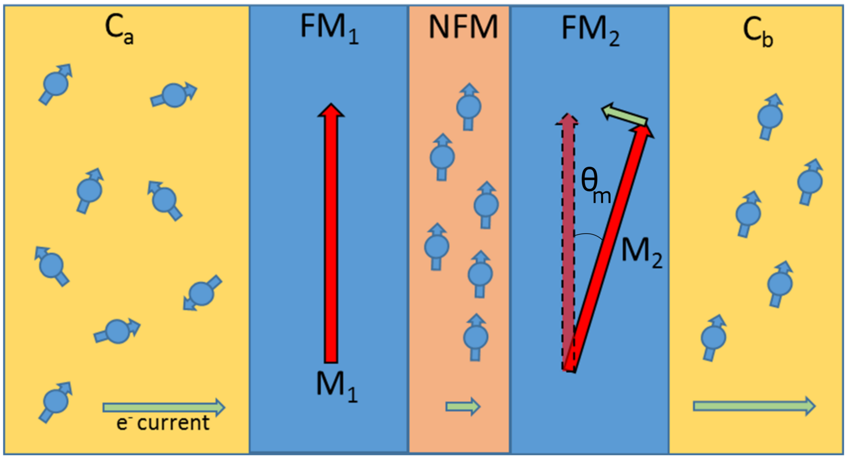

FIGURE 2.8: Spin transfer torque schematic

2.5 The origin of the Spin Transfer Torque effect

In order to understand the equations that govern this phenomena we have to analyse the equations of motion of the magnetisation

2.5.1 Landau-Lifshiftz-Gilbert-Slonczewski equation

Equation of motion of magnetisation without damping

Let us consider a localised spin $\vec{S}_i$ which obeys the torque equation

$$\frac{d\vec{S}_i}{dt} = \vec{\tau}_i\,, \tag{2.37}$$

which under a conservative system can be written in terms of an effective field H_{eff} action of the ith spin

$$\frac{d\vec{S}_i}{dt} = \mu_0\vec{\mu}_i \times \vec{H}_{\text{eff,i}}\,. \tag{2.38}$$

where $\vec{\mu}_i$ is the magnetic moment. Since $\vec{\mu} = \gamma\vec{S}$

$$\frac{d\vec{\mu}_i}{dt} = |\gamma|\,\mu_0\vec{\mu}_i \times \vec{H}_{\text{eff,i}}\,. \tag{2.39}$$

or

$$\frac{d\vec{M}(\vec{r})}{dt} = |\gamma|\mu_0\vec{M}(\vec{r}) \times \vec{H}_{\text{eff}}(\vec{r})\,. \tag{2.40}$$

Here $\vec{M}(\vec{r})$ is the magnetisation or the moment per unit volume at a point $\vec{r}$ and the effective field is defined as

$$\begin{aligned}\vec{H}_{\text{eff}} &= -\vec{\nabla}_M U = -\vec{\nabla}_M(U_{\text{ap}} + U_{\text{ms}} + U_{\text{an}} + U_{\text{ex}} + ...)\\ &= \vec{H}_{\text{ap}} + \vec{H}_{\text{ms}} + \vec{H}_{\text{an}} + +\vec{H}_{\text{ex}}...\end{aligned} \tag{2.41}$$

where U is the magnetic energy of the system. This energy contains contributions of different kinds and the most relevant for devices studied in this thesis are the Zeeman energy (U_{ap}), which is the one related to the interaction with the applied field; the magnetostatic energy (U_{ms}) due to dipolar interactions between spins; the anisotropy energy (U_{an}) due to crystalline or inter-facial energies; and the exchange energy (U_{ex})

due to spin-dependent quantum mechanical interactions. The gradients of these energies give rise to fields with the same name, which when summed up is the effective field, as shown in eq. (2.41).

It is important to notice that it is assumed that the exchange interaction is strong and that all of the moments in a device layer are aligned and move together, which is know as macrospin model. In this mode, the magnitude of the moment is constant in time. Considering just the dynamics on the free layer, we can rewrite eq. (2.40) in terms of the normalised momenum of the free layer $\vec{m}_f = \frac{\vec{M}_f(\vec{r})}{M_s}$:

$$\frac{d\vec{m}_{\mathrm{f}}(\vec{r})}{dt} = |\gamma|\mu_0\vec{m}_{\mathrm{f}}(\vec{r}) \times \vec{H}_{\mathrm{eff}} \,. \tag{2.42}$$

This equation says that the free layer moments will precess, with constant magnitude, around the effective field in a perpendicular direction to the energy gradient.

Equation of motion of magnetisation with damping

The eq. (2.45) does not consider the interaction of the local moment with its enviroment, which is quite strong to disregard. This interaction leads to dissipation and the relaxation of the moment into a low energy regime. It is for this that eq. (2.45) has to be modified in the following way:

$$\frac{d\vec{m}_{\mathrm{f}}}{dt} = -\mu_0\frac{|\gamma|}{1+\alpha^2}\vec{m}_{\mathrm{f}} \times \vec{H}_{\mathrm{eff}} - \alpha\frac{|\gamma|}{1+\alpha^2}\vec{m}_{\mathrm{f}} \times \left(\vec{m}_{\mathrm{f}} \times \vec{H}_{\mathrm{eff}}\right) \,. \tag{2.43}$$

This equation is know as Landau Lifshitz Gilbert (LLG) equation. The second term (damping term) causes the moment to relax towards the effective field. The strength of this relaxation is determined by the damping parameter α, which is always positive and typically take values between 0.005 and 0.05. We can also note the addition of the factor $\frac{1}{(1+\alpha^2}$ in both terms, which is responsible for the viscous damping which for large α makes the magnetisation to respond slowly. While the damping term describes phenomenologically the average interaction of the magnetisation with its environment, an extra term is added to the effective field in order to describe the random thermal fluctuations H_{th}, which is typically chosen to be a random Gaussian-distributed field with a root-mean square (rms) average value of

$$H_{\mathrm{th,rms}} = \frac{1}{\mu_0}\sqrt{\frac{2KT\alpha}{VM_s\gamma\Delta t}}, \tag{2.44}$$

where Δt is the period over which the thermal field is applied. These terms which describe the stochastic part of the system, give rise to the superparamagnetic response for small elements.

The damping term can be taken as a small perturbation to the precessional term, and under a first approximation, can be cancelled by a spin transfer torque from an applied current.

Equation of motion of magnetisation with damping and applied current

in 1996, John Slonczewski proposed the following modification to the LLG equation when a electron current is applied to a device

$$\begin{aligned} \frac{d\vec{m}_{\mathrm{f}}}{dt} = &- \mu_0\frac{|\gamma|}{1+\alpha^2}\vec{m}_{\mathrm{f}} \times \vec{H}_{\mathrm{eff}} - \alpha\frac{|\gamma|}{1+\alpha^2}\vec{m}_{\mathrm{f}} \times \left(\vec{m}_{\mathrm{f}} \times \vec{H}_{\mathrm{eff}}\right) \\ &\frac{g(\alpha_m)\mu_c I}{eM_s V}\vec{m}_{\mathrm{f}} \times \left(\vec{m}_{\mathrm{f}} \times \vec{m}_{\mathrm{p}}\right) . \end{aligned} \tag{2.45}$$

where the added term is called spin transfer torque, which is defined as a transport of angular momentum from one layer to another. This term includes the current I, the charge of the electron e, the volume of the free layer V, $\vec{m}_{\mathrm{p}}$ is the polarisation direction of the fixed layer , and $g(\theta_m)$ is a dimensionless term that contains all the information stemming from the stack geometry and materials properties within the stack and depends on the relative orientations of the magnetisation.

2.5.2 Micromagnetics

The basic spin torque dynamics can be understood assuming that magnetisation is uniform and stays uniform during the dynamic process, treating the whole magnetisation distribution as a single "macrospin" (Macrospin model). Two types of macrospin dynamics were predicted by Slonczewski in his work [31] in 1996 due to the spin torque: the switching of the direction of the macrospin in the absence of an external field, and the persistent precession excited by a DC spin-polarised current. Taking the spin torque term as an extra damping, the spin transfer torque can increase or decrease the local damping depending on its sign and the local magnetic configuration. A negative damping will be balanced by the already existing positive damping and steady-state high amplitude spin wave excitations can be indefinitely sustained, which form the basis of the Spin Transfer Oscillator [31, 34–36] the main topic in the next part of this chapter. However, assume that a uniform magnetisation of the magnetic layers is not always a justified assumption. magnetisation around the edges of the device can rotate due magnetostatic energy, or current induced magnetic fields (Oersted fields) can promote the nucleation of a magnetic vortex structure. This non-uniformities can be described by the LLGS equation by discretising the system as shown in Figure 2.9 and solving a large set of couple integro/differential equations (eq. 2.46)

$$\begin{aligned} \frac{d\vec{m}_{\mathrm{f}i}}{dt} = & -\mu_0 \frac{|\gamma|}{1+\alpha_i^2}\vec{m}_{\mathrm{f}i} \times \vec{H}_{\mathrm{eff,i}} - \alpha_i \frac{|\gamma|}{1+\alpha_i^2}\vec{m}_{\mathrm{f}i} \times \left(\vec{m}_{\mathrm{f}i} \times \vec{H}_{\mathrm{eff,i}i}\right) \\ & \frac{g(\alpha_m)\mu_c I_i}{eM_{si}V}\vec{m}_{\mathrm{f}} \times \left(\vec{m}_{\mathrm{f}i} \times \vec{m}_{\mathrm{p}i}\right) \ . \end{aligned} \tag{2.46}$$

These equations are often solved by numerical calculations using micromagnetics solvers [38, 39] due to the high difficulty that implies the analytical solution for each specific system.

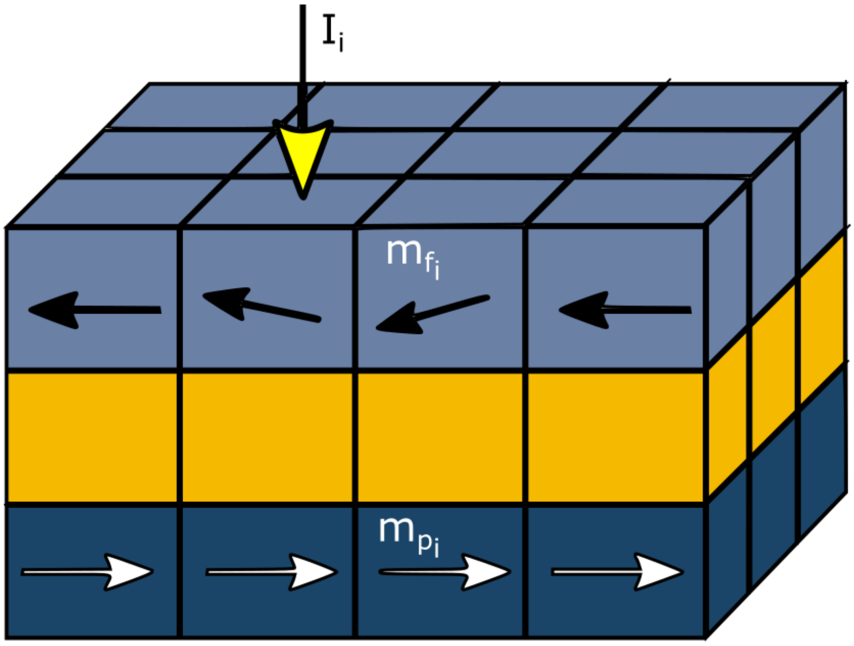

FIGURE 2.9: Discretised device structure used for micromagnetic simulations. Typical cell sizes are on the order of 3nm (from [37]).

2.6 Spin transfer oscillator based state of the art devices

In order to observe the effects of the STT in our devices, we need to pass a high current density (10^6 - 10^9 A/cm^2) [40] through the multilayer stack to transfer enough angular momentum to affect the magnetization. To do this a number of geometries have been tested in different laboratories, including mechanical contact points [40, 41], lithographically defined point contacts [42, 43], electrochemically grown nanowires [44], manganite junctions [45], lithographically defined nanopillars [46–50], tunnel junctions [51–54] and semiconductors structures. All these devices have a small cross sectional area so it allow high current density for a modest total current.

The first evidence of current-induced excitation of a ferromagnetic/non-magnetic multilayer was presented by Tsoi. *et al* [40]. To inject the necessary large current densities currents (10^6 - 10^9 A cm^{-2}), a point contact with area $\approx 10^2$nm^2 was used on top of a (Co/Cu)$_N$ multilayer sample, with the number of bilayers N ranging from 20-50 and with layer thicknesses t_{Co}=1.5 nm and t_{Cu}=2.0 - 2.2 nm. These measurements showed variations in the resistance of the device due to the high current density injected while microwave resonance studies showd peaks in the microwave absorption spectrum that correspond to the excitation of a zero-wave-number spin wave. Another important signature of the spin transfer effect was found, namely a change in the resistance of the device that is asymmetric in the current. These effects are shown in Fig. 2.10.

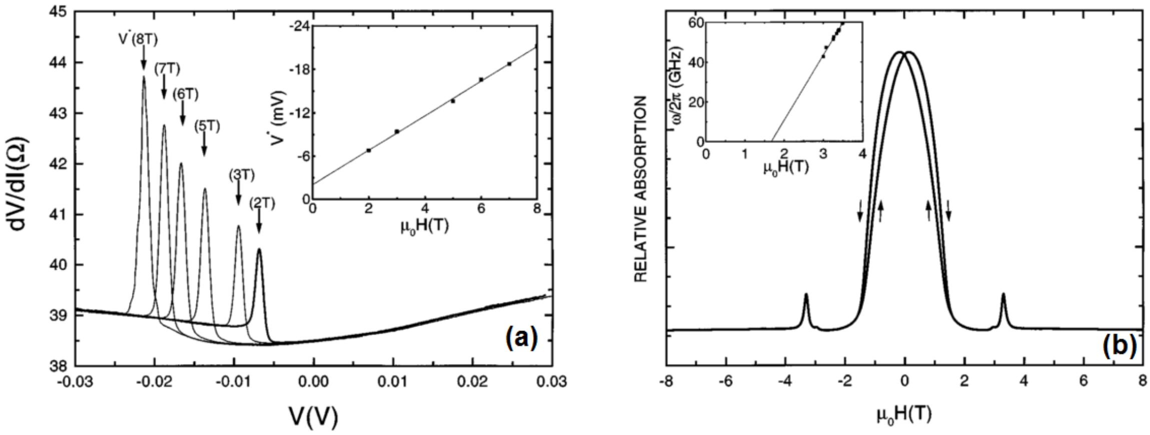

FIGURE 2.10: (a) The point contact dV/DI(V) spectra for different magnetic fields.The inset shows that the peak V*(H) increases linearly with the applied magnetic field. (b) The symmetric resonance peaks in $\pm H$ is attributed to excitations of standing spin waves in the thin ferromagnetic layer (from [40]).

A study with a more well defined geometry, better than the mechanical contact point, was performed by Katine *el al* [46]. In this work a nano pillar of 100 nm in diameter was fabricated containing two Co layers of different thickness separated by a Cu spacer. Using the GMR effect as a probe they demonstrated how an applied current can be used to controllably flip the relative magnetization alignment of the Co layers at low H, as is shown in Figure 2.11. When large magnetic fields are applied, the spin-polarized current no longer fully reverses the magnetic moment, but instead stimulates spin wave excitations.

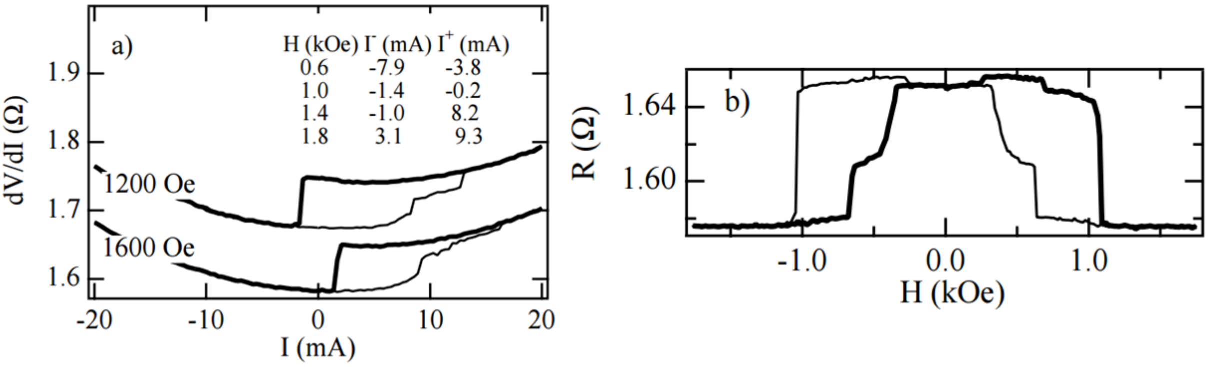

FIGURE 2.11: Differential resistance. (a) dV/dI of a pillar device exhibits hysteretic jumps as the current is swept. The current sweeps begin at zero with light and dark lines indicating increasing and decreasing current, respectively. The jump in the resistance for constant magnetic field is proof that the spin transfer torque modifies the local magnetization. (b) Zero bias magnetoresistive hysteresis loop for the same sample (from [46]).

It is our aim to work with well defined geometries so as to be able to compare our experimental results with quantitative analysis. However, instead of focusing or efforts on nano pillars devices we will instead consider lithographically defined point contacts, or *nano contacts*. Unlike in the nano pillar spin transfer oscillators, the induced magnetodynamics are not bounded by the physical dimensions of the devices allowing for potentially unfettered applications in magnonics [55–57].

2.6.1 Spin Transfer Vortex Oscillators

Since Tsoi *et al.* [40] showed the first spin transfer effects in 1998, the general characteristics of these observed dynamics were roughly understandable using the existing theories [31, 58–60], until 2007. In this year Pufall *et al.* [61] published measurements from nanocontact devices that were not easily explained by using the radially symmetric quasi uniform-mode approximations that were common at the time. A dc current was passed through a magnetic multilayer device that consisted of a nanocontact made to a psuedo-spin-valve comprising Ta (3nm) / Cu (15 nm) /$Co_{90}Fe_{10}$ (20nm)/ Cu (4 nm) / $Ni_{80}Fe_{20}$ (5nm). Similar devices were used before by the same author in 2004

[61] where the precession frequency of the coherent high-frequency magnetization induced by a spin polarized dc current could be tuned from below 5 to above 40 GHz by varying the applied current and the applied magnetic field. However, the results in the 2004 paper were markedly different to the results of 2007. The principal difference in the measurements was the reduction of the external magnetic field from $>$60 mT in 2004 to less than 5 mT in 2007. In the latter case, the oscillation was found to have a hysteretic dependence upon the dc current and lower frequency.

The magnetization dynamics were measured with a spectrum analyser and the spectral output is shown in the Fig. 2.12. We observe that the device produce no ac output until the current was increased to 11 mA, at which point the oscillations (ac voltage produced by the device) appear as a narrowband signal with a frequency of 188 MHz. On the other hand, when the current is reduced, the ac voltage persists for current values smaller than 11 mA. The large amplitude narrowband signal persists down to a frequency of 4 MHz at a current value of 8 mA, at which point the output ceases. The authors suggest that these dynamics arise from the generation and perturbation of a non-uniform magnetic state, such as a magnetic vortex, in the vicinity of the contact. This vortex is the result of the nucleation of a non-uniform mode by the combination action of the Oersted field (produced by the current in the nanocontact) and the spin transfer effect. Due to the magnitude of the external magnetic field used in previous works, this effect was not observed before. However, only the existence of the vortex is related to the external magnetic field. The frequency has hysteretic dependence upon the current and only a weak dependence on field and current, which is the crucial difference relative to previously measured spin transfer resonances.

In the same year, Pribiag *et al.* [62] reported that a d.c spin-polarized current can drive highly coherent gigahertz-frequency oscillations of the magnetic vortex in a nanoscale magnetic device. This device was a spin-valve nanopillar consisting of a thick (60 nm)

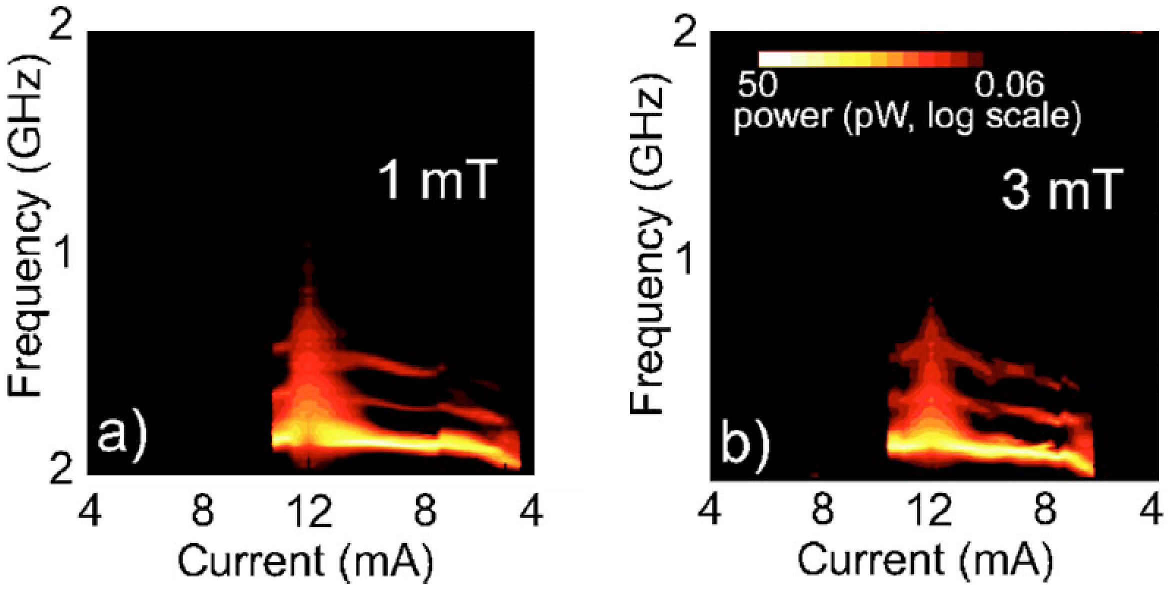

FIGURE 2.12: Output from nanocontact for in-plane field: Contour plots of spectral output fro (a) 1 mT (10 Oe) and (b) 3 mT. There is show the hysteresis of the oscillation with DC current and the dependence of the existence of the vortex with the external field (from [61]).

$Ni_{81}Fe_{19}$ ferromagnetic layer and a thin (5 nm) $Ni_{80}Fe_{20}$ layer separated by a 40-nm-thick Cu spacer. In comparison with the work of Tsoi *et al.* work [40] here a different device geometry leads to a different scale of oscillation frequency. In addition, they presented a micromagnetic simulation for comparison with experiment, which led to the oscillations being identified with gyration of the vortex core. The vortex simulation is shown in the Fig.2.13.

In 2008 Mistral *et al* [63] confirmed the predictions and suggestions about the nature of the vortex gyration made by Puffal *et al.* [61] and Pribiag *et al.* [62] by presenting simulations, analytical theory and experimental evidence of sub-gigahertz spin-transfer oscillations due to the translational motion of a magnetic vortex in a metallic nano-contact device. They proved that the sub-gigahertz modes, the increase of the

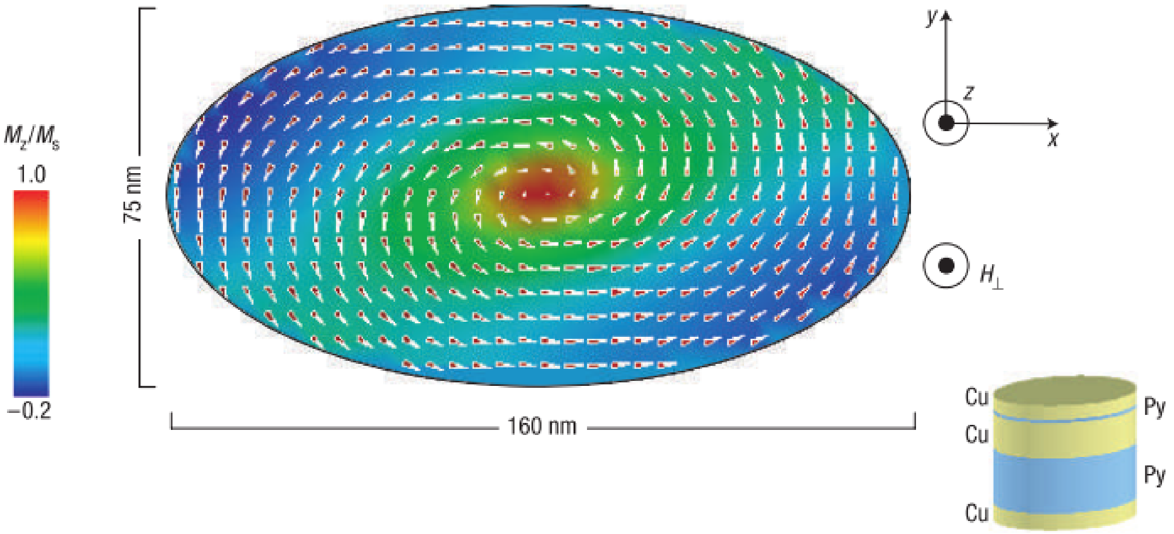

FIGURE 2.13: Micromagnetic simulation for I = 6.6 mA and $H_\perp$ = 200 Oe showing the initial magnetic configuration of the thick layer with in-plane components (arrows) and the z-component (colour shading). A schematic of the device is shown in the lower right corner (from [62]).

observed frequencies as a function of current for all applied field values, the sensitivity of the precession modes to small in-plane applied fields, and the observed field and current hysteresis of the oscillations, are all consistent with the presence of a magnetic vortex.

This new kind of device with, for example, oscillation line width narrower than 300 KHz at ∼ 1.1 GHz [62] are potential candidates for microwave signal-processing applications, wireless communication applications, and magnonic logic networks. While the low power and poor phase stability of the spin transfer oscillators are two bottleneck issues for the realisation of spin transfer oscillator based devices, the spin transfer vortex oscillator devices seems to be a solution in the low frequency regime (100 MHZ to 1 GHz). Hence, the further development of these devices is aimed at increasing the emitted power and the phase stability, and reducing the linewidth. In 2010, Dussaux *et al.* [64] presented a device that achieved an emitted power that was at least one order of magnitude larger. This device, a MgO based tunnel valve in a nano-pillar geometry, delivered much large power because of its increased magnetoresistance relative to a metallic spin valve with a Cu spacer layer.

Mutual synchronisation of multiple spin transfer vortex oscillators is another route to enhanced power emission. In 2009 Routolo *et al.* [65] (from the same group as Dussaux) presented a novel method to synchronize vortices within an array of 2 × 2 nanocontacts with intercontact distances of d=10μm , 2μm and 500 nm, as shown in Figure 2.14. The synchronization was achieved via anti-vortices within a shared free layer and led to enhanced emitted microwave power and reduced linewidth relative to a single spin transfer vortex oscillator. More examples of this technique can be found in the work of Locatelli *et al.* [66] where the auto-oscillations of two vortices within separate NiFe layers are coupled within a nano-pillar geometry, and in the work of Belanovsky *et al.* [67] who presents analytic and numerical modelling of the dynamic dipolar interaction that may also efficiently phase lock the gyrotropic auto-oscillations of multiple STVOs.

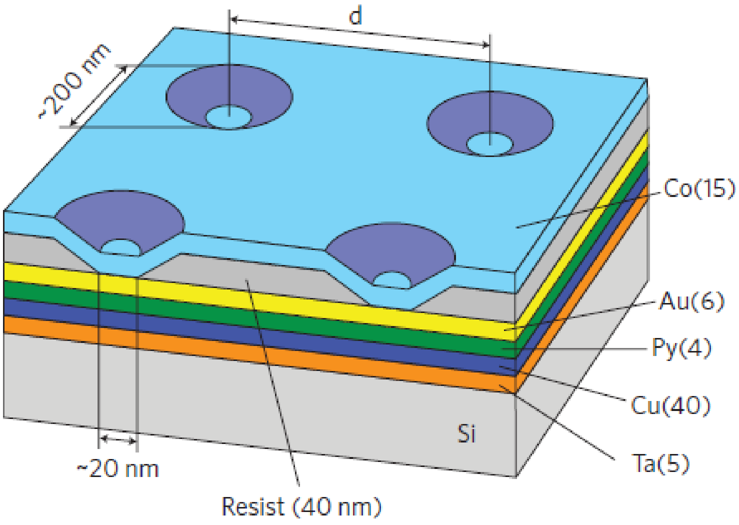

FIGURE 2.14: Schematic of the integrated array of 2 × 2 nanocontacts with intercontact distances d (from [65]).

An alternative to coupling an array of spin transfer oscillators through a common ferromagnetic layer, is to lock the gyrotropic motion of the vortex to an external microwave signal in order to increase the emission power. Rippard *et al* [68] in 2005 showed that spin transfer oscillators can be injection locked to an ac current and that the phase of oscillation can be electronically tuned by $\pm 90^{\circ}$. However, they presented results based upon locking the coherent precession of the magnetization in the free layer at gigahertz frequencies in the presence of an applied magnetic field. After the discovery of the vortex state under the nano contact at zero external field, Lehndorff *et al.* [69] demonstrated phase-locking of the dc curent-driven gyrotropic vortex motion in a vortex spin transfer oscillator to external HF signals. While the output power was too small to phase-lock another spin transfer vortex oscillator, it laid the foundation for future work. The following year, in 2011, phase locking of two isolated tunnel-valve nanopillar spin transfer vortex oscillators to an injected microwave current was demonstrated [70]. Futher work [71–73] on injection locking of spin transfer oscillators has aimed at improving the design of devices for use in technological applications.

2.6.2 Dissipative Magnetic Solitons

Vortex oscillator devices have both the fixed and free layers magnetised in-plane. However, significant changes in the fundamental dynamics of the magnetic modes are found when the free layer exhibits perpendicular magnetic anisotropy (PMA). A small field applied perpendicular to the plane excites a small angle precessional FMR-like mode with relatively small power [74]. Increasing the driving current produces an increase of the power, consistent with an increasing precession angle. However, for larger applied field, a dramatic drop in oscillator frequency and an increase in the oscillator power is observed, consistent with the formation of a magnetic droplet soliton, as it can be seen in Figure 2.15

A droplet is a localised excitation sustained by STT, with magnetisation opposite to

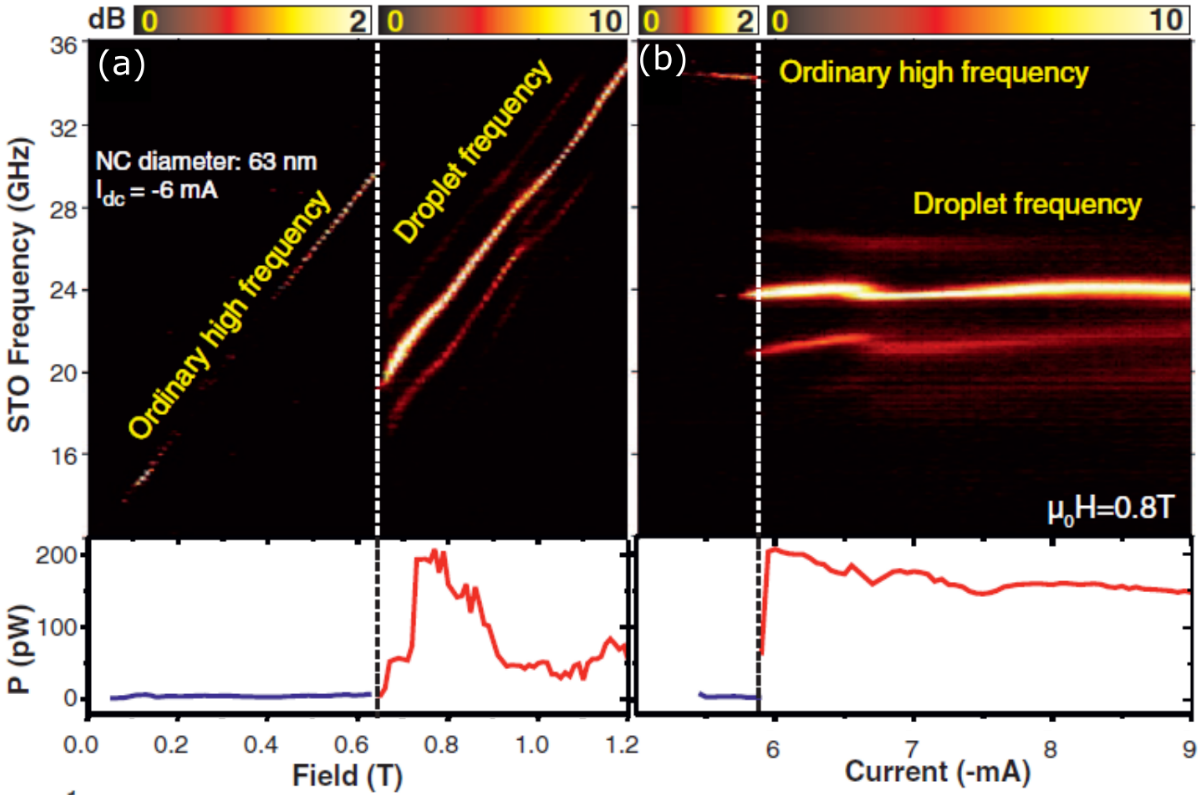

FIGURE 2.15: Frequency and power for a NC-STO with magnetic layers magnetized orthogonally as a function of (a) perpendicular field at a current of 6 mA and (b) the current when the field is set to 0.8 T (from [75]).

the rest of the free layer. All spins in a magnetic droplet soliton precess in phase around the film normal, with a precession angle $0 < \Theta(0) < \pi$ at the centre of the drop and $0 < \Theta(r) < \Theta(0)$ decresing exponentially fast, with radius to 0 in the far field [75, 76] as shown in figure 2.16. Similar to theoretically predicted conservative solitons[77], dissipative magnetic droplets can be sustained by balancing exchange with anisotropy energies and through the opposing effects of the damping and STT.

In 2013, an experimental study led by J. Åkerman [75] showed that a magnetic droplet can be created and maintained within a NC-STO. Further investigations based on transport measurements and micro-magnetic simulations of these systems [78–87] revealed a rich dynamic structure, promising a range of applications in microwave technology.

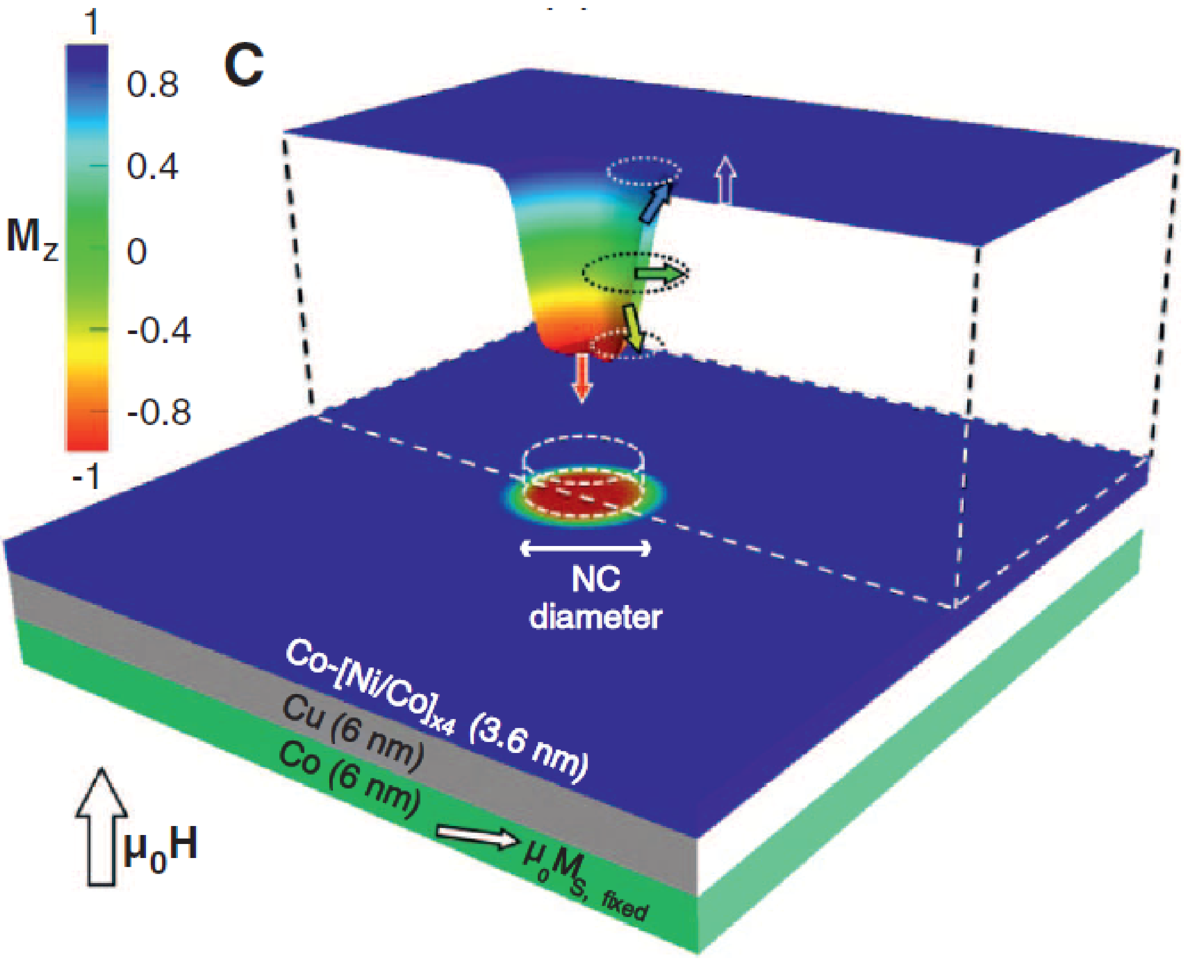

FIGURE 2.16: NC-STO on Co/Cu/Co-[Ni/Co]x4 orthogonal spin-valve with a cross section of a reversed magnetic droplet shown on top. Arrows surrounded by dotted circles indicate precession mechanism of droplet perimeter. (from [75])

2.6.3 Single Layer Spin Transfer Oscillators

While the vast majority of nano contact spin transfer oscillator studies have been performed on giant magnetoresistance trilayers (FM/NM/FM), some experiments on mechanical point contacts [41]and nanopillars [88, 89] fabricated with a single ferromagnetic layer have shown that an unpolarized current traversing a ferromagnetic layer can generate a comparable amount of spin transfer torque. In 2003, Ji *el al.* [41] reported the first evidence of spin wave excitation in a single ferromagnetic layer by high density current injection through a mechanical point contact, showing that in high fields, the behaviour of this system is close to that observed in multilayers as shown in Figure 2.17. However, the theoretical explanation used at that time [90, 91] was inconsistent with the measurements. Currently, the theory predicts that spin filtering by a single ferromagnetic layer creates a spin accumulation at both interfaces with adjoining non magnetic metals [92, 93]. When the interfaces are asymmetric, a substantial spin transfer torque can be generated. Sani *et al* [94] showed direct microwave generation from about 250 MHz to above 3 GHz (Figure 2.18 in devices with a single NiFe layer, ascribing this to creation and annihilation of vortex- anti-vortex pairs under the nano contact by the Oersted field generated by the high density current passing through the device.

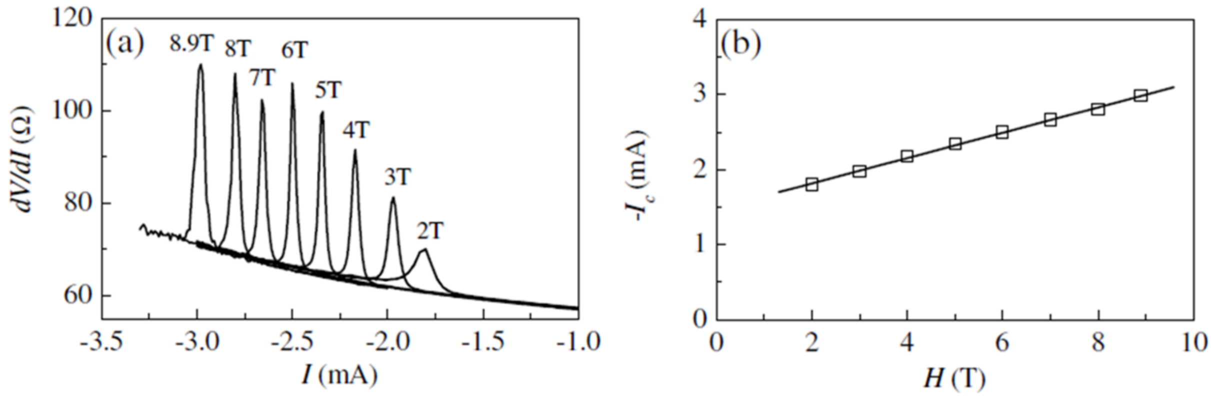

FIGURE 2.17: (a) The dV/dI - I plots at different fields for a Ag/Co point contact at 4.2 K. The critical current value at the peak position, defined as I_c depends linearly upon the external field as shown in (b)

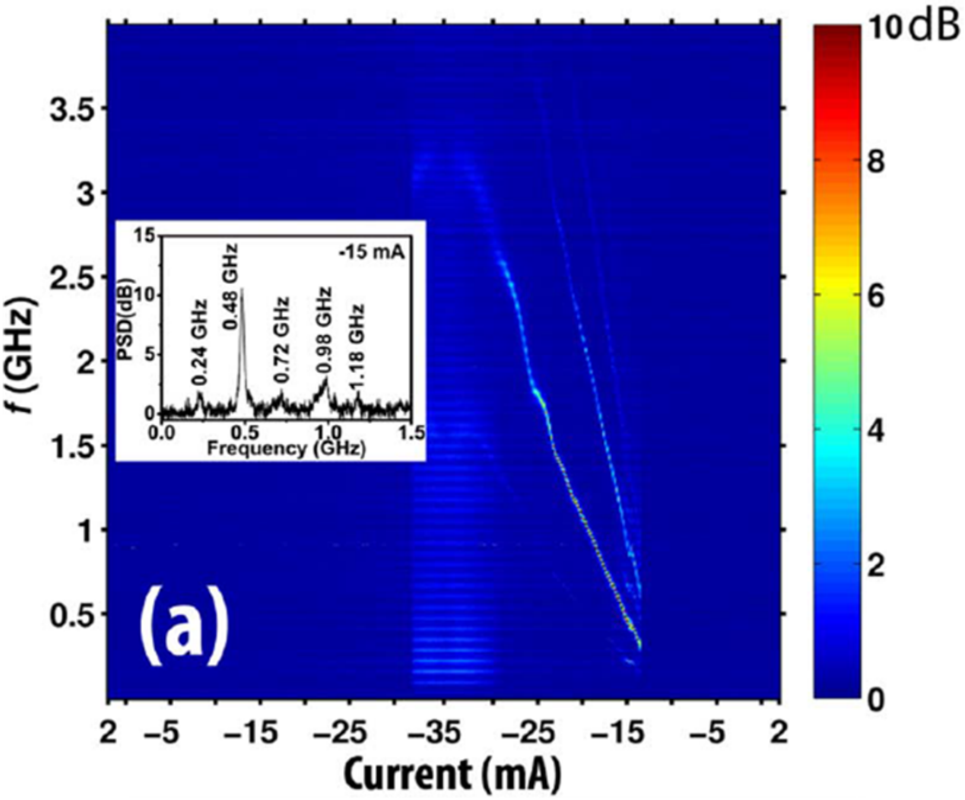

FIGURE 2.18: Current scan from 2 mA to -35 mA and back to 2 mA for a 100 nm single layer nano contact spin transfer oscillator at zero field. The inset shows the power spectral density at -15 mA where up to 5 harmonics can be observed simultaneously (from reference [94]).

2.7 Summary

In summary, the background principles of magnetism and the literature review relevant to this thesis have been introduced. The subject of the chapter covered topics from the basics of ferromagnetism to the theoretical understanding of magnetisation dynamics, giant magneto-resistance and spin transfer torque. The literature review is focused on the experimental results of the study of vortex oscillators and dissipative magnetic solitons whitin spin trasnfer oscillators, which is the focus of this thesis. In the next chapter the experimental techniques used to directly characterise magnetisation dynamics of these magnetic structures will be introduced in detail.

Chapter 3

Experimental Techniques

3.1 Holography with extended reference by autocorrelation linear differential operator (HERALDO)

Holography is an optical technique that was created to overcome the limitations produced by the spherical aberrations of electron lenses and the diffraction limit of light when it comes to achieving very high spatial resolution images on photographic systems. If fact, the very same principle of light that limits the performance of the optical photographic systems, diffraction, is the one that makes holography possible. The term "hologram" was coined by Dr. Dennis Gabor in 1948 in his paper "Microscopy by reconstructed wave-fronts"[95], where he shows the practical applications of recording on a photographic plate the interference pattern produced by the coherent beam of electrons (object wave) illuminating an object and the coherent background (reference wave) produced by an electron microscope. By doing this, the recorded interference pattern contains the amplitude and phase of the object wave and therefore the *whole* ("holos" in greek) information about the object in a single *drawing* ("gram" in greek). In order to reconstruct the original image the interference pattern or hologram is illuminated by a coherent visible light. All the aberrations of the electron optics can be corrected by optical methods during or after this process. At Gabor's time, the best coherent light source was a mercury arc lamp with a narrow-band green filter, which was used to reconstruct a 1.4 mm diameter object containing the names of Huygens, Young and Fresnel. This proof of concept encouraged the physics community to focus their research in the development and perfection of this technique. However, due to mostly the inability to separate the virtual image and the real image in the reconstruction step, and the lack of a highly coherent visible light source, scientists lost the interest in this technique.

Gabor had to wait more than 12 years to watch his invention become a practical possibility. Thanks to the invention of the laser in 1960 and the creation of the first 3D hologram using a laser by E. Leith and J. Upatnieks [96] in USA and Y. Denisyuk [97] in the Soviet Union, both in 1962, the importance of Gabor's work was appreciated and was soon implemented in science and technology. He was awarded the Nobel prize in physics in 1971 *"for his invention and development of the holographic method"*.

While Gabor's work was conducted in the optical region, in 1952 A. Baez proposed ways to use shorter wavelength radiation and construct a holographic x-ray microscope [98]. Although significant advances were done during the next 25 years [96, 99–106] , the lack of an x-ray source with sufficient coherent flux and fine-grained detectors yet to be invented made impossible the acquisitions of x-ray holograms with a better resolution than the ones obtained with visible light. This changed from 1977 with the development and implementation of synchrotron high brightness X-ray sources [107, 108] along with advances in x-ray optics technology , sensitive electronic arrays detectors and high resolution resist for X-rays. It was correctly predicted, as we can see nowadays, that the high beam coherence from synchrotron sources [104] and short-pulses of the recently developed X-ray free electron laser (FELs) [105] will shape the future of high resolution holography.

3.1.1 X-Ray holography

The holography principle applies to radiation of arbitrary energy as long as the radiation is monochromatic and with a relatively high degree of temporal and spatial coherence. This permits that the coherent background wave and the wave reflected by the studied object interfere constructively or destructively, forming the desired hologram. Due to the resolution needed to study the samples in this thesis, we will focus our study on holography X-ray radiation.

X-ray radiation

X-ray radiation comprises electromagnetic radiation with wavelengths ranging from 10 to 10^{-3} nm. The photon energy associated with that wavelength range is 10^2 to 10^9 eV and it is usually divided between soft x-rays ($\leq 10^3$ eV) and hard x-rays ($\geq 10^3$ eV), as it can be seen in Figure 3.1 [109]. However, at low energies there are not clear boundaries between what we call extreme ultraviolet (EUV) and soft x-rays and at high energies between hard x-rays and gamma rays. While the former region is usually associated with scientific analysis of materials through diffraction techniques, and medical and dental imaging, the soft x-ray region is specially interesting for us as a tool for elemental and chemical identification due the high degree of energy absorption in all materials within this energy range.

X-ray sources

- First generation sources The first generation of x-ray sources date since 1895, when x-rays were discovered and studied by Wilhelm Conrad Röntgen until the 1950s, where synchrotron and storage rings came into operation. During these 50 first years, x-rays were produced by sealed tubes in which a tungsten filament under a high voltage ($\sim$ 40 kV) emitted electrons onto a metal target, which absorbed and re-emitted radiation within the x-ray energy. In order to compare

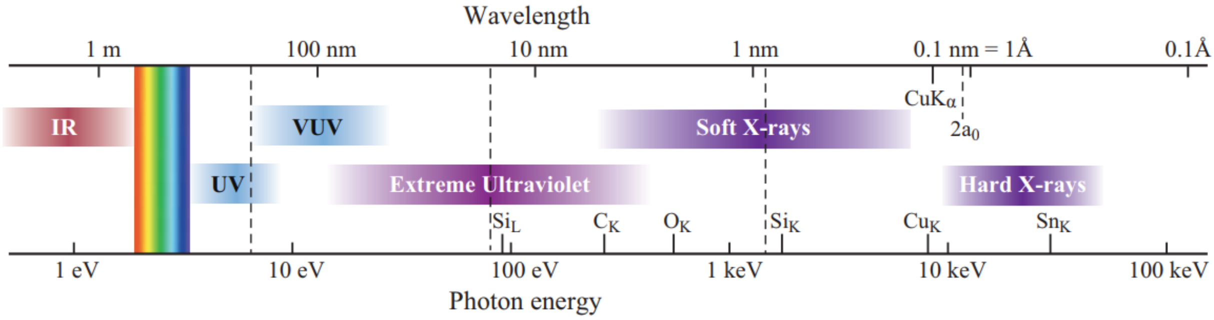

FIGURE 3.1: The electromagnetic spectrum from the infrared (IR) to the x-ray regions.The rainbow coloured part corresponds to the visible light, ranging from 450 to 650 nm wavelegth. At shorter wavelegth are ultraviolet (UV) and extreme ultraviolet (EUV) radiation, soft x-rays (SXR) and hard x-rays. Different K or L-absorption edges are shown for common elements for references, as the cooper K_α emission line at 1.54 Å(8.05 KeV), and twice the Bohr radius at $2a_0$=1.06 Å. Vertical dashed lines correspond to the transmission limits of commom window materials used to isolate vaccum: fuse silica (pire SiO_2) at 200 nm, a ∼ 100 nm thick layer of Si_3N_4 at 15 nm, and a 8 μm thick beryllium foil at a wavelength of about 1 nm.

the quality of x-rays sources we need to define brilliance. This is defined as the number of photons per area of the source, per solid angle, per second and per the photons failing wihting a bandwith (BW) of 0.1% of the central wavelength or frequency . First generation sources had a maximum brilliance of 10^{13} (photons/s·mm^2·mrad^2·0.1% BW)

- Second generation sources In the 1950s, the first particle accelerators and electron storage rings were built for the elementary study of particle physics. The relativistic velocities achieved from these particles produced spontaneous x-ray radiation that was used as a byproduct of these machines. Due to the relativistic transformation from the source reference frame to the laboratory frame, the emission produced was squeezed into a narrow cone, which increased the brilliance of these sources by two orders of magnitude compared with the first generation sources.

- Third generation sources

The optimisation of storage rings for electrons optimised and built from scratch as x-ray sources gave rise to the third generation of these sources. The first of these storage ring, commonly name "synchrotron light source" or "synchrotron", was commissioned in 1968 and since the development of new pieces of equipment as wigglers and undulators has increased the brilliance of the light source to about 10^{19} (photons/s·mm^2·mrad^2·0.1% BW). First generation sources had a maximum brilliance of 10^9 (photons/s·mm^2·mrad^2·0.1% BW). It is expected that a Extremely Brilliant Source (EBS), which will be in operation at the European Synchrotron Radiation Facility (ESRF) in France will produce x-ray with a brilliance of 10^{21} (photons/s·mm^2·mrad^2·0.1% BW) by 2022. Figure 3.2 shows a graph of the evolution of brilliances associated with each generation source during the last century.

In-line holography

When holography was proposed by Gabor in 1948, a single plane coherent light beam interacted with the sample producing the object wave and served as the reference wave, as it can be seen in Figure 3.3 (a).

The resulting interference pattern is a set of concentric rings (Figure 3.3 (b)) where the radius r_n of the nth ring is given by

$$r_n = \sqrt{(2nd\lambda)} \tag{3.1}$$

where d is the distance of between the object and the detector and λ the wavelength. The spatial resolution δ of this technique is limited by a quantity called numerical aperture (NA) which is defined by *the maximal angle at which the interference fringes are recorded with good visibility* [110–112] by the relation $\delta \geq \frac{\lambda}{2}$. Given s the source size, σ as the detector resolution, and M as the magnification defined by the ratio of the source-detector and source-object distances, we can define some cases to calculate the

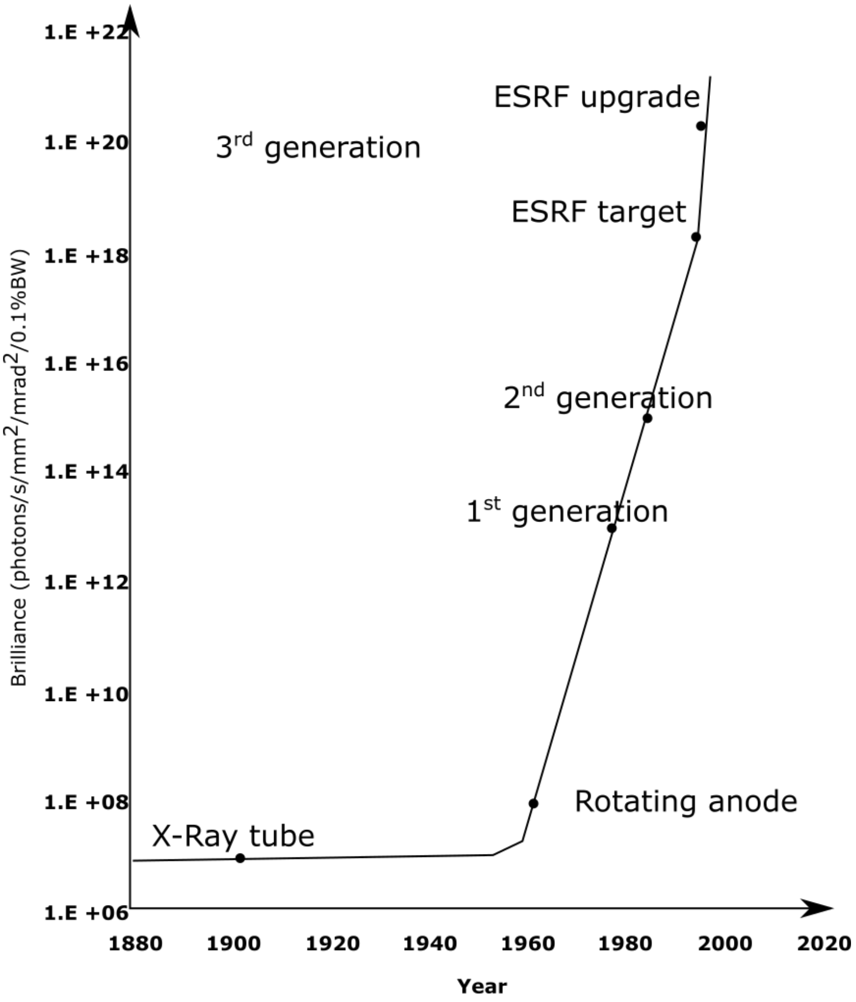

FIGURE 3.2: Evolution of the brilliance of x-ray sources since x-rays' discovery.

resolution of the technique:using a plane reference wave ($M = 1$) gives us a resolution of $\delta = 0.61\sigma$ while using a spherical reference wave gives us $\delta \approx 1.22s$. In the soft x-ray range, a spherical wave can be produced by focusing the beam by means of spherical multilayer mirrors [113], Fresnel zone plates [114–118]and pinholes [119–121] as shown in Figure 3.3 (c). In general, using a spherical reference wave offers advantages over the plane reference wave. For instance, the resolution is only determined by the ratio $\frac{\sigma}{M}$ and not by the pixel size of the charge-coupled device (CCD) detector. In addition, focusing the primary beam close to the studied sample increment the object wave intensity, which increment the hologram contrast [112].

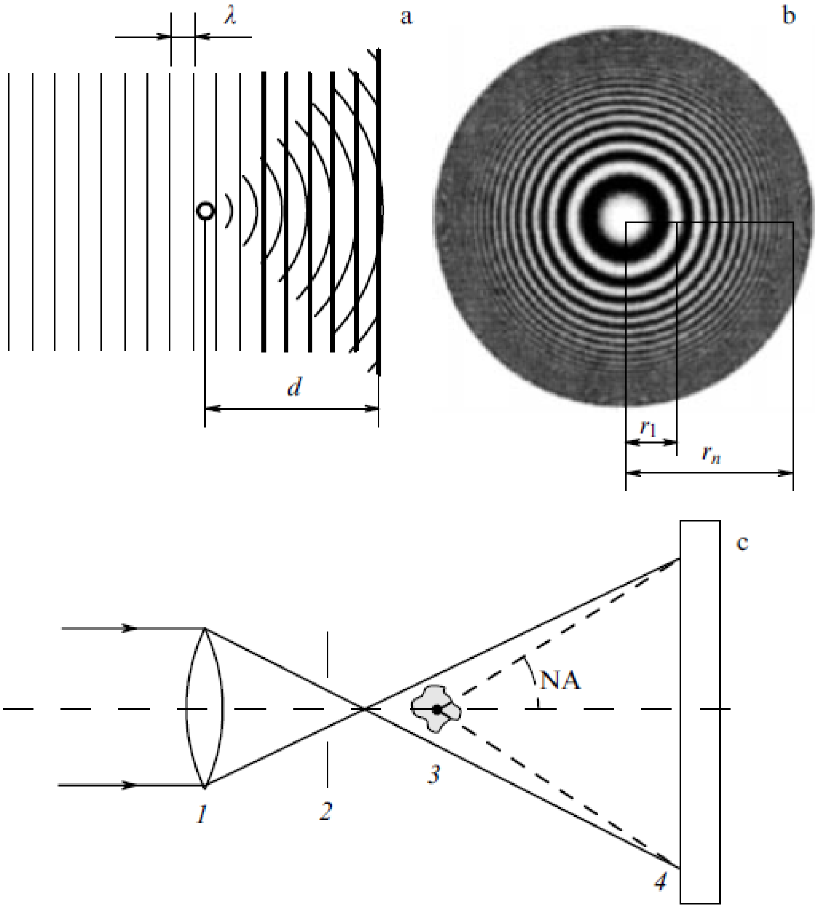

FIGURE 3.3: (a) In-line holography schematic, where d is the distance between the sample and the detector. (b) Interference fringes produced by the object wave and the reference wave when the object of study is illuminated. (c) Schematic of on-axis holography using a spherical wave to illuminate the object: 1-focusing optics, 2- order sorting aperture, 3-the object, 4- detector, NA- numerical aperture (from [110]).

Although the simplicity of the technique allows it to be used in several applications [115, 117, 120–123], there is a main drawback that limits the quality of the reconstructed image: the so called double image effect. In simple words, when the reconstruction process takes place there are always three constituent parts: the zero diffraction order and two conjugate images, virtual and real. These three parts are superimposed distorting the final image. This second hologram is the product of a virtual image produced by one of the diffraction orders and interferes with the non-diffracted beam, producing a new hologram. The distortion of the image can be small if the Fraunhofer condition

$$a^2 \ll d\lambda \tag{3.2}$$

is fulfilled, where a is the size of the sample. In addition, there are iterative procedures where this artefact can be removed. However, due to the nature of the in-line set-up, the separation would never be complete.

Off- axis holography

Leith and Upatniek [96] proposed a modification of the in-line Gabor's set-up in order to avoid the double image effect. In the off-axis configuration, the reference wave and the object wave travels in different paths with an angle $\Delta\theta$ as shown in Figure 3.4. In this way, the final components of the reconstruction are in different places and can be observed separately. The only constraint is that the size of the sample must be smaller than the transverse coherence length of the beam. At the same time, it must satisfy the condition $a < d\Delta\theta$. While the technique solves the main problem of Gabor's set-up, it introduces an extra optical element (mirror, prism or waveguide) and requires a wide coherent beam. This introduces other problems such as limitations in the radiation energy, and spatial resolution which are now determined by the waveguide cross section (among other paramenters) used to separate the x-ray source in two paths. [124].

Fourier-Transform holography

Fourier-Transform holography works under the same principle of off-axis holography, but the reference and the object wave are generated in the same plane, perpendicular to the x-ray's ray vector and thus parallel to the detector. Usually the reference wave is produced from a small hole (point-like source) made on a x-ray opaque metallic foil

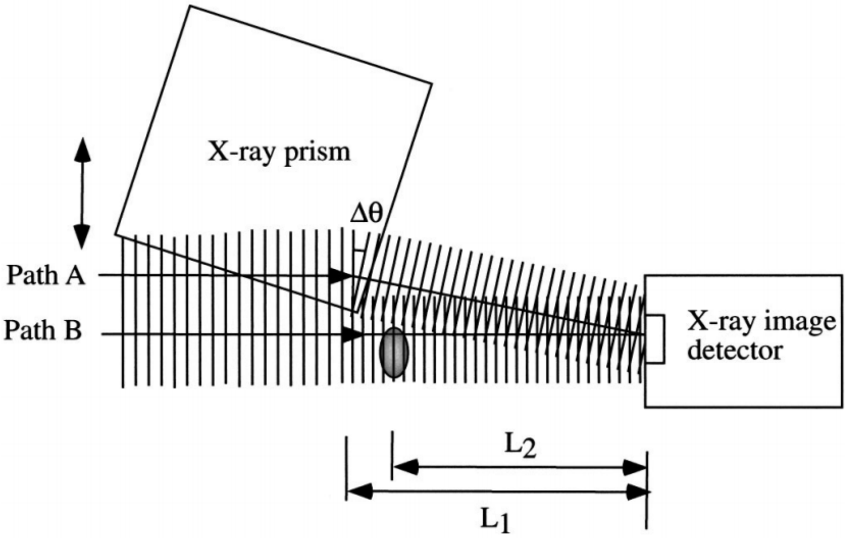

FIGURE 3.4: Experimental set-up of off-axis holography using a prism as a splitter. $\Delta\theta$ is the deflection angle of the x-rays through the prism. In order to use this sep-up, the maximum suitable size for the object is $L_2\Delta\theta$ or the size of the coherence area. L_1 (L_2) is the distance between the x-ray prism (object) to the detector (from [125])

an at a distance x from the studied area [126]. If both the sample and the reference are illuminated with a common source and its transverse coherence exceeds the spacing between them, a phase-coherence is achieved and the resulting hologram can be ascribed to the Fourier transform (FT) of the interference between the object plane and the object wave in the hologram [127]. A complex-valued image may be reconstructed using inverse FT in a single-step deterministic computation, which greatly reduces the reconstruction time of a digitalised hologram. When the condition $d \gg x$ is satisfied, the interference pattern consists of uniformly spaced fringes $\frac{d\lambda}{x}$ as it can be seen in Figure 3.5. Due to the large spacing between the interference fringes on the hologram, the requirements of the spatial detector resolution are not as high as for other holographic and phase retrieval techniques, and the resolution of the technique is typically limited by the size of the reference hole. On the other hand, the quality and contrast on the reconstructed image depend of the relative amplitudes of the object and reference waves and is highest when these two are equal. A small reference hole will generate a small flux of photons and therefore a low intensity reference wave, producing a high resolution but poor contrast image. A big reference hole will generate a reference wave with comparable intensity to the object wave, producing a high contrast but low resolution image. A successful reconstructed image will depend on the balance between these two parameters and the desired output.

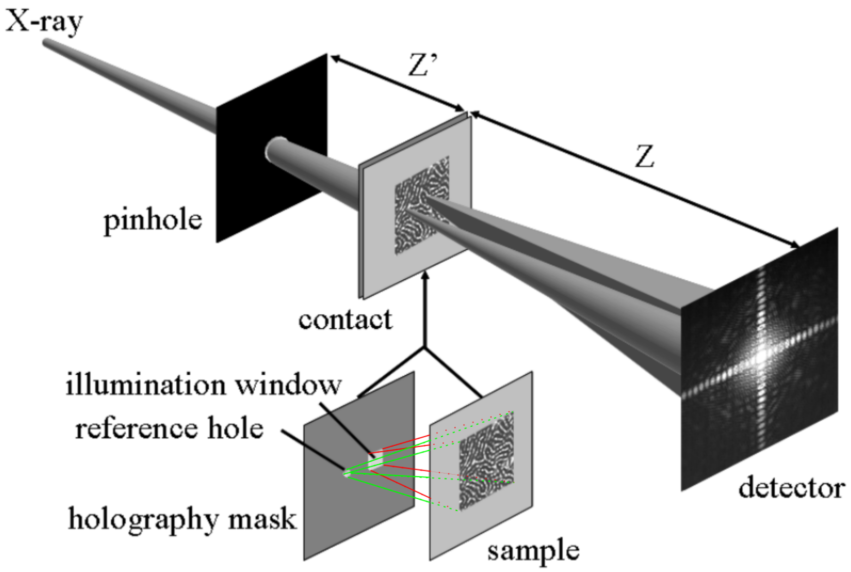

FIGURE 3.5: Schematic figure of the experimental geometry of contact x-ray Fourier transform holography. Figure reproduced from [127]

In order to increase the intensity of the reference wave without compromising the resolution of the technique, several ideas have been proposed and tested. It is possible to increase the number of references around the sample, which give rise to more reconstructed images [128]. The posteriori averaging of these images increase the contrast and signal-to-noise ratio. Careful positioning of the references is required to not produce overlapping images, which limits the number of references to 5 [129]. Another approach to increase the intensity of the reference wave-front is by using the first diffraction order of Fresnel-zone plates as a spherical reference wave while the sample is illuminated with the non-diffracted primary beam[130–133]. In this case, the spatial resolution is limited by the focal spot of the focused first order. Finally, instead of using a point-like reference source it is possible to modify the geometry of reference, which is the subject of the next subsection.

3.1.2 Holography with extended reference by autocorrelation linear differential operator

Holography with extended reference by autocorrelation linear differential operator, or HERALDO, is an off-axis holography technique where the reference has a different geometry than the point-like geometry used in Fourier-transform holography. Depending on the manufacturing process or the aim of the research, the reference can take the form of a thin wire, a sharp tip, a slit, or even a parallelogram. The condition required to form a suitable reference wave from these extended references is a sharp edge, which its quality determines the resolution of this technique. It is easy to see that the flux of photos formed by an extended reference is much greater than the one formed for a point-like reference and therefore the contrast of the image is greatly improved while the high spatial resolution is not affected [134–136], decreasing the general hologram acquisition time to the point of being capable of forming high resolution images with a single sample femtosecond x-ray pulse [134].

In this thesis, I used XMCD (section X of chapter X) combined with HERALDO to obtain the magnetic information of different magnetic samples. In the following sections of this chapter it is explained the sample preparation for HERALDO measurements, experimental set-up for the acquisition of the magnetic holograms, and magnetic image reconstruction using HERALDO .

Sample Preparation

HERALDO is a x-ray transmission holography technique and therefore the minimum requisite for our object of study is that it must be transparent to x-rays. In this thesis we have studied $Ni_{80}Fe_{20}$ squares of $2000 \times 2000 \times 80$ nm^3, and multilayer devices of diverse magnetic and non magnetic materials, all deposited on top of a Cu or Au coplanar-wave (CPW). At the right thickness, all these materials fulfill the transparency condition for x-rays.

- Opaque Mask deposition

  The specific techniques used to build each of the studied devices are presented in the corresponding results chapters. However, all the samples studied with HERALDO used as substrate a Si_3N_4 membrane with a thickness $\leq$ 300 nm which works as a transparent substrate (Figure 3.6 (a)). In order to create the extended reference and to delimit the area of study (object) by an aperture, we deposited a multilayer mask of {Au(95nm)/Cr(5nm)} x6 onto the reverse side of the Si_3N_4 membrane as it can be seen in Figure 3.6 (b). Due to its thickness and composition, this mask is opaque at energies on the soft x-rays range.

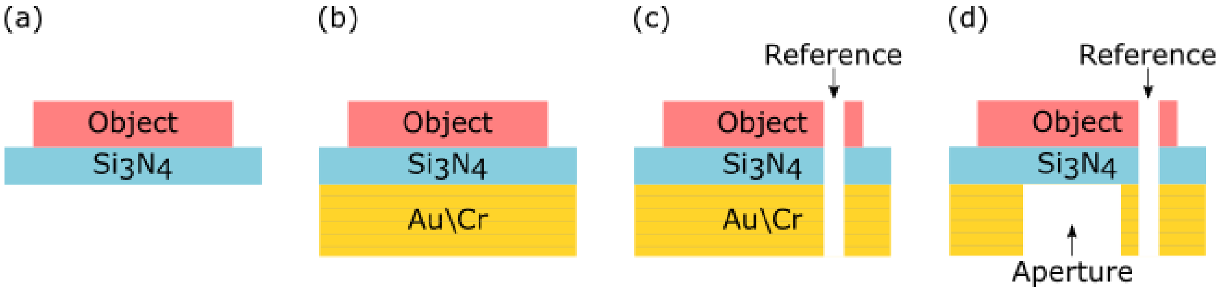

FIGURE 3.6: Step required for sample preparation for HERALDO: (a) Deposition of the studied object onto a Si_3N_4 membrane. (b) A x-ray opaque mask (Au/Cr) is deposited onto the opposite side of the Si_3N_4 membrane. (c) A reference slit is milled across the sample to produce the reference wave-front. (d) In order to produce the object wave-front, an aperture is milled to allow x-rays pass through the object and the Si_3N_4 membrane. The arrows indicate the milling direction.

- Milling the aperture and extended reference

  Using a Gallum ion beam from a xT Nova Nanolab 600 FIB located in the Imaging Suite of the University of Exeter, we milled a reference slit of 6 μm long and 30-100 nm wide which cross the sample from the object side to mask side, and circular aperture of 3-5 μm (depending on the studied sample) diameter which removes the Au/Cr until reaching the Si_3N_4 membrane as shown in Figure 3.6 (c) and (d). Using thin layers of Cr between thick layer of Au prevents the formation of thick gold grains and facilitates the milling process, improving the quality of the reference slit and promoting clean and sharp edges.

It is critical for a good resolution and a right intensity balance between the object and reference wave a good quality slit. We aimed for a slit of constant $\sim$ 30 nm width through the sample with any defects in the corners of it. The most critical parameter to achieve these features is the milling time with Ga ions. However, the reproducibility of a good quality slit is not always possible, even when using the same milling time and the same current. voltage for the ion beam and vacuum pressure in the chamber. This is mostly due to the constant use by different users that modify the eucentric high of the equipment by focusing and defocusing the Ga ion beam. Even though we correct the focus of the ion beam every time that we prepare a set of samples, we also perform a milling time test. This process consist of milling a set of references (between 15 and 20) under the same conditions of voltage and current but different milling times. Then, the sample is rotated 180 degrees and the the width of the slits that went through the sample are measured, choosing a correct milling time as the one that produce a slit width close to 30nm. Figure 3.7 (a) shows a transversal cut of a series of references made with 2 seconds of difference. In Figure 3.7 (b) we observed that the slit is not uniform through the sample. This is mostly due to the milling process, where material is not entirely removed when the Ga ions go deeper in the sample and therefore there is an accumulation of it which results in an unevenly milled slit. We take the nominal width of the slit as the one that is measured at the Au/Cr side which corresponds to the smaller one. This is the part of the slits that create the reference wave and face the detector. Figure 3.8 shows a standard scanning

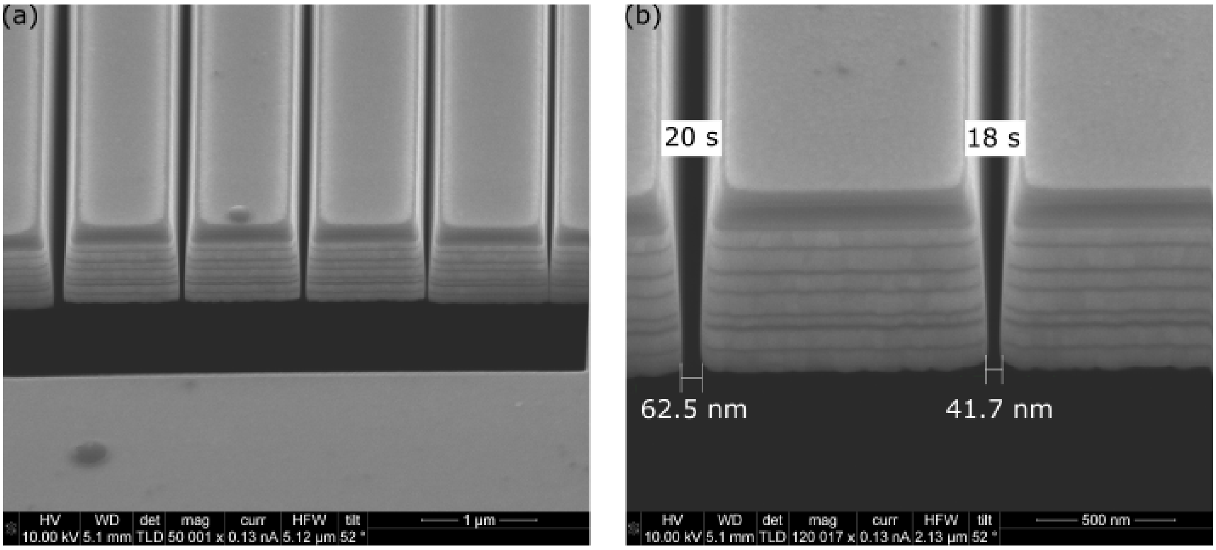

FIGURE 3.7: (a) Set of reference milled as part of a milling time test. It is important to produce a high quality end of the slit in order to obtain a coherent reference wave. (b) Close up of (a), where two slits milled under the same conditions (50 pA, 30 kV) with two seconds of difference are compared.

electron microscopy (SEM) image of a reference and aperture milled in a Au/Cu mask. As we will see in Section **??**, the reference length has to be longer than size of the object, which in this case is the diameter of the aperture. In addition, their distance has to be smaller than the coherence length of the x-rays so phase matching is achieved in the hologram. The coherence length is usually given by the pinhole used to collimate the x-ray beam and for the results presented in this thesis, is $\sim 25\mu$m.

Magnetic Hologram acquisition

Along the chapter I have demonstrated that x-ray holography is a suitable technique to investigate the spatial characteristics of the object at nanometric scale. However, by tuning the x-ray energy to characteristic absorptions edges we can go further and collect information about different elemental and chemical properties of the sample. Further to that, using different x-ray polarization it is possible to reconstructs images

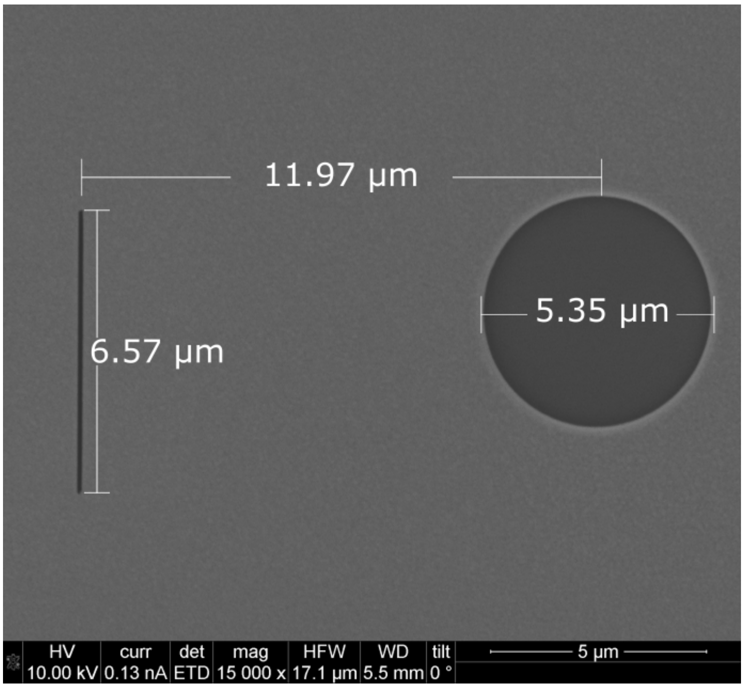

FIGURE 3.8: SEM image of a sample ready to be used in HERALDO. A reference slit and aperture where milled on the opaque mask (Au/Cr). While the reference slit goes through the entire sample, the aperture shows Si_3N_4 membrane. The object in this case is magnetic multilayer with an electric nano-contact, all located in the reverse of the Si_3N_4 membrane. The nano-contact (non-visible in the image) is contained within the aperture and is the study region of interest.

with charge[137] and spin orientations[138] information of the sample.

- X-rays magnetic dichroism

  The term *dichroism* is defined as the polarization dependence of the light absorption by a material. This dependence arise when the material's symmetry is broken. In this thesis we will use circular dichroism, which arise by breaking either the inversion or the time-reversal symmetry of the system. However, x-ray magnetic dichroism (XMCD) due time-reversal symmetry breaking by a magnetic field will be considered. XMCD originates from electric dipole (or quadruple) transitions of core electrons.

  Let us start with a $3d$ metal where the $2p$ core state is split in a $j = \frac{3}{2}$ level (L_3 edge) and $j = \frac{1}{2}$ (L_2 edge), where spin and orbit are coupled parallel and antiparallel, respectively. Irradiating the sample with circular polarized photons parallel (antiparallel) to the $2p$ moments, excite electrons of spin up (down) direction. Then, the excited electron has to find its place in the unoccupied $3d$ valence band. An unbalance of spin-up and spin-down *holes* avalable will produce a difference in the peaks of the x-ray absortion spectrum (XAS) for different circular polarization of the light. A XMCD spectrum is obtained as the differences between the two XAS spectras. If there is, for instance, more spin-up that spin-down *holes*, the XMCD spectrum will have a negative L_3 and a positive L_2 peak, as we can see in Figure 3.9.

The XAS is sensitive to a specific chemical element and by tuning the X-rays to the resonance energy of a core to valence transition, we can discriminate between different layers into a multilayer of different materials. Adding an specific circular polarization to the light, XAS can sense the magnetic polarization of the atoms, offering a method for element-specific magnetometry with a sub-micron scale. Table 3.1 show the energies of the edges relevant for magnetic transitions metals, which are relevant for this thesis.

Edge		3d	4d	5d
K	$1s \rightarrow p$	$5-11$ keV	$17-27$ keV	$65-81$ keV
$L_{2,3}$	$2p \rightarrow d$	$450-950$ eV	$2-4$ keV	$9-14$ keV
$M_{2,3}$	$3p \rightarrow d$	$30-125$eV	$150-650$ eV	$1.7-3$ keV
$N_{2,3}$	$4p \rightarrow d$	$-$	$-$	$380-610$ eV

TABLE 3.1: Relevant X-ray absorption edges (photon energies) for magnetic $3d$, $4d$ and $5d$ transition metals. The nomenclature used for X-ray spectra involving a core level n, ℓ, j, with $j = \pm\frac{1}{2}$, is as follows: K, L, M, N refer to the principal quantum number $n = 1,2,3$ respectively, while the subscripts $1,2,3$, refer to $\ell_j = s_{1/2}, p_{1/2}$, and $p_{3/2}$ respectively.Reproduced from [139].

Using resonant magnetic x-ray dichorism inherent of transition or rare-earth metals, it is possible to image magnetic domains and structures at nanometre length

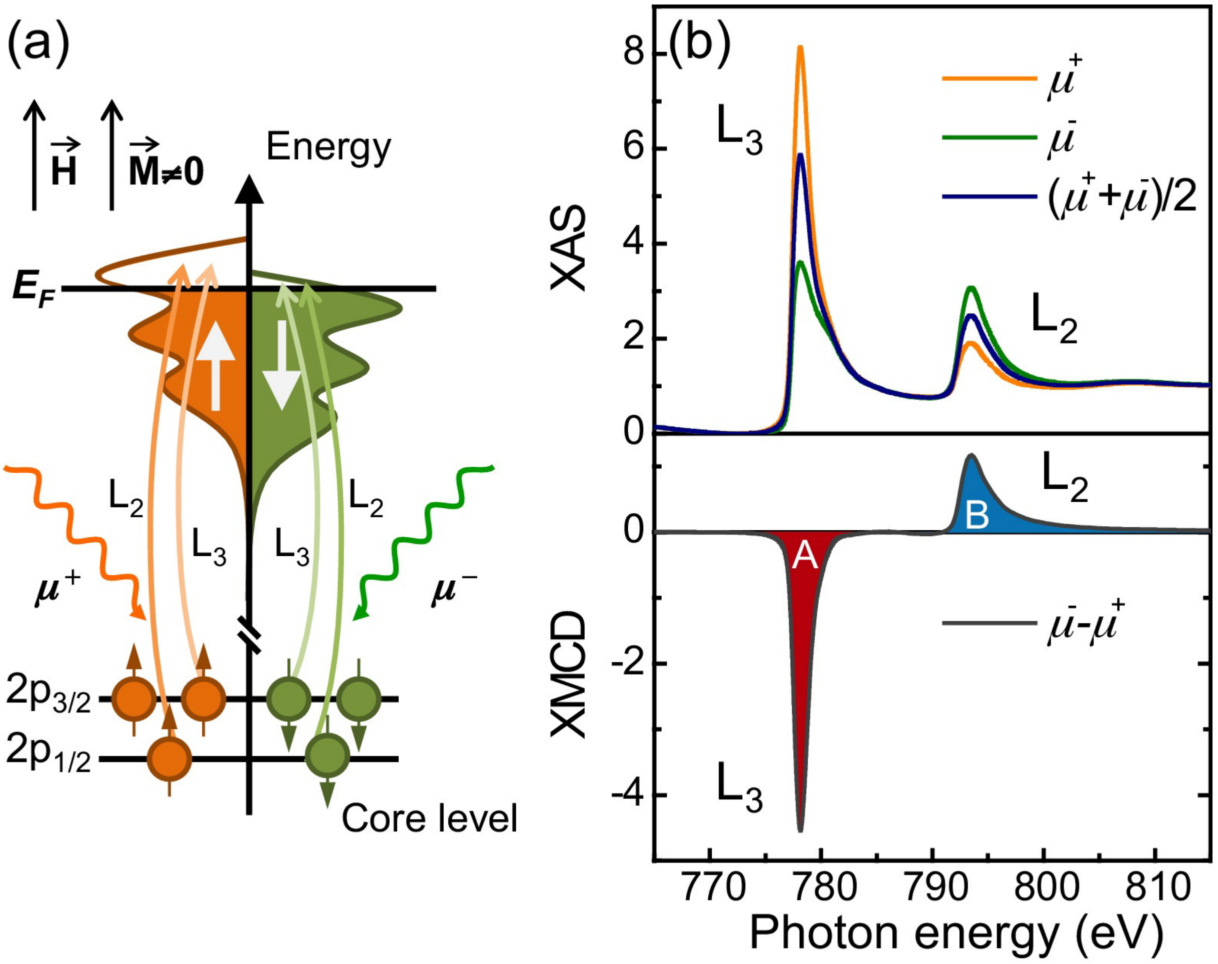

FIGURE 3.9: (a) Diagram of XMCD process for a single-electron in the resonant excitation process for a magnetic material. Firstly a spin polarized electron from the spin orbit split $2p$ level is excited by a circulary polarized photon. Photons with a positive helicity ($q = +1$) excite 62.5% spin up electrons for L_3 while just a 25% for L_2. In the other hand, photons with a negative helicity ($q = -1$) excite 37.7 % spin down electrons for L_3 and a 75% for L_2. (b) XAS at the Co $L_{2,3}$ for right (μ^+) and left (μ^-) circular polarization together with the difference spectrum: the XMCD (from [139])

scale. We can choose, for instance, a x-ray energy that coincided with the L_3 absorption edge of transition metals to produce a hologram for each circular x-ray polarization. By subtracting them we obtain a hologram that contains pure magnetic information. In this case all the charge scattering is eliminated as it is not sensitive to changes in circular polarization. The subsequent reconstruction of this "magnetic" hologram will show the magnetisation of the sample parallel the x-ray beam direction.

- Experimental set-up to perform HERALDO

  The hologram acquisition related to the results in chapters 6, 5 and 4 was done in two synchrotron source light facilities: SOLEIL (Paris, France) and Diamond Light Source (Didcot, United Kingdom). The specific details for each experiment can be found in the experiment method in each relevant chapter. However in this section I will explain the general set-up and procedure to perform HERALDO, which is common to all the holography-related chapters.

- Sample mounting

  Figure 3.10 shows a typical aluminium sample holder crafted to support sample with electrical contacts. The circular x-ray window (Figure 3.10 (a) and (b) window allows the x-ray beam to go through the sample and its truncated cone shape (Figure 3.10 (d)) permits to rotate the sample along the $\hat{y}$ axis without blocking the beam. The rotation of the sample in addition to the extended shape of the reference allow us to obtain information of the in-plain component of the magnetisation of the sample with HERALDO. The acquisition of this in-plane information is one of the most important results of this thesis.

- Hologram formation

  The sample holder is introduced within the vacuum chamber where the experiment is conducted and it position can be controlled by a $x - y$ stage in the range of the micrometers length scale. The sample is positioned in such a way that the frontal part of the sample is perpendicular facing the x-ray beam. The x-ray beam produced by a synchrotron light source is collimated by a pinhole of $\sim 20 - 25\mu$m diameter several centimetres before reaching the sample position. In order to increase the transmission of the photons through the reference and the aperture on the opaque mask, a photo-diode is positioned on the rear side

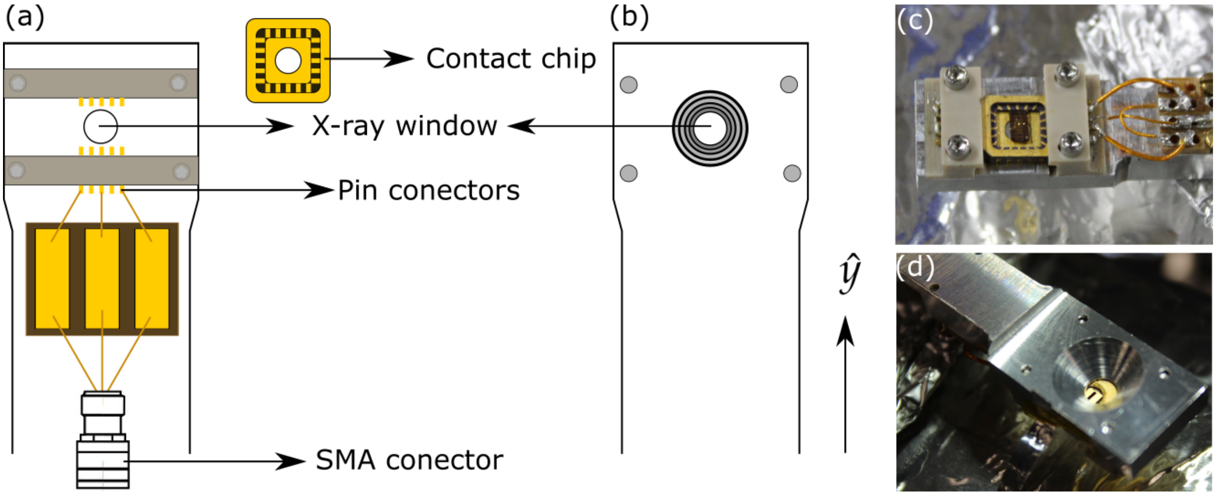

FIGURE 3.10: Schematic (a) and real image (d) of the front side of a standard sample holder used the HERALDO experiments in this thesis. The SMA connection along the pin connectors allow us to inject electric excitation to the sample hold and electrically connected to the contact chip. These excitations generate magnetic dynamics studied within a time resolved or time average regime by HERALDO. (b) Rear side of the sample holder The cone-shaped window, as is shown in (d) allow us to rotate the sample and do not block the x-ray beam by the edges of the window. Rotating the sample allow us to acquire information of in-plane magnetisation of the sample.

of the sample and its (sample) position is adjusted in such way that the signal read by the photo-diode is a maxima. It is worthy to note that several sets of references and apertures can be milled in the same irradiated sample, so special care is required at the moment of choosing the desired device. Once the position of the sample is aligned with the x-ray beam, the photo-diode is retired and a charge-coupled device (CCD) detector is positioned behind the sample. Figure 3.11 (a) and (b) depicts the position of the sample within the chamber and in the centre of the portable octupole magnet system (POMS), which allows us to apply magnetic external field in any direction of the plane xy. Figure 3.11 (c) shows the recorded hologram for one circular polarization of the source. We observe that the interference pattern is visible in the form of concentric rings which are crossed by a high intensity line. This line is formed by the reference wave passing through the slit. Due to the high intensity of the non-diffracted rays at the centre of the hologram, the transmitted light its blocked by a beam-stop. The silhouette of the beam-stop hold by two thin wires can be seen in Figure 3.11 (c).

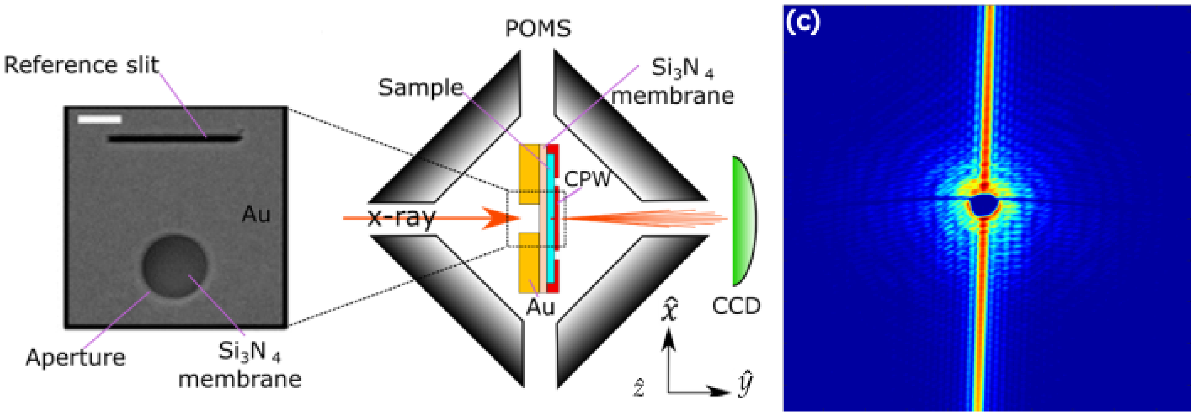

FIGURE 3.11: (a) Sample for HERALDO explained in Figure 3.8. (b) Schematic set up for HERALDO measurements with an external magnetic field. The sample is positioned in the middle of a portable octupole magnet system (POMS) and the coherent x-rays from the synchrotron source pass through the aperture and the reference slit. The resulting diffraction pattern is captured by a CCD camera at a distance ~ 60 cm behind the sample, at the end of the beam-line. (c) hologram produced by the interference of the object wave (aperture) and the reference wave (reference slit), capture by a CCD camera. The red line across the image is produce by the non-diffracted x-ray beam coming from the reference slit. Colormap: blue (red) corresponds to minimum (maximum) intensities.

Depending on the recording time of each hologram by the CCD interface software and the storage ring operation mode, the acquisition time for a hologram with a reasonable signal-to-noise ratio and for one circular polarization of the x-ray beam might take up to 45 minutes. To take advantage of the magnetic circular dichroism and obtain a magnetic signal we need to obtain one hologram for each x-ray beam circular polarization.

Reconstruction process - Theory

This subsection has been based mostly on the reference [135] .Once we have a hologram for left and right circular polarization of the source, reconstruction of the magnetic signal can take place. When subtracting both holograms we are sensitive to the magnetic information of the sample. Let us define f(u,v), the field in object space (or real space) as the sum of an object additive modulation $o(x,y)$, produced in this case by the magnetic information of the sample, and an extended reference $r(x,y)$.

Application of the linear differential operator

Working under the paraxial approximation we can describe the Fraunhofer field (far field) as "the product of a quadratic phase factor and $F(u,v) = O(u,v) + R(u,v)$, where (u,v) are the Cartesian transverse coordinates in Fourier space" [140] and the FT is defined as

$$F(u,v) = \mathscr{F}\{f(x,y)\} = \int\int f(x,y)\exp[-i2\pi(ux+vy)]dxdy \tag{3.3}$$

All integral limits are $(-\inf, \inf)$. Upper-case letters will refer to FTs of their lower-case counterpart. A intensity detector array, in this case a CCD camera, measure the Fourier intensity $\left|F(u,v)^2\right|$ in the far field and it is related to the object-space field autocorrelation by means of an inverse FT

$$\mathscr{F}^{-1}\{\left|F(u,v)^2\right|\} = f \otimes f = o \otimes o + r \otimes r + o \otimes r + r \otimes o \tag{3.4}$$

where

$$o \otimes r = \int\int o(x',y')r^*(x'-x,y'-y)dx'dy', \tag{3.5}$$

is defined as the cross-correlation of $o(x,y)$ and $r(x,y)$ and (*) denotes complex conjugation. HERALDO does not use deconvolution to separate the $r \otimes o$ or $o \otimes r$ to recover the original object field [101, 141, 142] but involves the application of linear differential operators on the field autocorrelation.

Let us select a linear differential operator, $\mathscr{L}^{(n)}$, that applied to $r(x,y)$ give us

$$\mathscr{L}^{(n)}\{r(x,y)\} = A\delta(x-x_0)\delta(y-y_0) + g(x,y)\,, \tag{3.6}$$

where A is an arbitrary complex-valued constant and

$$\mathscr{L}^{(n)}\{\cdot\} \equiv \sum_{k=0}^{n} a_k \frac{\partial^n}{\partial x^{n-k}\partial y^k}\,, \tag{3.7}$$

is a n-th order linear differential operator and a_k are constant coefficients. $g(x,y)$ can be defined as any arbitrary extended function. Applying the linear differential operator to eq. (3.4)

$$\mathscr{L}^{(n)}\{f\otimes f\} = \mathscr{L}^{(n)}\{o\otimes o\} + \mathscr{L}^{(n)}\{r\otimes r\}\mathscr{L}^{(n)}\{o\otimes r\} + \mathscr{L}^{(n)}\{r\otimes o\}\,. \tag{3.8}$$

Based on the derivative theorem for the convolution of two functions we have [143]

$$\frac{\partial}{\partial x}\left[h\otimes g(x,y)\right] = -h\otimes\frac{\partial g(x,y)}{\partial x} = \frac{\partial h}{\partial x}\otimes g(x,y) \tag{3.9}$$

which can be extended by induction to a n-th order linear differential operator $\mathscr{L}^{(n)}\{\cdot\}$ obtaining

$$\mathscr{L}^{(n)}\{h\otimes g\} = (-1)^n\left[h\otimes\mathscr{L}^{(n)}\{g\}\right] = \left[\mathscr{L}^{(n)}\{h\}\otimes g\right]\,. \tag{3.10}$$

Using eq. (3.10) on (3.8) we obtain

$$\mathscr{L}^{(n)}\{f\otimes f\} = \mathscr{L}^{(n)}\{o\otimes o\} + \mathscr{L}^{(n)}\{r\otimes r\} + (-1)^n\left[o\otimes\mathscr{L}^{(n)}\{r\}\right] + \left[\mathscr{L}^{(n)}\{r\}\otimes o\right]\,. \tag{3.11}$$

Finally, using the linear differential operator definition given in 3.6 and the sifting property of the Dirac delta [140] we obtain

$$\begin{aligned}\mathscr{L}^{(n)}\{f \otimes f\} = \mathscr{L}^{(n)}\{o \otimes o\} + \mathscr{L}^{(n)}\{r \otimes r\} + (-1)^n o \otimes g + g \otimes o \\ + (-1)^n A^* o(x + x_0, y + y_0) + A o^*(x_0 - x, y_0 - y)\,. \end{aligned} \tag{3.12}$$

The two last terms of eq. (3.12) are the most important result of HERALDO as they enable direct recovery of the original object field if the reconstruction does not overlap with other cross-correlation terms. Fourier holography is a special case in this formulation where the reference is a point-like source $r(x,y) = A\delta(x - x_0)\delta(y - y_0) = 0$, $g(x,y) = 0$ and $\mathscr{L}^{(0)}\{\cdot\} = I$ is the identity operator.

Linear differential operator for an slit

Although HERALDO works for an reference arbitrary geometry, we will determine the linear differential operator associated to a slit reference, which is the choosen reference geometry for all the results presented in this thesis.

Let's consider a reference parallel to a $\hat{x}$-axis as in shown in Figure 3.12 described as

$$r(x', y') = A\delta(y') \left[H\left(x' + \frac{L}{2}\right) - H\left(x' - \frac{L}{2}\right) \right] \tag{3.13}$$

where $H(x)$ is the Heaviside function defined elsewhere. Taking the partial derivative with respect to x', and using $\frac{\partial H(x)}{\partial x} = \delta(x)$ we have

$$\frac{\partial r(x', y')}{\partial x'} = A\delta(y') \left[\delta\left(x' + \frac{L}{2}\right) - \delta\left(x' - \frac{L}{2}\right) \right] \tag{3.14}$$

The two deltas obtained and the ends of the slit are related to the position where the image will be reconstructed. Generalizing this result to a slit making a angle α with

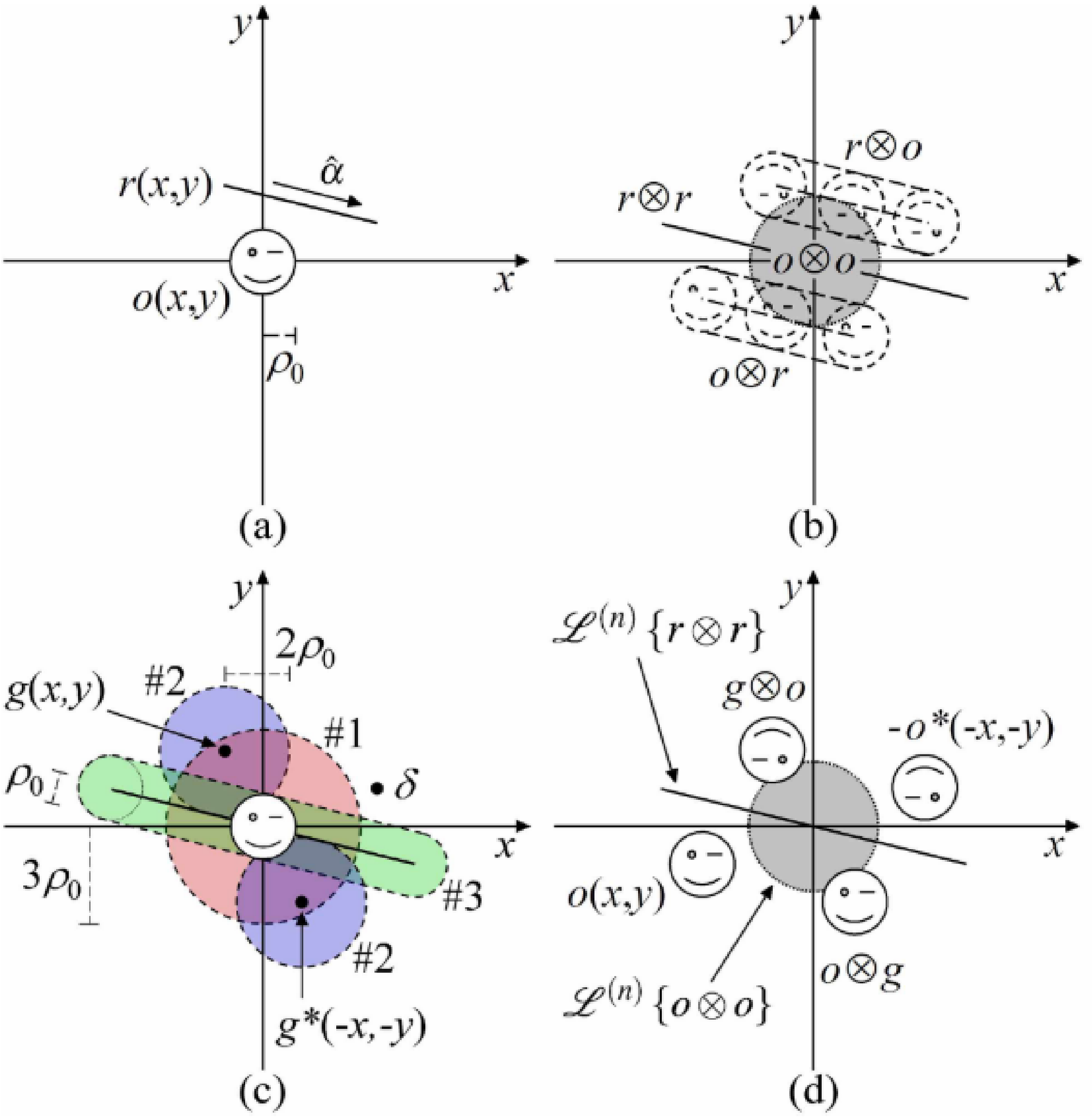

FIGURE 3.12: (a) Field $f(x,y)$ with a slit reference. (b) Field autocorrelation $f \otimes f$ (inverse FT of far-field intensity). c) HERALDO separation conditions, the reference feature must satisfy separation conditions from $o(x,y), g(x,y), g^*(-x,-y)$ and $r \otimes r$. (d) Directional derivative of the autocorrelations in the direction of the slit, $\hat{\alpha}$. Figure and caption taken from ref. [135]

respect to the x-axis, we define the non-rotated coordinates as

$$x = x' \cos\alpha - y' \sin\alpha\,, \tag{3.15}$$

$$y = y' \cos\alpha + x' \sin\alpha\,. \tag{3.16}$$

and

$$\mathscr{L}^{(1)}\{r(x,y)\} = \frac{\partial r(x',y')}{\partial x'}\,, \tag{3.17}$$

$$\mathscr{L}^{(1)}\{r(x,y)\} = \cos\alpha\,\frac{\partial r(x',y')}{\partial x} + \sin\alpha\,\frac{\partial r(x',y')}{\partial y}\,, \tag{3.18}$$

$$\mathscr{L}^{(1)}\{r(x,y)\} = (\hat{x}\cos\alpha + \hat{y}\sin\alpha)\cdot\nabla\,, \tag{3.19}$$

$$\mathscr{L}^{(1)}\{r(x,y)\} = \hat{\alpha}\cdot\nabla r(x,y)\,. \tag{3.20}$$

This results means that taking the directional derivative along the slit will produce point deltas at the ends of the slits.

If we attempt a reconstruction at one of the edges of our reference, the other end becomes g(x,y). The term $(-1)^n o \otimes g + g \otimes o$ in eq. (3.12) tell us that any feature in $g(x,y)$ will replicate the object and its complex-conjugated inversion, at any position where is non-zero as it can be seen in Figure 3.12 (b). As a condition to no overlap this cross-correlation with the intended reconstruction, we need that $g(x,y)$ and $g(-x,-y)$ be zero in a radius of $2\rho_0$, where ρ_0 is the radius of the aperture (object). (#2 in Figure 3.12 (c))

There are certain conditions to do not overlap the cross-correlation therms with the reconstruction for an arbitrary election of the reference geometry, which are described in reference [135]. In our case the reference geometry is a slit and we need to fulfil the following conditions:

- The separation of one of the ends of the slit from the centre of the object has to be greater than $3\rho_0$
- The length of the slit has to be no less than $2\rho_0$ Figure 3.13(d) show us a diagram of all the images formed after a successful reconstruction with HERALDO.

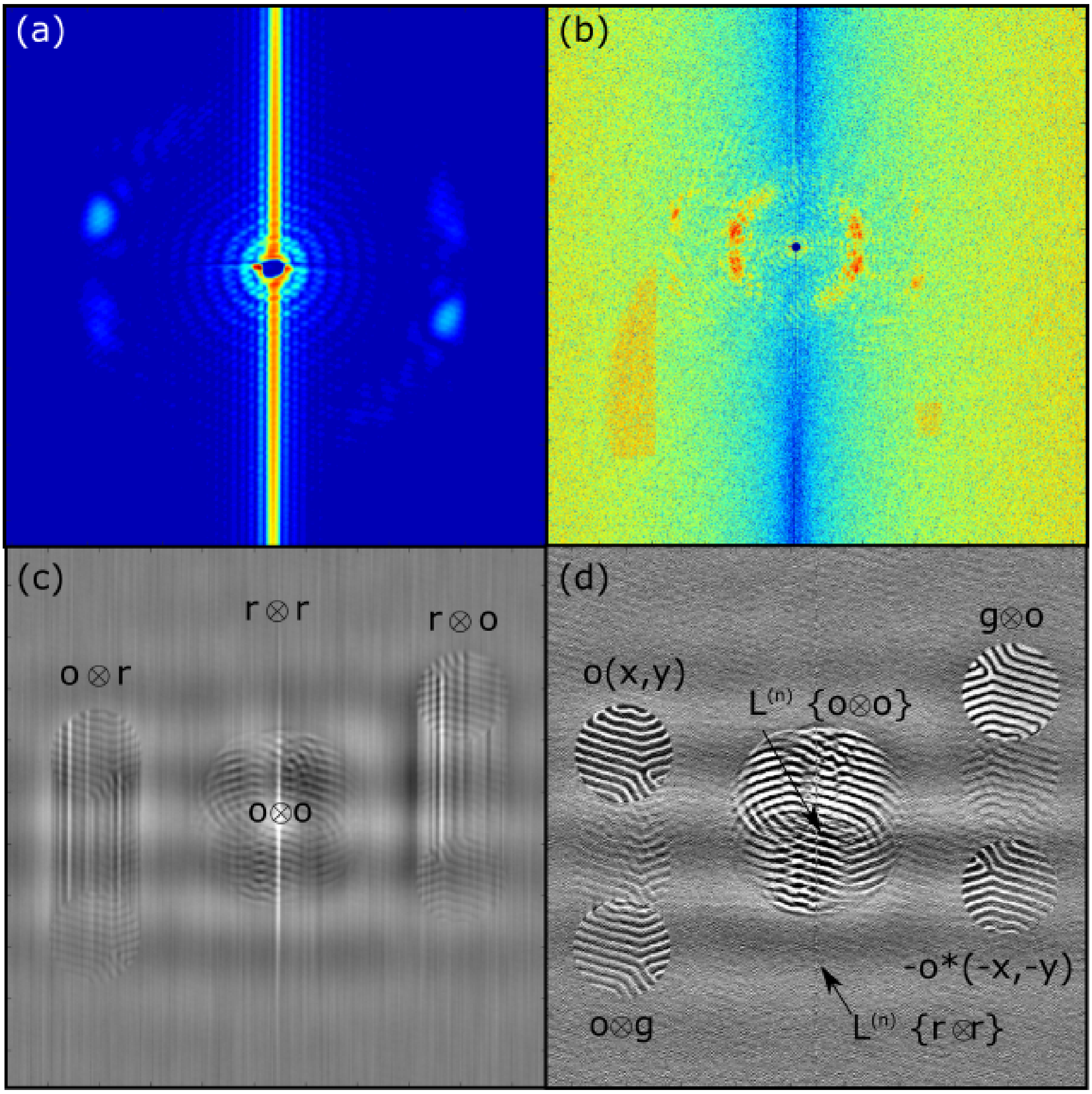

FIGURE 3.13: (a) Zoomed section of raw data corresponding to an hologram produced by x-rays with left circular polarization. In the image we can observe the concentric fringes formed by the interference between the object and reference wave. The large features at the side of the circular pattern corresponds, in this specific case, to the zero diffraction order of a helical phase of the magnetisation in the sample. (b) The results of subtraction and application of the linear differential filter to the hologram. There are some features in the image that does not belong to the interference pattern but to straight light leaking from outside our interest area. These regions are usually removed with the subtraction of both hologram polarisations if they have similar intensity. However, the might introduce some unwanted noise in the final reconstruction. (c) Reconstruction of the subtraction between left and right circular polarized holograms without the application of the differential filter. (d) Reconstruction of the subtraction between left and right circular polarized holograms with the application of the differential filter. The resulting image is the out-of-plane magnetisation of the object. Colormap: blue/back (red/white) corresponds to minimun (maximum) intensity.

Reconstruction process - Coding and practical advices

The reconstruction of the holograms can be done by implementing the theory shown in section 3.1.2 through a computational script. The coding language used to write the script that reconstructed the images shown in thesis is MATLAB®, a matrix-based language, but any programming language can be used to write the script.

Figure 3.16 shows the flux of the steps followed in the reconstruction process. The rest of this section is focused on the explanation of most of the steps and practical advices to obtain a good quality reconstructed image.

- **CCD captures the left-handed (LC) or right-handed (RC) circularly polarised x-ray interference pattern** The x-ray interference pattern is captured by a CCD camera. Let us take the CCD camera as a square matrix of $n \times m$ elements, where each element is a pixel. Each pixel of the CCD camera detects a certain number (N) of photons which are associated to the intensity in each pixel. The intensity recorded for each pixel in each frame depends on many factors such as beam intensity, size of the pinhole used in the set-up, detector gain, and the distance between the CCD and the camera among others. The entire intensity matrix is stored within a data file located in beam-line CCD computer.

- **Retrieval of data from beam-line computers** Each complete measurement takes from 30 to 90 minutes and it is formed by hundreds of frames captured by the CCD camera for each x-ray circular polarisation. Most beamlines have computational scripts that sum all the frames for one polarisation and deliver this as output in a single file, usually a *.nxs* type and $\sim$16 MB size, containing all the measurement details and the single intensity matrix for a single polarisation.

- **Import data files as matrices** The intensity matrix forms part of the structure of the .nxs file. In order to use it within the script it is necessary to import the data. Special care must be taken in importing the matrix as a numeric class *double*

- **Remove *hot pixels*** Each pixel in the CCD camera can be thought of as a well of electrons where the charge is accumulated. Where this potential well reaches its limit, the linear relationship between the light intensity and the signal degrades until the measurement is stopped. This pixel is now called a *saturated* pixel. A saturated pixel appears in a plot of the intensity colormap, a pixel with the maximum intensity possible that we called *hot pixel*. These pixels are produced by external light that leaks into the chamber, non-controlled internal reflections, extra holes in the opaque mask or even cosmic rays. These hot pixels introduce noise in the final reconstructed image and therefore it is necessary to erase them before the normalisation process occurs. An easier way to identify these pixels is to compare their intensity to that of their neighbours. A sharp increase in the intensity between two adjacent pixels might usually indicate a hot pixel. To erase it, it can be replaced by the mean of the closest neighbours, or simply be replaced by 0.

- **Perform background normalisation in both data matrices** Once all the hot pixels are removed, we have to normalise each pixel on both holograms (LC and RC) by the mean value of the background. In order to do this, we selected an area that contains the light coming from the reference slit and the background signal, as the one shown within the yellow rectangle in figure 3.14 (b), and we calculate the mean value of the pixels in that area. Then, each pixel in both holograms are divided by that value.

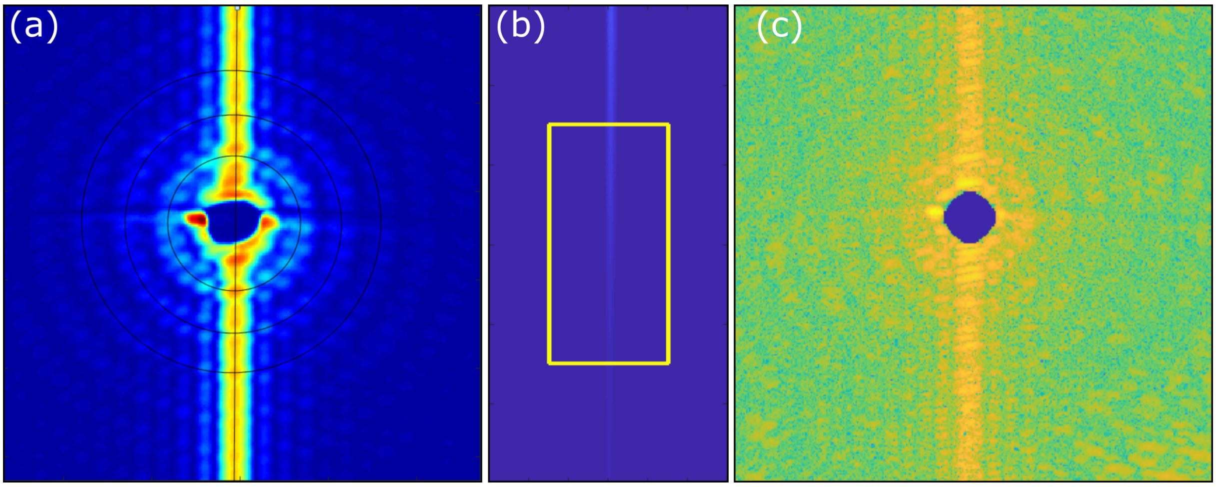

FIGURE 3.14: (a) Using the Airy rings as a guide, it is possible to find the centre of the hologram. (b) The region enclosed in the yellow rectangle is used to normalise each hologram. (c) The blue region edge is a smooth function that covers the rough edge of the beam-stop shadow. Colormap: blue (red) corresponds to minimum (maximum) intensities.

- **Subtract and add LC and RC matrices** To take advantage of the strong XMCD effect in ferromagnetic materials, we must subtract from each other both holograms taken with different polarisations. After doing this, we will have an intensity matrix containing only magnetic information (magnetic hologram), which we will reconstruct. In order to compare the position of the magnetic features with the real image, we use one of the holograms, or the addition of both holograms produced by both polarisations. Reconstructing this new hologram (charge hologram) we will obtain the topography of the sample.

- **Find the pixel corresponding to the centre of the hologram**

  The application of the linear differential operator must be done using the centre of the hologram (and not the centre of the matrix) as zero point. Therefore, it is crucial for a good reconstruction to find the centre of the hologram with a sub-pixel definition. I have used the Airy rings produced by the diffraction of the x-rays through the circular aperture as a guide to draw circles on the top of the them, as it is shown in figure 3.14 (a). It is possible to program a function that finds the centre of each rings, and the centre of the hologram as an average of those values.

- **Remove the beam-stop shadow** A beam-stop is usually positioned in front of the CCD camera to avoid shining straight light onto the detector which can result in permanent damage to it. However, the shadow of this beam-stop is recorded as a non-intensity region in the matrix as the one shown in the centre of the figure 3.14 (a). It has been shown [144] that multiplying the raw data by a function to smooth out the sharp edges at the border of the beam-stop shadow (Figure 3.14 (c) improves the signal-noise ratio of the final reconstruction, eliminating undesired artefacts as concentric rings and parallel strips.

- **Calculate the linear differential operator angle** As we studied in the previous subsection, the linear differential operator for n slit is a directional derivative along the slit. However, the slit is not always fully aligned to the vertical axis of the CCD camera. When this happens, we need to find the angle β between the vertical axis of the CCD camera and the light coming from the slit, as is shown in figure 3.15(a). Knowing the centre of the hologram and the angle that specifies the direction of the slit, we can proceed to apply the linear differential operator (figure 3.15(b)).

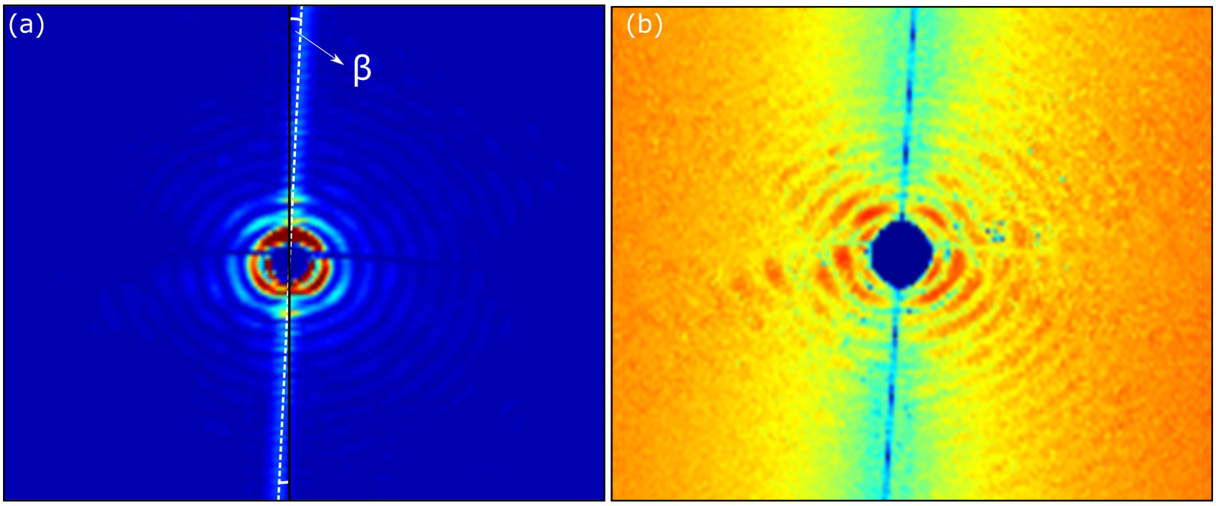

FIGURE 3.15: (a) It is necessary to find the off-set β angule in order to apply the differential filter. (b) Log scale color representation of the intensity matrix after apply the differential filter. Colormap: blue (red) corresponds to minimum (maximum) intensities.

- **Apply an off-centre Fast Fourier Transform to the holograms** The last step is to apply an off-centre Fast Fourier Transform to the holograms operated with the linear differential operator. In MATLAB® we need to apply first a 2D Fast Fourier Transform (*fft2*) and then shift it off centre with *fftshift*, which rearranges a given Fourier transform by shifting the zero-frequency component to the centre of the array.

- **Magnetic and topographic information obtained from the holograms** Displaying the output of the off-centre Fast Fourier Transform as an image allows us to visualise the information needed. The reconstruction of the magnetic hologram gives us the magnetism of the sample and the reconstruction of the magnetic information. The quality of the reconstruction is given by the amount of artefacts and periodic structures non-related with the actual magnetic information.

  Within the script, it is possible to improve the final image by modifying the hologram centre position, the function that removes the beam-stop shadow and the angle of the linear differential operator application. Within the experimental details, it is key to obtain a good quality image to have similar maximum intensity on both LC and RC holograms. This ensures a good subtraction of interference patterns and eliminates artefacts in the magnetism image.

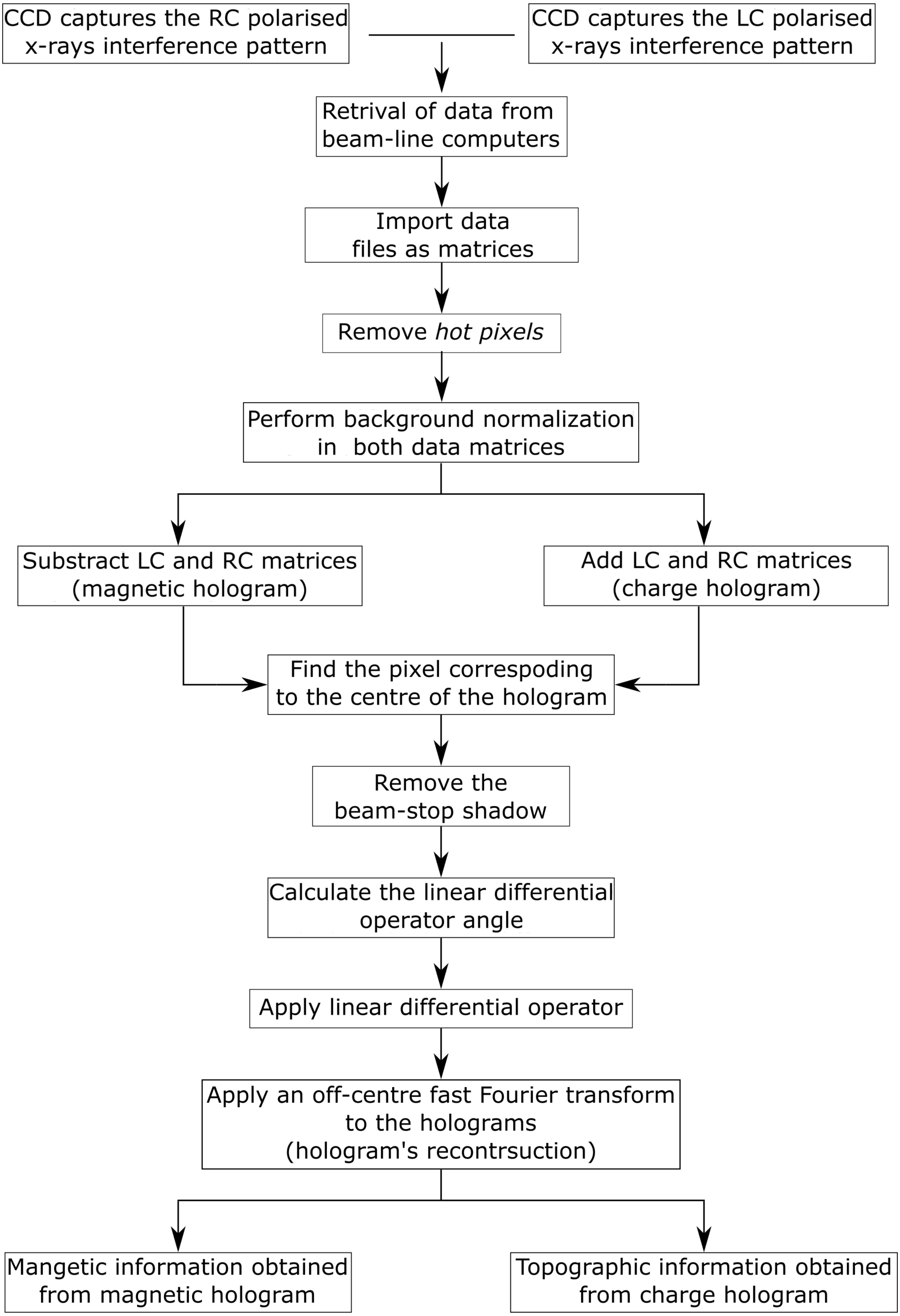

FIGURE 3.16: Flux diagram of the reconstruction steps

3.2 Time resolved scanning Kerr Microscopy

3.2.1 Discovery of the magneto-optics effect

The studies about how light and other forces interact started around the beginning of the 19^{th} century. Scientists were interested in observing the interaction of light with electrical fields and by 1825 null results were reported by Sir John Herschel when he examined the propagation of a beam of polarized light along the axis of a helix carrying an electric current. Further studies by Michael Faraday also showed null results between the interaction of light and electric forces. However, when he used an electromagnet with an iron core, he discover the magneto-optic effect. That day, he wrote in his labbook *"A piece of heavy glass, which was 2 in. by 1.8 in. and 0.5 of an inch thick, being a silico-borate of lead, was experimented with...when contrary magnetic poles were on the same side there was an effect produced on the polarised ray, and thus magnetic force and light were proved to have a relations to each other. This fact will most likely prove exceedingly fertile, and of great value in the investigation of conditions of nature force"*

While Faraday studied light transmission, in 1877 Rev. John Kerr examined the polarization of light reflected from a polished electromagnet pole. His research allowed him to receive the Royal Medal in 1898 making his findings among the most important after Faraday's discovery. These effect are known as the magneto-optical Faraday effect and the magneto-optical Kerr effect, both proportional to the ferromagnetic materials magnetisation $\vec{M}(T)$. Due to its sensitivity, local probing nature and relative experimental simplicity, these effects are widely used as experimental tools in magnetism.

3.2.2 Origins of the Magneto-Optical Kerr Effect

The origins of the magneto-optical effect can be studied in two levels: macroscopically (dielectric theory) or microscopically (quantum theory). Macroscopically, this effect arise from the antisymmetric, off-diagonal elements in the dielectric tensor, which determine the optical properties of a medium. Microscopically, the spin-orbit interaction explains the coupling between the electrical field of the light and the electron spin within a magnetic medium.

Magneto-optical Faraday effect - Macroscopic formulation

The macroscopic formulation of the magneto-optical effect is based on dielectric properties of a medium. In order to probe this effect, a linearly polarized light is passed through the magnetic film studied. The polarization of an electromagnetic wave is defined by the direction of the electric field vector, which is confined to a given plane along the direction of propagation. Maxwell expressed linearly polarized light as being a superposition of two circularly polarized components. The phenomenological explanation says that the Faraday effect is a result of the different propagating velocities of these two circular modes, which gain different phase shifts due to the different propagating velocities resulting in a rotation of the polarization plane, or *Faraday rotation*. In addition, due to the different absorption rates of the medium for the two circularly polarized modes, the ellipticity of these modes is changed. For transparent materials the Faraday rotation is dominant over the ellipticity, but for metals rotation and ellipticity are comparable.

Let's take the dielectric tensor $\tilde{\varepsilon}$, which relates the displacement vector $\vec{D}$ to the electric field according to $\vec{D} = \varepsilon\vec{E}$, and is given by the coefficients ε_{ij} with $i, j = 1, 2, 3$. This can be decomposed into a symmetric and a antisymmetric part, $\varepsilon_{ij} = \frac{(\varepsilon_{ij}+\varepsilon_{ji})}{2} + \frac{(\varepsilon_{ij}-\varepsilon_{ji})}{2}$. Because the symmetric can be diagonalized by rotating the coordinate system, it does not give rise to Faraday effect and we will always assume that it is isotropic with dielectric constant ε_0. In the other hand, the antisymmetric part of the dielectric tensor is

$$\tilde{\varepsilon} = \varepsilon_0 \begin{pmatrix} 1 & iQ_z & -iQ_y \\ +iQ_z & 1 & iQ_x \\ iQ_y & -iQ_x & 1 \end{pmatrix} \tag{3.21}$$

where $\vec{Q} = \{Q_x, Q_y, Q_z\}$ is the magneto optical coupling strength or Voigt vector. The magnetic response of the medium is attributed to the Voigt vector $\vec{Q}$ in the dielectric tensor. Assuming the magnetic permeability is 1, then the relationship between $\vec{D}$ and $\vec{E}$, and $\vec{B}$ and $\vec{H}$ is

$$\vec{D} = \varepsilon\vec{E} + i\varepsilon\vec{E} \times \vec{Q} \quad \text{and} \quad \vec{B} = \vec{H}\,. \tag{3.22}$$

Then Maxwell's equations give

$$\vec{k} \cdot \vec{E} = -i\vec{k} \cdot (\vec{E} \times \vec{Q})\,, \tag{3.23}$$

$$\vec{k} \times \vec{E} = \frac{\omega}{c}\vec{H}\,, \tag{3.24}$$

$$\vec{k} \cdot \vec{H} = 0\,, \tag{3.25}$$

$$\vec{k} \times \vec{H} = -\frac{\omega\epsilon}{c}(\vec{E} + i\vec{E} \times \vec{Q})\,. \tag{3.26}$$

Here, $\vec{D}$, $\vec{H}$ and $\vec{k}$ are perpendicular to each other. However, $\vec{E}$ has a component parallel to the wave vector $\vec{k}$. We can write $\vec{E}$ as

$$\vec{E} = E_s\vec{e}_s + E_p\vec{e}_p + i(-\vec{Q} \cdot \vec{e}_p E_s + \vec{Q} \cdot \vec{e}_s E_p)\vec{e}_k\,, \tag{3.27}$$

where s and p refers to the s- and p- polarization modes, $\vec{e}_s$, $\vec{e}_p$, and $\vec{e}_k$ are unit vectors along the s, p and k directions. The light polarization is described as s (p) when the electric field of the linearly polarised light light is perpendicular (parallel) to the plane of incidence, as is shown in Figure 3.17.

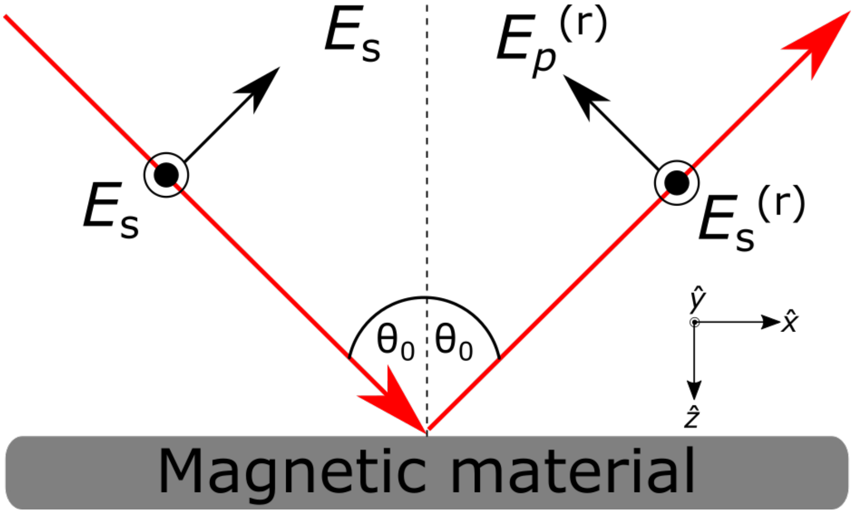

FIGURE 3.17: Plane of incidence of the laser beam onto a magnetic surface, used to define s and p linear polarisation of the light. This geometry is used to calculate the optical reflection coefficients.

E_s and E_p are the s and p components of the electric field, and their equations of motion are

$$\left(\frac{\omega^2\varepsilon}{c^2}\right)E_s + \frac{i\omega^2\varepsilon\vec{Q}\cdot\vec{e}_k}{c^2}E_p = 0 \tag{3.28}$$

$$-\frac{i\omega^2\varepsilon\vec{Q}\cdot\vec{e}_k}{c^2}E_s + \left(\frac{\omega^2\varepsilon}{c^2}\right)E_p = 0\,. \tag{3.29}$$

from where is easy to show that the two normal modes are right (R) and left (L) circularly polarized modes with

$$K_{R,L} = k\left(1 \pm \frac{1}{2}\vec{Q}\cdot\vec{e}_k\right) \quad \text{or} \quad n_{R,L} = n\left(1 \pm \frac{1}{2}\vec{Q}\cdot\vec{e}_k\right) \quad . \tag{3.30}$$

Here $k = \frac{\omega}{c}\sqrt{\varepsilon}$ is the wave vector and $n = \sqrt{\varepsilon}$ is the refraction index without the magnetisation. Any mode of the electromagnetic wave can be viewed as their superposition.

The complex Faraday rotation of the polarization plane after the light has travelled a distance L through the medium is

$$\theta = \frac{\pi L}{\lambda}(n_L - n_R) = \frac{\pi L n}{\lambda}\vec{Q}\cdot\hat{k}\,. \tag{3.31}$$

The real part of eq. (3.31) gives the rotation, and the imaginary part gives the ellipticity.

The samples studied in this thesis are opaque and therefore is not possible to measure Faraday rotation. Instead, is convenient to measure the reflected light in order to measure the magneto-optic response.

Magneto-optical Faraday effect - Macroscopic formulation

The reflective electric field components $E_p^{(r)}$ and $E_s^{(r)}$ of the elliptically polarised light can be described in terms of the incident electric field components E_p and E_s by using the Jones Matrix formalism

$$\begin{pmatrix} E_s^{(r)} \\ E_p^{(r)} \end{pmatrix} = \begin{pmatrix} r_{ss} & r_{sp} \\ r_{ps} & r_{pp} \end{pmatrix} \begin{pmatrix} E_s \\ E_p \end{pmatrix} \tag{3.32}$$

where r_{ij} are the optical reflection coefficients. Using the geometry show in Figure 3.17, and retaining terms to the first order in Q, the Voigt parameter, the reflection coefficients are the following [145]

$$r_{ss} = \frac{n_0 \cos\theta_0 - n_1 \cos\theta_1}{n_0 \cos\theta_0 - n_1 \cos\theta_1}, \tag{3.33}$$

$$r_{pp} = \frac{n_1 \cos\theta_0 - n_0 \cos\theta_1}{n_1 \cos\theta_0 - n_0 \cos\theta_1} + \frac{2iQn_0 \cos\theta_0 \sin\theta_1 u_y}{(n_1 \cos\theta_0 + n_0 \cos\theta_1)^2}, \tag{3.34}$$

$$r_{ps} = -\frac{i1n_0 n_1 \cos\theta_0 (\sin\theta_1 u_x + \cos\theta_1 u_z)}{\cos\theta_1 (n_0 \cos\theta_0 + n_1 \cos\theta_1)(n_1 \cos\theta_0 + n_0 \cos\theta_1)}, \tag{3.35}$$

$$r_{sp} = \frac{iQn_0 n_1 \cos\theta_0 (\sin\theta_1 u_x - \cos\theta_1) u_z}{\cos\theta_1 (n_0 \cos\theta_0 + n_1 \cos\theta_1)(n_1 \cos\theta_0 + n_0 \cos\theta_1)}, \tag{3.36}$$

where $\vec{u} = \vec{M}/M_s$, θ_0 and θ_1 are the angles of incidence and refraction, and n_0 and n_1 are the refractive indices of the initial and final media.Finally, the Kerr rotation ϕ' and ellipticity ϕ'' for $s-$ and $p-$polarised light are given by

$$\phi_s = \phi'_s + i\phi''_s = \frac{r_{ps}}{r_{ss}} \quad \text{and} \quad \phi_p = \phi'_p + i\phi''_p = \frac{r_{sp}}{r_{pp}}. \tag{3.37}$$

In non-magnetic materials the polarisation of incident $p-$ or $s-$polarised light remains unchanged after being reflected by the non-magnetic surface because r_{ps} and r_{sp} are zero and r_{ss} and r_{pp} are non-zero and complex. In a magnetic material, r_{ps} and r_{sp} are also non-zero and complex which induces a electric field in the reflected light in the orthogonal direction of the polarisation of the incident light.

Quantum theory - Microscopic formulation

Previously we described the change of polarisation of light passing through (or being reflected from) a material by means of the dielectric tensor and its antisymmetric part. If we go further in the microscopic understanding of what determines the properties of the dielectric tensor, we will find that it is determined by the motion of the electrons in the medium. When a beam of light propagates through a medium, the electrical field of the light generates the motion of the electrons in the medium. We previously discussed that the polarization of a linearly polarised beam can be decomposed as a superposition of left and right circularly polarised modes. Each mode will drive electrons into left and right circularly polarised movement. In an isotropic medium, the radius of gyration will be the same for both polarisation, and there will not be difference in the dielectric constants for left and right circularly polarised waves thus no Faraday rotation will be measured. However, if a magnetic field is applied in the propagation direction of the light beam, a Lorentz force will be exerted in each electron. The Lorentz force takes into account the gyration polarisation of the electron and it will points toward or away from the circle's centre. This difference in the radii of the left- and right-circularly polarised modes will give different dielectric constants for each mode and therefore generates an Faraday effect. Regarding the fact that this explanation works in all materials, it does not answer why the magneto optical effect is much stronger in ferromagnetic materials that other materials. The first attempts to explain this assume that ferromagnetic materials have an effective field, rather than the applied field, that determines the Faraday rotation. Voigt postulated a effective field of the order of $10^6 - 10^7$ Oe to produce such Faraday rotation. This magnitude of this effective field was the same order of the one that Weiss postulated in order to explain ferromagnetism. Heisenberg correctly explained the existence of the so called effective field due the exchange interaction between electrons as a purely quantum mechanical effect. However, this was not enough to explain the Faraday effect because this field is not coupled to the movement of the electrons which determines the dielectric properties of a material. It was Hulme, in 1932, who pointed out that it is the electron spin is coupled to its motion by the spin-orbit interaction. This coupling, $\sim (\nabla\vec{V} \times \vec{p}) \cdot \vec{s}$, results from the interaction of the electron spin with the magnetic field the electron *sees* as it moves through the electric field $-\nabla\vec{V}$ with momentum $\vec{p}$ inside a medium. Is through this coupling that the magnetic and optical properties of a ferromagnet are connected, and the effect is strong due to the imbalance of spin-up and spin-down electrons at the Fermi level in these materials as we saw in the previous section.

3.2.3 Experimental detection of the magneto-optical Kerr effect

Depending of the polarisation of the incident light (E_s or E_p) and the orientation of the the magnetisation $\vec{M}$ of the sample we can define three fundamental Kerr geometries: Polar, Longitudinal and Transverse, as are shown in Figure 3.18. Table 3.2 presents the definition of each geometry based on the magnetisation direction relative to the plane of incidence of the light beam, showing the reflecting interface and the light polarisation needed to measure such signal.

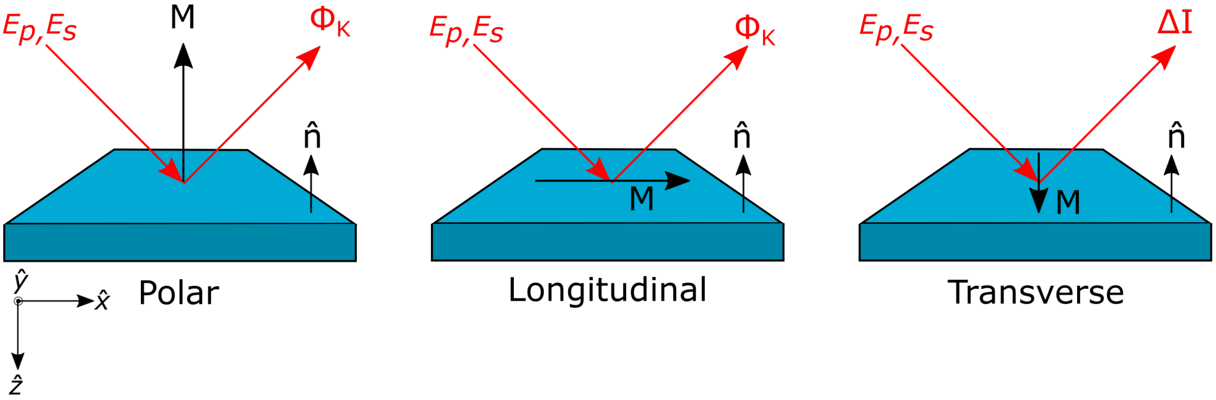

FIGURE 3.18: MOKE geometries: polar, longitudinal, and transverse.

In the polar and longitudinal geometry, the Kerr effect leads to a magnetisation-dependant rotation Φ_k of the major axis of the elliptically polarised reflected light. However, in the transverse geometry, using $p-$ polarised light does not result in a polarisation rotation since $\vec{M}$ is perpendicular to the plane of incidence and $\vec{E}$. Instead, it give rise to a $\vec{M}$-dependent change in reflectivity ΔI. For s-polarised light $\vec{E}$ is parallel to $\vec{M}$, which does notyield a magneto-optical effect.

Detection of the magneto-optical Kerr effect

In this thesis, we use MOKE to determine the magnetisation dynamics of vortices and anti-vortices in spin transfer vortex oscillators. Vortices are quite complex magnetic structures presenting magnetisation components in all three spatial directions. We

	Polar	Longitudinal	Transverse
Direction of $\vec{M}$ relative to plane of incidence	Parallel	Parallel	Perpendicular
Direction of $\vec{M}$ relative to reflecting interface	Perpendicular (Out-of-plane)	Parallel (in-plane)	Parallel (in-plane)
Required polarisation of incident light	$p-$ or $s-$polarised ($r_{sp} = r_{ps}$)	$p-$ or $s-$polarised ($r_{sp} = -r_{ps}$)	$p-$polarised (r_{pp})

TABLE 3.2: Definition of polar, longitudinal, and transverse geometry in relation to the direction of magnetisation of the film with the plane of incidence and the reflecting interface, and the polarisation require to measure each geometry.

have shown that there are three MOKE geometries that can be used to detect the magnetisation and for the vortex case, we use all three. In general, the chosen geometry for an experiment will depend upon the sample, behaviour of the magnetisation, and detection technique. Due the size of the analysed magnetic structures, a microscope objective lens was required to focus the probe laser onto the region of interest in the sample. A focused laser will have rays forming a cone, which is formed of planes of incidence at all azimuth angles with a range of angle of incidence. At normal incidence only the polar Kerr effect can be sensed, which is sensitive to the out of plane component of the magnetisation. However, it has been shown [146] that even at angles of incidence away from the normal, the polar Kerr effect can be measured. In order to use the longitudinal Kerr effect, which is sensitive to the in-plane magnetisation, we need to modify the usual single photo-detector detection technique. In Figure 3.19 a schematic of the experimental geometry of the scanning Kerr microscope used in the time-resolved experiments is shown. Before entering to the microscope objective, the beam is expanded by a factor of ten in order to reduce the beam divergence and enhance the spatial resolution of the technique. After passing an aperture to define the beam diameter, the beam is passed through a linear polariser to define its polarization. The polarisation of the beam is either vertical or horizontal with respect to the plane defined by $a - a'$ and $b - b'$. Finally, the beam is focused by the objective lens to a spot of diameter defined by the diffraction limit. The same objective lens collects and re-collimate the reflected beam, which is sampled using a non-polarising beam-splitter.

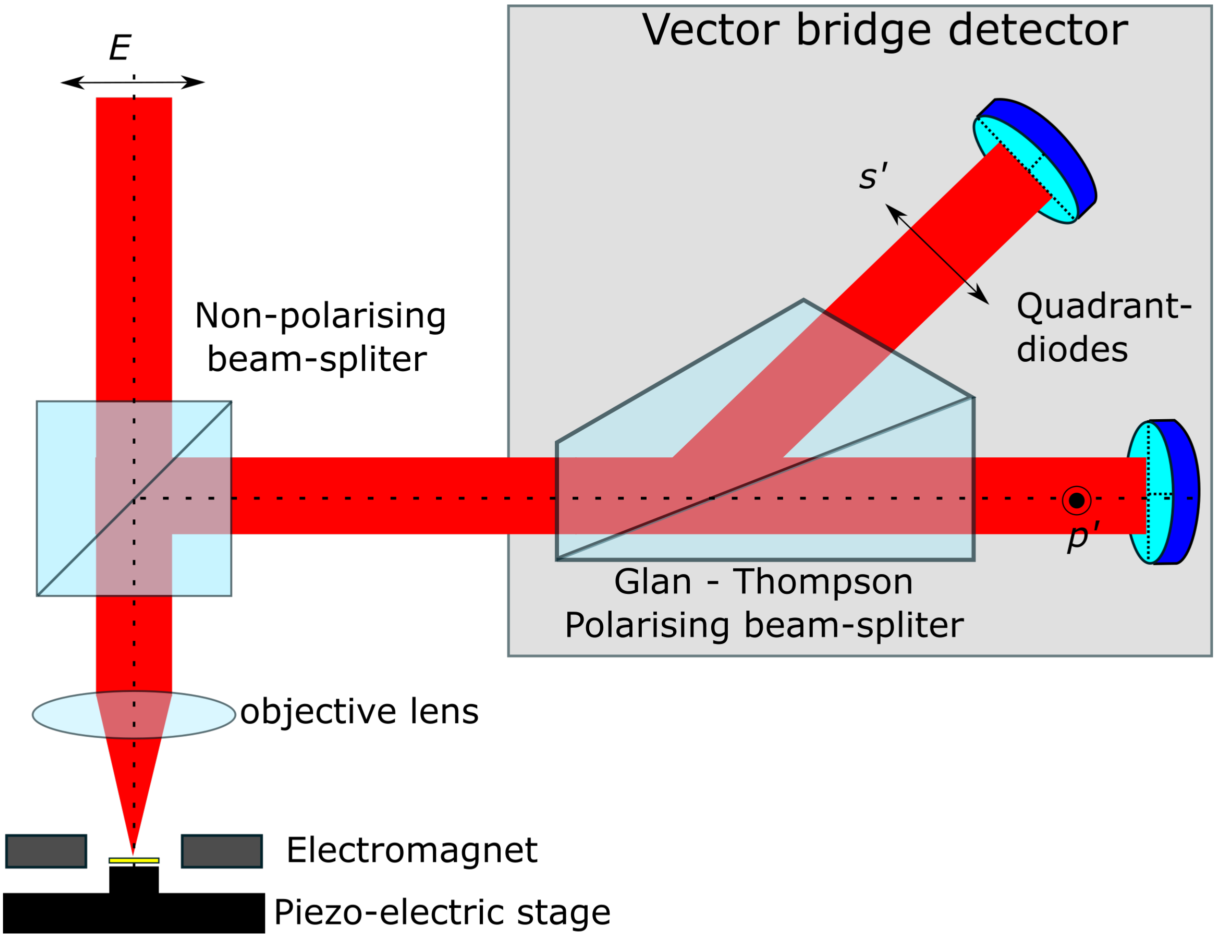

FIGURE 3.19: Schematic of the scanning microscope MOKE geometry. The vector bridge detector is shown with its main components: the Glan - Thompson polarsing beam-spliter and the two quadrant-diodes.

In this thesis, a Glan-Thompson polarising beam-splitter and two quadrant-diode detectors (quad-detectors) that were contained within a vector bridge detector that was used to measure three orthogonal components of the vector magnetisation simultaneously, two in-plane components, parallel ($M_{||}$) and perpendicular ($M_{\perp}$) to the applied in-plane field $\vec{H}$, and an out-of-plane component (M_z).

The Glan-Thompson polarising beam-splitter is built by cementing two birefringent prisms of calcite together so that the optical axes of the crystals are parallel. The refractive index along the directions perpendicular and parallel to the optical axes of a calcite crystal are different ($\mathrm{n}_{||} < \mathrm{n}_{\perp}$) . Since $\mathrm{n}_{||} < \mathrm{n}_{\perp}$ the critical angle for total internal reflection of the ray with parallel $\vec{E}$ to the optical axis is larger than that for the perpendicular $\vec{E}$. This produced that the angle of incidence of rays of the two polarisations componets are such that one is transmitted, while the other is totally internally reflected. This optical item is design to separates the light reflected from the sample into two beams of orthogonal polarisation separated by an angle of 45°, as is shown in Figure3.19

Each quadrant-photodiode has a total area of 50 mm^2 and a responsivity of 0.55 A/W at a wavelength of 800 nm. Typically a 6 mm spot diameter was used, determined by the rear aperture of the microscope objective (6.5 mm). It is important to have a spot size larger than the width of the inactive gap between the quadrants of the photodiodes. The current produced in each photodiode quadrant Q_i is converted to a voltage signal using trans-impedance amplifiers with a gain of $10^4\Omega$ [147].

Figure 3.20 shows the cone of rays focused onto the sample by the microscope objective, which is divided into four parts. When the beam is centred in the quad-detector each quadrant measures one of the four parts of the beam, arbitrarily labelled a, b, c, and d. Each half of the beam is reflected back through the opposite half: $a + b \rightarrow c + d$ and $a + d \rightarrow b + c$ for instance. Then, each quad-detector QD_i with $i = 1, 2$ will measure an intensity $I_{(a,b,c,d)_i}$. The longitudinal component of the Kerr rotation, sensitive

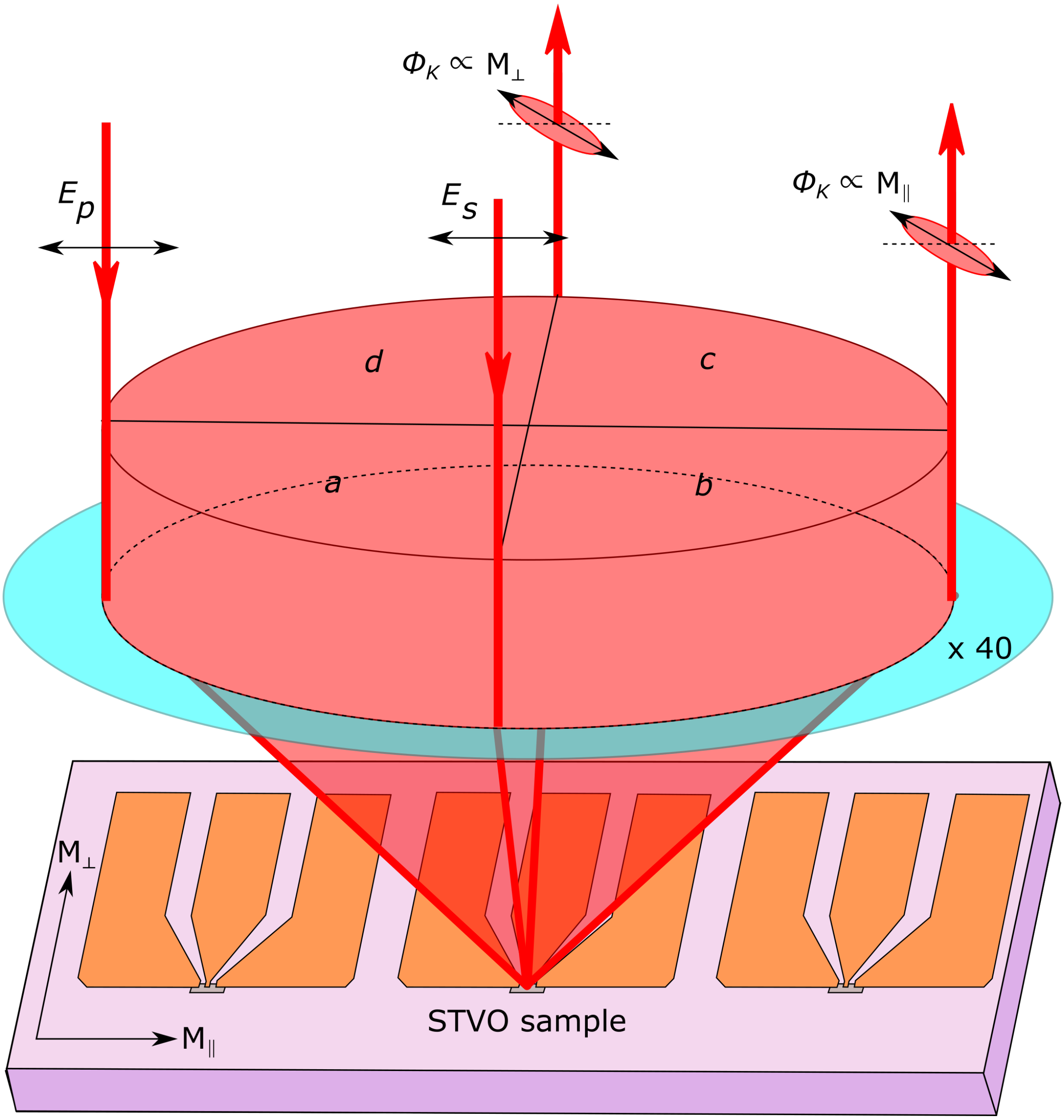

FIGURE 3.20: Schematic of the geometry of the probe laser focused upon the sample. The ray paths highlighted show planes of incidence for a linearly polarised beam where the incident light is $p-$ and $s-$polarised.

to M_x is given by

$$\Delta I_x = I_{c_2+d_2} - I_{c_1+d_1}\,, \tag{3.38}$$

$$\Delta I_{-x} = I_{a_2+b_2} - I_{a_1+b_1}\,. \tag{3.39}$$

$$\tag{3.40}$$

The Kerr rotations induced on opposite halves of the reflected beam are equal in magnitude and opposite in sign. Therefore

$$|\Delta I_x - \Delta I_{-x}| = 2|\Delta I_x|\,. \tag{3.41}$$

give us the longitudinal component of the Kerr rotation due to M_x.

In the same way, the longitudinal component of the Kerr rotation, sensitive to M_y is given by

$$\Delta I_y = I_{a_2+d_2} - I_{a_1+d_1}\,, \tag{3.42}$$

$$\Delta I_{-}y = I_{b_2+c_2} - I_{b_1+c_1}\,, \tag{3.43}$$

$$|\Delta I_y - \Delta I_{-y}| = 2|\Delta I_y|\,. \tag{3.44}$$

Finally, if we add the four quadrant together, the longitudinal component will disappear, allowing us to measure the polar Kerr rotation due M_z by

$$|\Delta I_z| = I_{a_2+b_2+c_2+d_2} - I_{a_1+b_1+c_1+d_1} \tag{3.45}$$

This detection scheme provides an output signal that is proportional to twice the Kerr rotation. In addition, any non-magnetic intensity change produced by depolarisation effects in the microscope objective, or background noise is removed by the difference operation.

3.2.4 Time resolved scanning Kerr microscopy

In order to produce time-resolved measurements of the magnetisation dynamics using MOKE, we used a mode-locked Ti:sapphire laser (Spectra-Physics Tsunami) with 80 MHz repetition rate. The Tsunami beam had a diameter of 2 mm and a divergence of $\sim$ 1 mrad. It produce pulses of a sub 100 fs duration at a wavelength of $\sim$800 nm, with a power of ∼ 0.6 W (∼ 8 nJ per pulse). A detailed explanation of the mode-locking and the specifications of the equipment can be found in [147]. The diameter of the pulsed laser was expanded ×5 and then the beam was linearly polarized, and focused to a diffraction limited spot onto the spin-valve mesa using a ×60 (0.85 numerical aperture) microscope objective lens. This provides a spatial resolution of ∼ 500 nm.

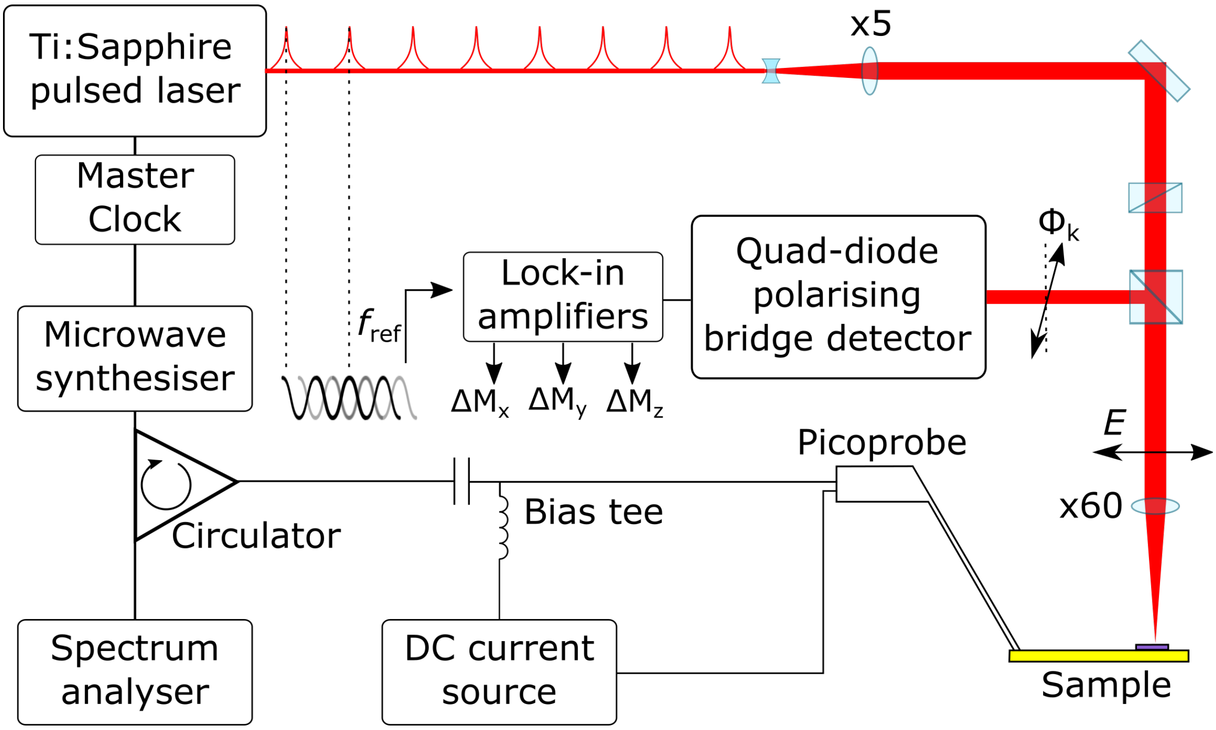

FIGURE 3.21: Experimental set-up of a time resolved scanning Kerr microscope.Reproduced from [148]

The set-up of the time-resolved scanning Kerr microscope (TRSKM) apparatus used to obtain the results of chapter 6 is shown in Figure 3.21. A microwave synthesiser is used to lock the magnetisation dynamics of the STVO to a multiple of the integer multiple of the laser repetition rate. In order to synchronise the microwave synthesiser with the laser we used a master clock with an 80 MHz output, which was used to phase lock the laser by tunning its cavity length. The stroboscopic measurements were done by modifying the relative time delay between the pump, in this case the RF current, and the probe. This was achieved by varying the optical path length of the of the beam using a hollow Au retro-reflector mounted on a 600 mm stepper motor stage. The corresponding total time delay was 4 ns. Each image was acquired at a fixed phase of the RF injected current, which was phase modulated from 0 to 180° at $\sim$ 3 KHz for phase sensitive detection of the corresponding change in the magnetisation [148]. The device studied was scanned relative to the focused beam by using a piezoelectric stage on the device holder. Finally the vector bridge detector captured both components of the longitudinal MOKE signal, and the polar MOKE signal, which were recovered at the modulation frequency by three lock-in amplifiers.

3.3 Summary

In summary, I have introduced the necessary knowledge for understanding the two main imaging techniques used in this thesis. First, I have reviewed the origin and development of x-ray holography and the experimental and theoretical background necessary to perform holography with extended reference by autocorrelation linear differential operator. I have described in detail how to build a suitable sample for HERALDO and the steps to perform the measurements and subsequent reconstruction of the hologram. Secondly, I have reviewed the origin of the magneto-optical Kerr effect. I have shown the different geometries of MOKE and the experimental and theoretical background necessary to perform time resolved scanning Kerr microscopy. In the following chapters I will present the results obtained with these techniques when applied to devices that present interesting magnetic structures, with dynamics driven by a spin transfer torque and/or external magnetic fields.

Chapter 4

Single Layer Spin Transfer Oscillator

While the majority of NC-STO devices exploit giant magneto-resistance (GMR) trilayer systems, in order to achieve large STT [41, 42, 149, 150], a number of similar effects were demonstrated in devices based upon single ferromagnetic layers [88, 89]. Theory predicts [93, 94] that a spin torque, of similar strength to that obtained with GMR materials, can be achieved via asymmetric spin-accumulation at the different interfaces of a single layer ferromagnetic pillar [88, 89]. In a paper of 2013 by S. Sani [94], it was suggested that NC-STO devices can also be realized on extended single-layer ferromagnetic films. Experiments carried out on a Pd(5)/Cu(20)/$Ni_{81}Fe_{19}$(7)/Cu(2)/Pd(2) (thicknesses in nm) stack, showed that a microwave signal can be generated with power and line width values comparable to those achieved with GMR materials. Moreover the microwave emission did not require application of an external magnetic field, making it much more favourable for technological applications.

Although the observed effect is obviously related to the magnetization dynamics in the $Ni_{80}Fe_{20}$ magnetic free layer, the exact nature of the dynamics is not well understood. Given the range of the generated microwave frequencies, which may be as low as 250 MHz, it has been suggested that the emitted signal must originate from the gyrotropic motion of vortices, which have been commonly observed for equivalent NC-STO devices based on GMR materials. However, the observation of microwave emission at frequencies up to 3 GHz appears incompatible with the gyration of a single vortex. Instead this behavior was ascribed to the repeated creation and annihilation of a vortex-antivortex (V-AV) pair underneath the nano-contact [151]. Moreover, it was proposed that the process could involve two V-AV pairs with opposite polarizations [152].

In this chapter we investigate the magnetization dynamics of a single layer NC-STO by means of the recently developed soft x-ray imaging technique known as HERALDO, introduced in chapter 3, section 3.1. This technique can provide high spatial resolution (20 nm) with immunity to mechanical and thermal drifts. A particular advantage of HERALDO compared to the standard Fourier Transform Holography (FTH), is its ability to image both 'out-of-plane' and 'in-plane' components of the magnetization. This is of direct relevance to systems containing magnetic vortices where both in and out of plane magnetization components are present.

4.1 Experimental procedure

4.1.1 Sample

A non-magnetic/ferromagnetic/non-magnetic stack of composition Pd (5)/Cu(20)/$Ni_{81}Fe_{19}$(7)/Cu(2)/Pd(2) (thicknesses in nm) was built on top of a Si3N4 membrane using the procedure described in references [94]. The lithographically integrated nano contact (NC) used to drive current through the device had 100nm diameter. Figure 4.1 shows a schematic of the device and the co-planar waveguide (CPW) used to supply the current. To obtain a holographic image, the sample has a slit of 35nm width and 6μm length that is separated from the imaged area by a distance of 11 μm, which is within the x-ray coherence length.

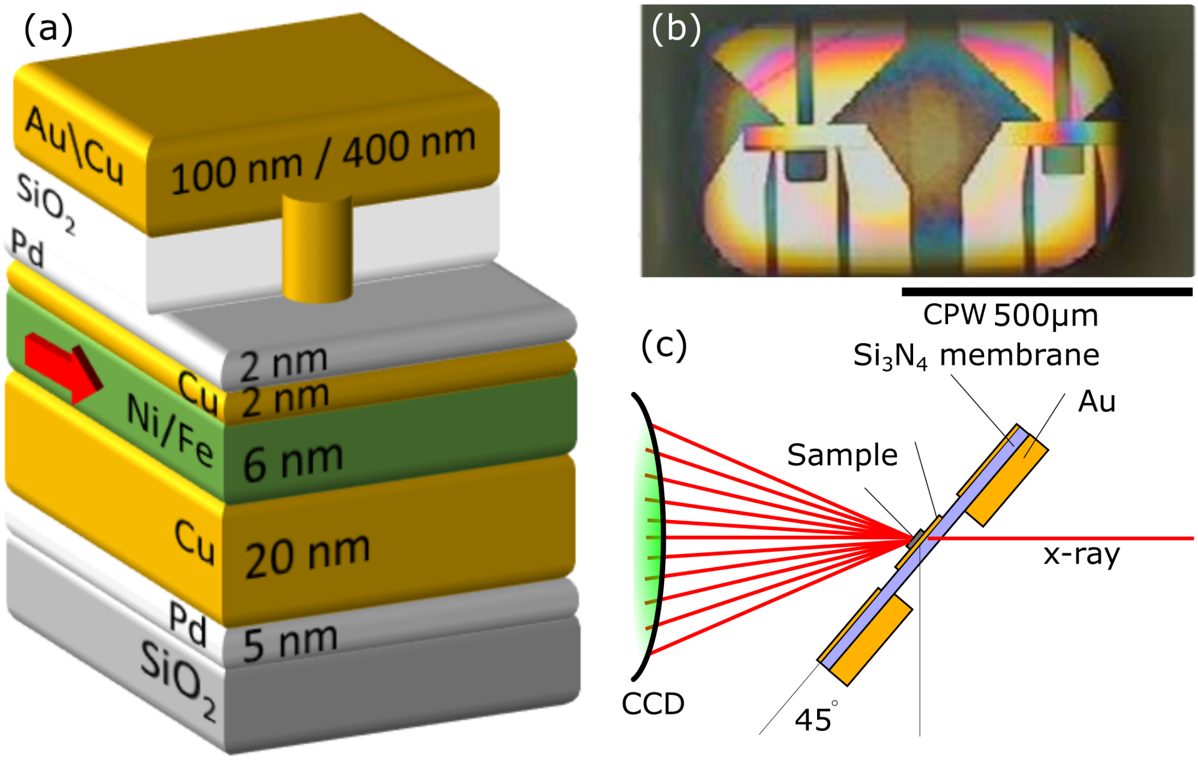

FIGURE 4.1: Schematics of a single layer NC-STO, (a) layer composition. The red arrows represents the in-plane magnetisation of the free layer, (b) Coplanar waveguide (CPW) with the NC-STO fabricated on a Si_3N_4 membrane for imaging at 45 degrees incidence by HERALDO, (c) Layout of the sample in case of off-normal orientation with the beam. This configuration allow us to obtain in-plain component of the free layer magnetisation

4.1.2 Electrical measurements

Transport measurements were performed in a custom probe station. A DC bias current from a Keithley 6221 current source was passed through the NC and between the signal and ground lines of the surrounding coplanar waveguide (CPW) structure through the DC port of a bias-tee, while the microwave signal generated by the STT effect was measured simultaneously through the AC port. The microwave signal was input to a a 100 MHz - 4 GHz AtlanTec amplifier and recorded by a Agilent E448A spectrum analyser.

4.1.3 HERALDO measurements

In order to image the magnetization dynamics of the sample, soft x-ray holography was performed using the HERALDO technique that was previously used to image static magnetic vortices [134, 151, 153]. Measurements were made at the SEXTANTS beamline at the SOLEIL Synchrotron (Paris, France) in order to obtain a highly coherent x-ray beam. Samples grown on Si3N4 membranes allow transmitted x-rays to pass to a CCD camera, positioned on the optical axis behind a beam-stop that removes the direct beam. The interference pattern of the beam transmitted by the sample and the reference slit are recorded on the CCD camera as is shown in Figure 4.1(c). By taking directional derivatives of the Fourier transform of the raw data, the real space image may then be recovered [134].

4.2 Results and Analysis

Figure 4.2 shows the characteristic voltage spectral density of the - microwave signal generated by a single layer NC-STO with 110 nm contact diameter when the current is swept from -30 mA to 0 mA. Up to 3 harmonics of the fundamental frequency signal are observed, as well as mode transitions at -20 mA, -15 mA and -7mA. The linewidth decreases substantially from 36 MHz to 10 MHz as the current is decreased from -23.5 mA to -12.5mA, while the microwave frequency exhibits a quasi-linear dependence on current for values between -15mA and -7mA. All the observed features of the signal, including a hysteretic dependence of the frequency upon current, a continuous monotonic dependence of frequency upon current, and a broad range of emission frequencies (150 MHz – 2GHz) are consistent with the suggested mechanism of V-AV creation and annihilation under the NC induced by the Oersted field [6]. For current values less than that required for nucleation, the V- AV creation and annihilation is expected to stop, with the generated microwave power increasing due to the continuous motion of a single vortex.

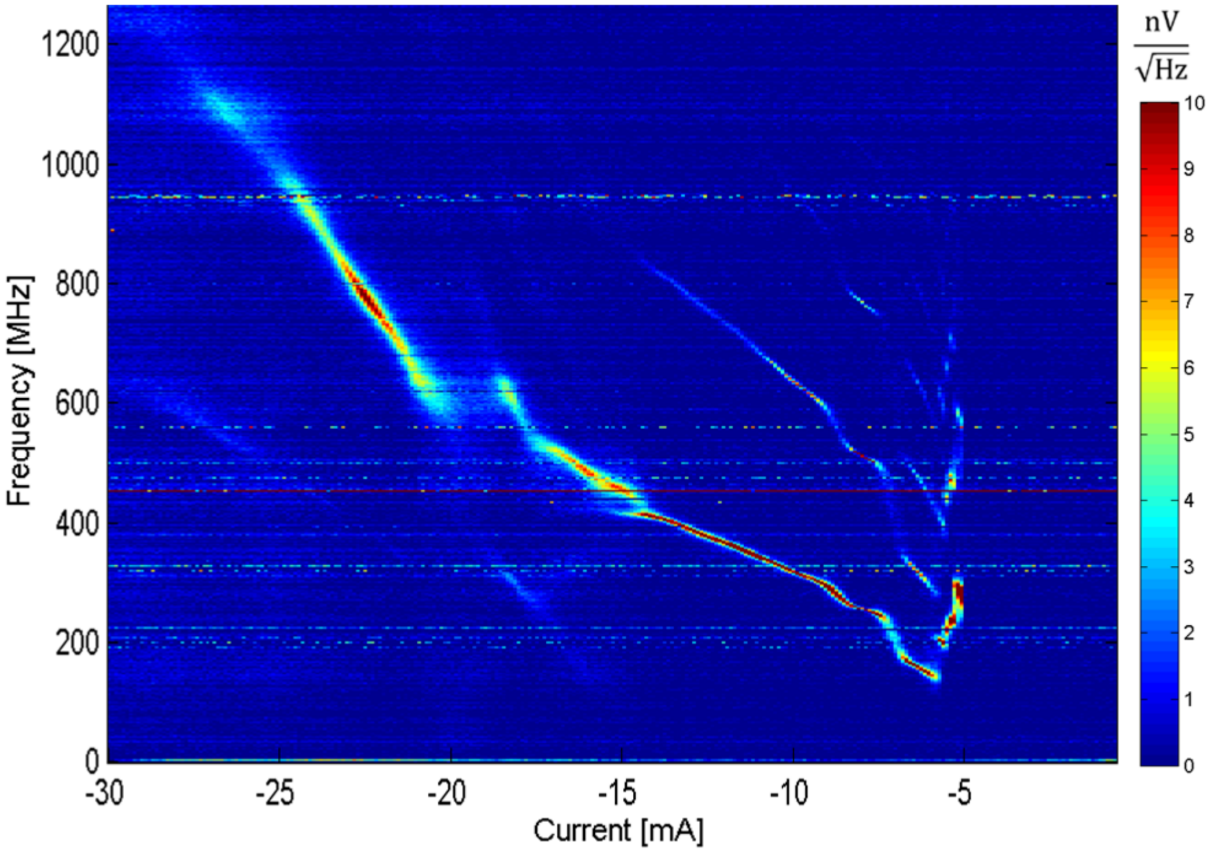

FIGURE 4.2: Dependence of the microwave frequency on DC current for a SL STO with 110 nm nano-contact diameter. The current was varied from -30 mA to 0mA at zero applied magnetic field.

In order to observe the vortex dynamics in the sample, images were acquired, using the HERALDO technique, from devices with 100nm and 50nm contact diameter. The magnetic state was imaged for different values of the DC current with x-rays of 706.5 eV energy incident at 45 degrees to the sample normal, with the plane of the incidence lying in the horizontal direction within the image. The energy used corresponds to the L3 Fe edge and was used in order to obtain the magnetic information from the NiFe layer. Figure 4.3 shows the holograms reconstructed from difference interference patterns acquired at current values of -24mA and 24mA. The difference interference patterns are obtained by subtracting interference patterns acquired with positive and negative circular x-ray polarization, each of which is the average of $\sim$ 800 exposures of 60ms duration. Both current polarities show magnetic contrast suggestive of vortex formation just within the edge of the aperture within the gold layer. The polarity of the contrast, and hence the orientation of the magnetization within the vortex, are seen to reverse with the polarity of the current as might be expected. As well as the vortex-like feature, contrast reminiscent of a domain wall is observed along the rim of the aperture. The measurements without the DC current showed no contrast. Measurements at lower currents showed similar effects though with reduced contrast.

Micro-magnetic simulations [151, 154] have studied the vortex nucleation and behaviour within magnetic NCs systems. These micro-magnetic simulations consist of solving the LLG - Slonczewski and Thiele equations to minimise the magnetic energy in multilayer systems and resolve the equation of motion of magnetic vortices. These studies have shown that it is possible to nucleate a magnetic vortex along an anti-vortex in the nano-contact area. When any of these structures escape that area, they are artificially pinned by the grid edge in the simulations. It is predicted that material defects will lead to similar pinning in the experimental system. Based on these works, we can interpret our results as follows: the vortex structure is observed some way from the NC, which is positioned near the middle of the aperture. It is therefore expected that a V-AV structure is initially formed underneath the NC, before the vortex is ejected due to the large gradient in the confining potential associated with this relatively large current value. The vortex then becomes pinned at the rim of the aperture. It is likely that the magnetic layer is highly stressed at the rim due to the physical removal of the gold layer behind the Si_3N_4 membrane. The mechanical stress along the rim is likely to cause a sharp variation in the potential experienced by the vortex causing it to become pinned. Due to the reproducibility of this observation for both orientations of the current, we ascribe this effect to the Oersted field generated by the DC current rather than the STT effect.

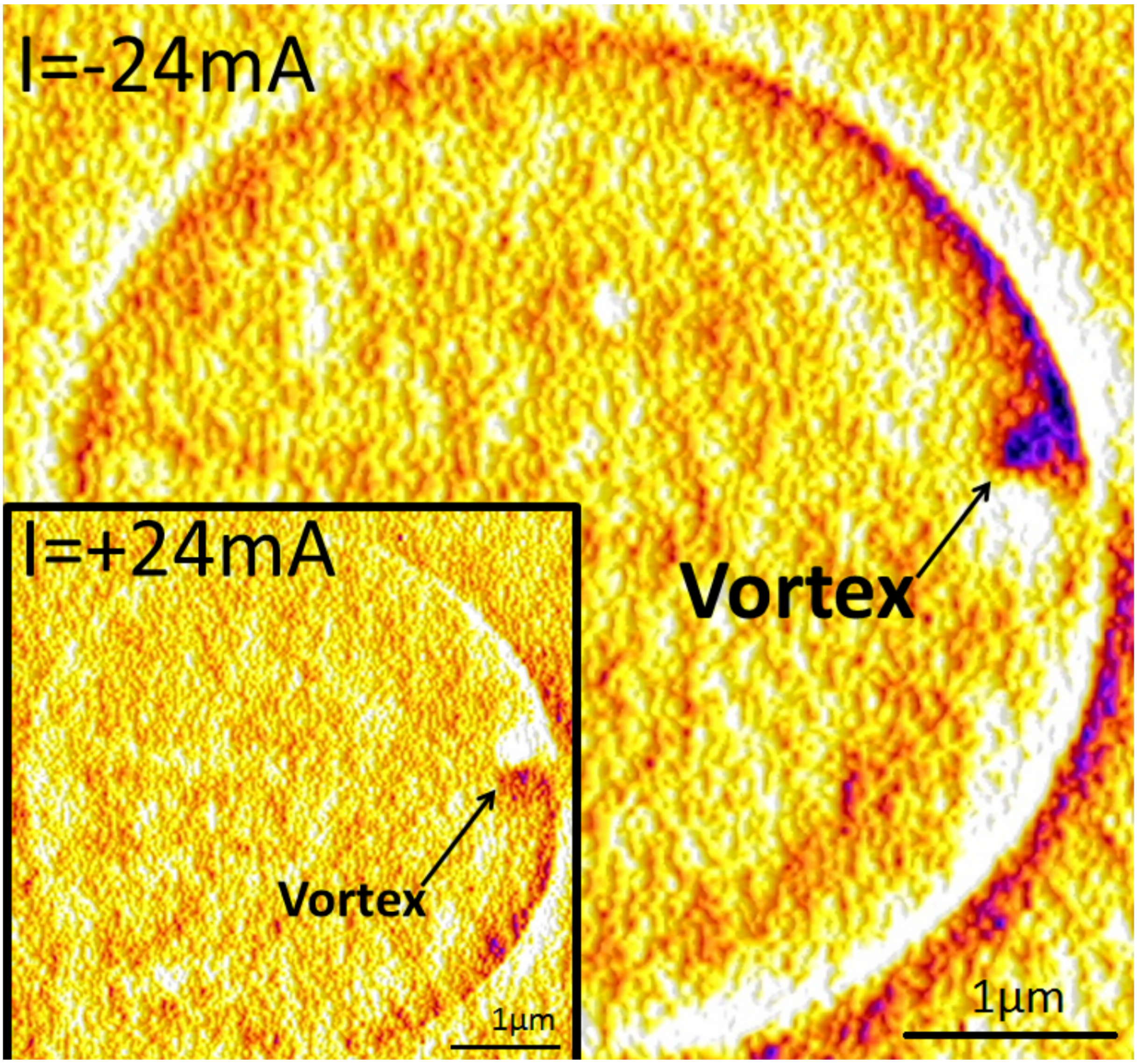

FIGURE 4.3: Dependence of the microwave frequency on DC current for a SL STO with 110 nm nano-contact diameter. The current was varied from -30 mA to 0mA at zero applied magnetic field. Colormap: blue and white correspond to a oposites direction of the in-plane magnetization.

At lower currents, close to the point that the microwave signal disappears, it is expected that the V-AV dynamics will remain under or within the vicinity of the NC. Figure 4.4 shows magnetic images acquired at current values of -1mA and -5mA from a SL STO device with ~50nm NC diameter. The observed features may indicate magnetization dynamics in the region where the NC is positioned (red arrow in Figure 4.4). Due to the time-averaged nature of the measurements it is not possible to determine

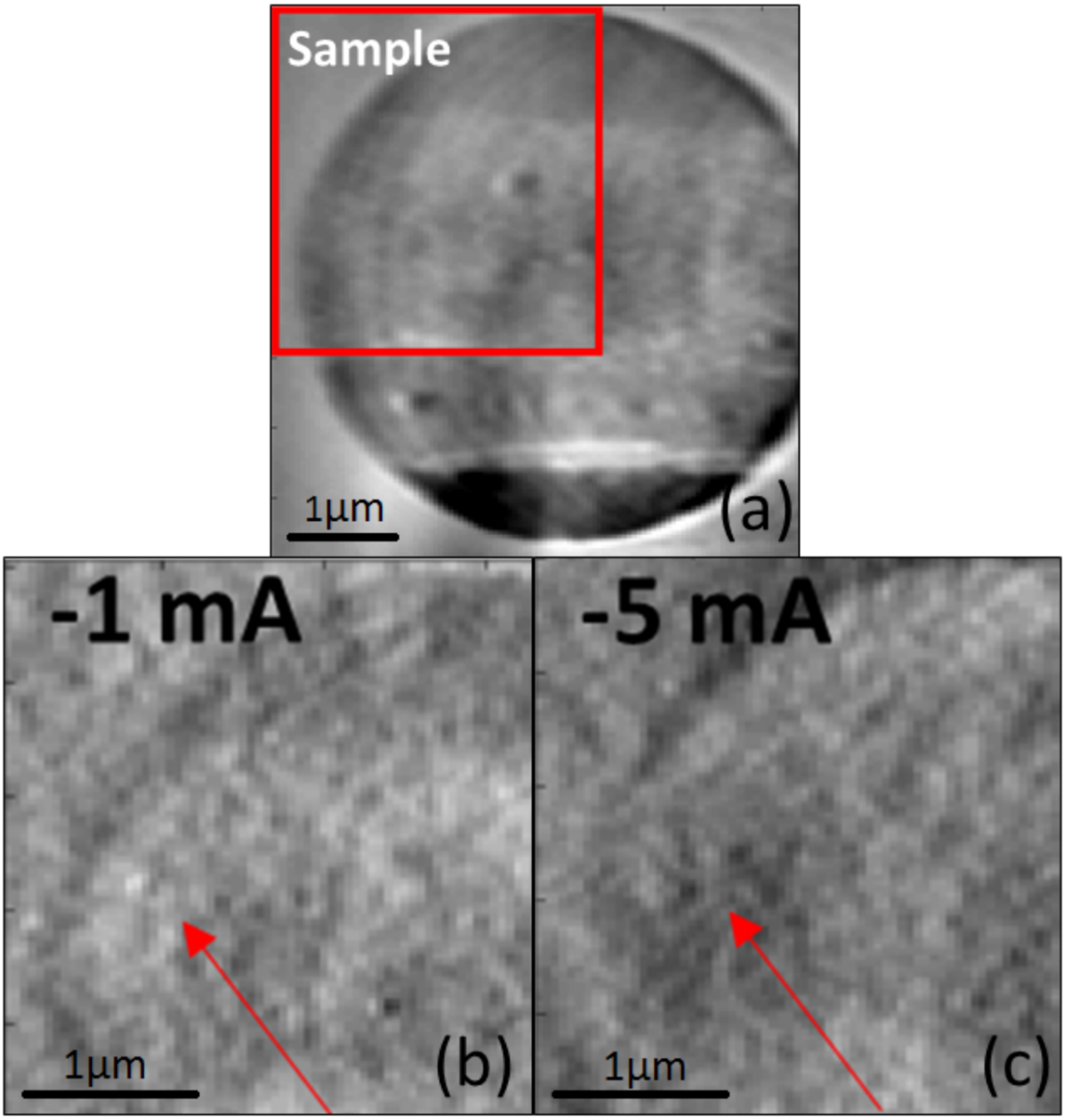

FIGURE 4.4: HERALDO reconstructions for a SL-STO device. (a) Aperture in the gold mask providing access to the underside of the stack (non-magnetic image). The red square encloses the region of the sample for which magnetic contrast is shown in (b) and (c). (b), (c) Magnetic images of a SL STO device at -1mA, and -5mA respectively. The red arrow shows where the NC (red circle) is positioned. Colormap: black and white correspond to a oposites direction of the in-plane magnetization.

a trajectory for the vortex. However, it is still possible to observe changes in the time-averaged magnetic contrast that occur at different current values. It is expected that at -1 mA the V-AV dynamics disappear due to the small current density. At -5mA the magnetization dynamics underneath the contact generate a low frequency microwave signal and some change in the magnetization is expected to occur. The comparison between these two current values is made in Figure 4.4 (b) and (c). While the appearance of two dark spots is suggestive of magnetic contrast associated with time-averaged vortex motion, it is impossible to completely rule out the breakthrough of structural features into the magnetic images. Further testing of the reconstruction process on model systems is required to confirm this latter interpretation.

4.3 Conclusion

In conclusion, we have presented time-averaged images of the magnetization within single layer NC STO devices with 100 nm and 50 nm nano-contact diameter. Transport measurements showed a response characteristic of the vortex – antivortex dynamics that have been previously reported [155], making the devices good candidates for imaging by x-ray holography techniques. HERALDO measurements suggest pinning of a vortex at the rim of the aperture within the Au mask for a device with 100nm NC diameter at DC current values of -24mA and 24mA. For smaller current values, devices with a 50nm NC diameter showed changes in the time averaged magnetic contrast that may indicate the presence of a dynamic process within vicinity of the NC. Since the x-ray beam has a well-defined time structure, time resolved stroboscopic measurements should be possible in future by injection locking to a multiple of the synchrotron master oscillator frequency.

Chapter 5

Dissipative Magnetic Solitons

5.1 Introduction

As discussed in Chapter 2, section 2.6.2, the NC-STO containing magnetic layers of orthogonal magnetization provides an ideal environment in which to nucleate a dissipative magnetic soliton refered to as droplet from here on. A droplet is a localized excitation sustained by STT, with magnetisation opposite to the rest of the free layer, for which the amplitude of precession decays exponentially towards its boundaries[76]. Similar to theoretically predicted conservative solitons[77], magnetic droplets can be sustained by balancing exchange and anisotropy energies and through the opposing effects of the damping and STT. In 2013, an experimental study led by J. Åkerman [75] showed that a magnetic droplet can be created and maintained within a NC-STO. Further investigations based on transport measurements and micro-magnetic simulations of these systems [78–87] revealed a rich dynamic structure, promising a range of applications in microwave technology. However, few experimental techniques allow the magnetisation of these structures to be imaged with adequate resolution ($\leq$ 32 nm) [26, 134] while the necessary external magnetic field is applied. Therefore only a few direct images have been obtained [156–158] of magnetic solitons confined with NC-STO devices, so that the different dynamic regimes of the system remain largely unexplored. In the present chapter we report one of the first direct measurements of the magnetic structures within the FL of an orthogonal NC-STO for different combinations of external magnetic field and applied DC current. In order to obtain magnetic information from the sample we combined holography with extended reference autocorrelation by linear differential operator (HERALDO) with the magnetic contrast provided by X-ray magnetic circular dichroism (XMCD) (both topics revised in chapter 3, section 3.1) . The latter, being element-specific, allows different layers to be probed separately. Our implementation of magnetic HERALDO allows us to access both the perpendicular and parallel components of the magnetization [2, 26, 134, 153]. Here we work in the perpendicular x-ray incidence geometry, which provides the perpendicular component of magnetization [153]. A particular advantage in this case is also that the magnetisation can be imaged beneath the electrical contacts. Studies of the magnetisation, both around and underneath the nano-contact, are crucial for understanding the importance of the Oersted field in the nucleation and subsequent drift of the droplets. In this study the sample fabrication process does not allow the exact location of the NC to be known, however as we show below, the area of the NC can be identified by the unique structure of the domains nucleated by the Oersted field arising from the DC current. Imaging the magnetic structure at different values of the magnetic field and electric current shows a significant variation in the domain structure around the NC. We demonstrate that at certain conditions, correlated with the intensity spectra observed in transport measurements, a localised magnetic structure with opposite polarisation to surrounding magnetisation can be observed. We suggest that this visualisation is in direct agreement with magnetic droplet formation at the field and current values expected from electrical measurements.

5.2 Experimental method

5.2.1 Sample fabrication

50×250 μm^2 rectangular patterns were exposed and developed on standard 4-inch thermally oxidized Si wafers using an optical lithography technique. A pseudo-spin-valve structure of composition Co (6 nm)/Cu (6 nm)/Co (0.2 nm)[Ni (0.8 nm)/Co (0.3 nm)]$\times$4, was then deposited by confocal magnetron sputtering onto a Ta (4 nm)/Cu (11 nm)/Ta (4 nm) seed layer and capped with a Cu (2 nm)/Pd (2 nm) bilayer. The lift-off process was completed by the removal of the remaining photo resist, and followed by the deposition of a 30 nm-thick SiO_2 dielectric film by chemical vapour deposition. Nano-pores of different size were formed within the SiO_2 using electron beam lithography and highly selective reactive ion etching. The device fabrication was completed by the deposition of a 400 nm Cu/100 nm Au top electrode using a combination of lift-off lithography and sputtering. All the device fabrication was performed by J. Åkermans group in KTH Royal Institute of Technology in Stockholm, Sweden.

5.2.2 Device Characterization

In order to electrically characterize the NC-STO, the sample was mounted in a custom probe station and a DC bias current from a Keithley 6221 current source was passed through the NC and between the signal and ground lines of the surrounding coplanar waveguide (CPW) structure. The current was swept from 0 to -40 mA under a fixed external field of $\sim$ 0.3 T at room temperature. In order to decouple and amplify the a.c. signal from the device, a bias-T and a 2 - 18 GHz AtlanTec(AS7265) amplifier were used respectively . The amplified a.c signal was recorded by an Agilent E448A spectrum analyser.

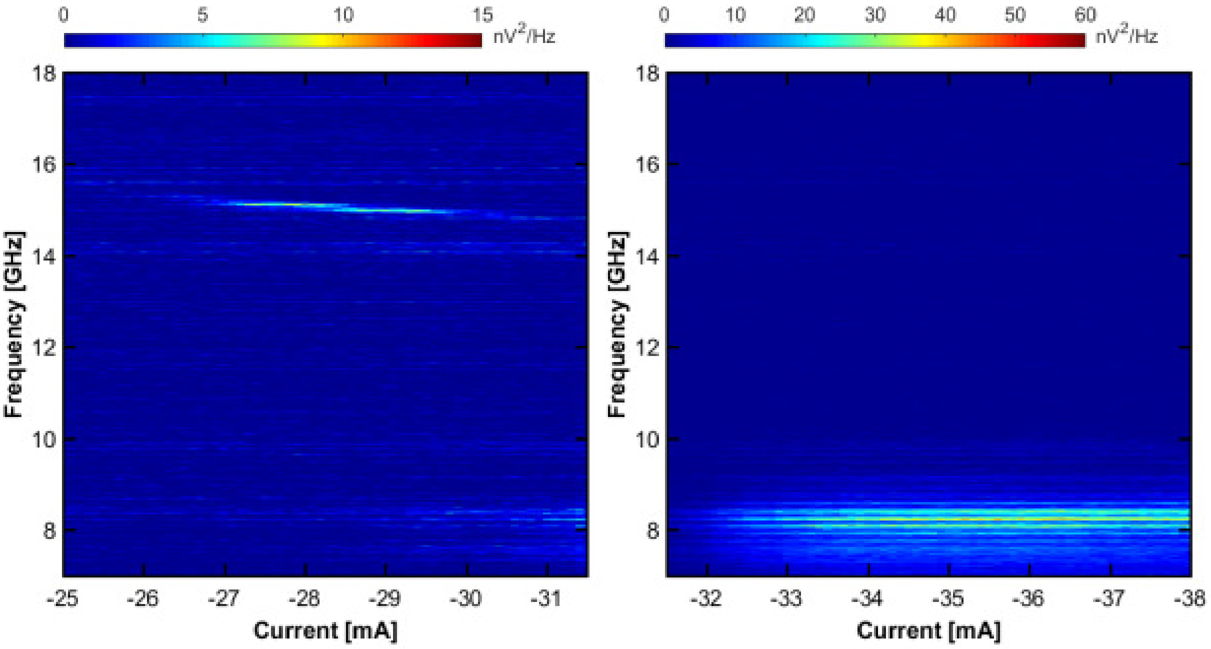

FIGURE 5.1: Power spectral density (PSD) is represented by the colour scale for an orthogonal pseudo spin-valve with a nano-contact of 90 nm diameter with a magnetic field of 0.4 T applied perpendicular to the sample plane. When the threshold current for the nucleation of the droplet is reached ($\sim$-30.5 mA), a sudden drop in in the emission frequency of $\sim$ 8 GHz occurs in addition to a dramatic increase of the emitted power, as is shown in (a) and (b).The additional structure is an artifact due to standing waves in one or more of the cables between the microwave components in the measurement chain.

5.2.3 HERALDO measurements.

The measurements presented in this paper were taken on beamlines I06 and I10 of the Diamond Light Source using a continuous filling pattern ($\sim$300 mA). To perform x-ray magnetic circular dichroism measurements on the samples, left and right-circularly polarised x-rays were applied with a photon energy of 851.1 eV coinciding with the Ni L_3 absorption edge. The interference pattern of the direct and diffracted x-rays for each polarisation was recorded on a CCD camera positioned behind a beam stop, that blocked the direct non-diffracted beam, at a distance of 60 cm from the sample, resulting in a minimum spatial resolution of 32 nm. To obtain holographic images the sample had a reference slit that was isolated from the imaged area by a distance of twice the aperture diameter but which remained within the x-ray transverse coherence length ($\sim$25 μm). Holograms recorded for left and right polarisations were subtracted and then processed using directional derivatives and Fourier transformed in order to obtain the real-space image.

5.3 Results

Electrical transport measurements and time-averaged imaging of the dynamics of the out-of-plane magnetisation within an orthogonal NC-STO were performed for samples with NC diameter of 90 nm and 110 nm for different combinations of applied magnetic field and DC injected current. Figure 5.2(a) and (b) shows the coplanar waveguide deposited on the top of the multilayer stack and used for transport measurements on these devices. Figure 5.2(c) and (d) shows a schematic of the multi-layered device on top of the S_3N_4 membrane and the intended position of the NC within the sample.

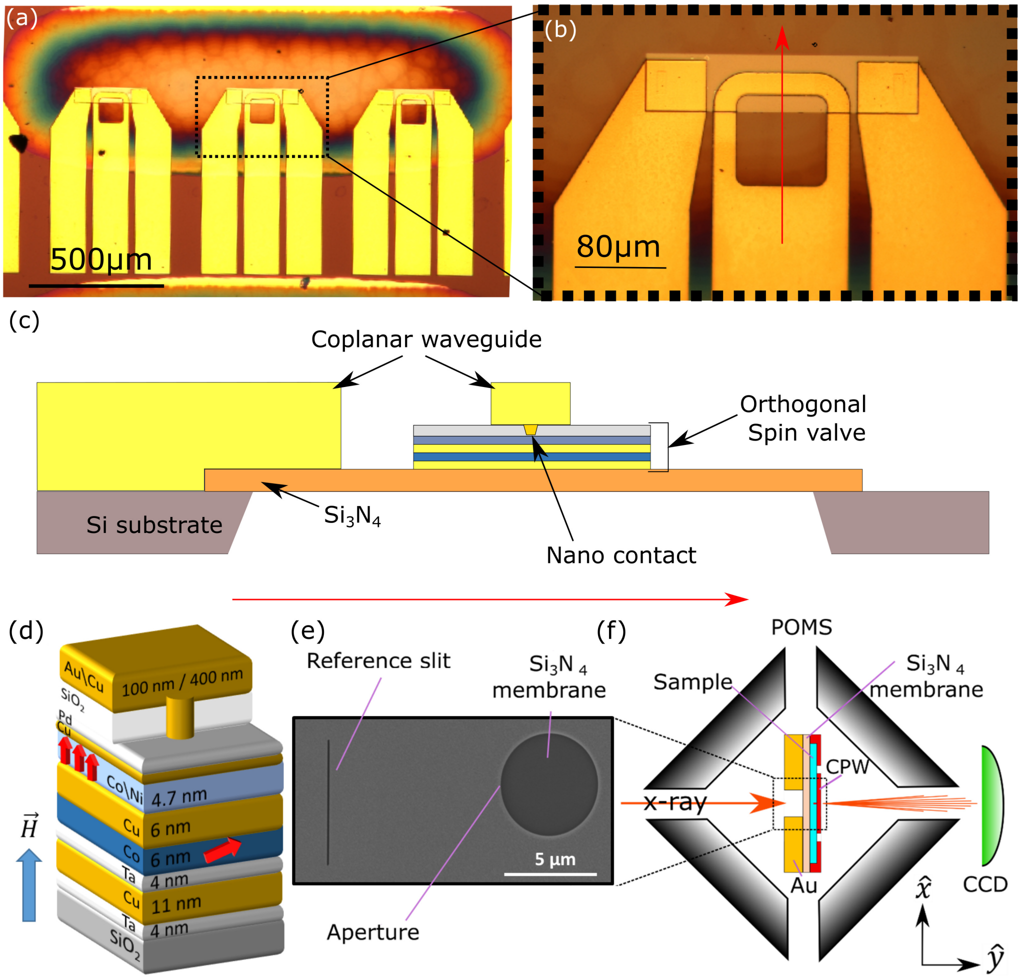

FIGURE 5.2: (a) Set of three coplanar waveguide used for HERALDO. The oval shaped region is the Si3N4 membrane. (b) Zoom of the top section a CPW shown in (a). The red arrow depict the position where the transversal cut shown in (c) is depicted. (c) Schematic of a transversal cut along the red arrow in (b) where the position of the nano contact is shown. (d) Schematic of a section of the 16×8 μm^2 mesa layer containing the nano-contact orthogonal pseudo spin-valve, where the Co/Ni multilayer acts as the free layer and the Co layer as the pinned layer. In this work devices with Cu nano-contacts of 90 and 110 nm diameter were studied. The red arrows indicate the equilibrium orientation of the magnetization of the magnetic layers after applying a magnetic field raging 20 -3000 mT out-of-plane (blue arrow). (e) Au layer covering one side of the Si_3N_4 membrane. An aperture of 5 μm diameter and a reference slit of 6 μm in length and $\sim$ 60 nm width were milled using a focused ion beam. The pseudo spin-valve is located on the opposite side of the Si_3N_4 membrane (f) Schematic set up for HERALDO measurements with an external magnetic field. The sample is positioned in the middle of a portable octupole magnet system (POMS) and the coherent x-rays from the synchrotron source pass through the aperture and the reference slit. The resulting diffraction pattern is captured by a CCD camera at a distance $\sim$ 60 cm behind the sample, at the end of the beam-line. The coplanar waveguide (CPW) supplies the DC current that passes through the magnetic layers and generates the STT required to form the droplet soliton.

5.3.1 Transport measurements

Figure 5.1 shows the power spectral density (PSD) with a ∼-0.4 T external magnetic field applied to a device with 90 nm nano-contact diameter. Microwave emission occurs at a frequency of 15 ± 0.1 GHz from -27 to -30.5 mA, which then drops to 8.2 GHz, as the emitted power increases by a factor of about 5. Furthermore, emission at a lower frequency of a few hundreds of MHz is also detected once the threshold current for the nucleation of the droplet is reached (not shown here). This is in agreement with previous results where the appearance of lower frequency (hundreds of MHz) dynamics, simultaneous drop in frequency and an increase in emitted power of the principal microwave mode occurred as a droplet was formed [81, 159]. Considering also the stability map presented in reference [81], the device with a 90 nm NC diameter is a good candidate for imaging current-induced magnetisation dynamics in a range of magnetic fields. The device with 110 nm NC diameter also revealed similar electrical features but the magnetic field needed to image a magnetic droplet lies outside of the range that could be achieved within the used experimental set-up, which was 0.35 T.

5.3.2 Holographic measurements

Figure5.2(e) shows a SEM image of a standard sample used in HERALDO measurements. In this case, the device is built on one side of a Si_3N_4 membrane while the other side of the membrane is covered by a Au layer of ∼ 600 nm thickness. A reference slit and an aperture are milled into the Au layer using a focused ion beam, which together generate the diffraction pattern produced by coherent x-rays passing through and captured by the CCD camera, as shown in the schematic of the set-up in Figure 5.2(f).

Zero external field and zero current applied

The magnetic domain configurations found within both samples at zero current are the characteristic maze-like domain pattern well described in the literature for samples with perpendicular magnetic anisotropy (PMA). Figure 5.3 shows four magnetic domain patterns corresponding to four different points on the hysteresis curve. It is evident how the balance between magnetic domains of opposite polarisation changes as the magnetic field is increased. Even though the total thickness of the Ni layer is only $\sim$ 3.2 nm, and imaged behind a 500 nm copper contact, the magnetic contrast is remarkably good. It is worth to notice that the magnetic contrast of smaller domains is more pronounced. Larger domains appear more 'grey-ish' and non-uniform. This effect is related to a limitation of the set-up, but does not undermine the conclusions drawn from the observations. Generally, due to the use of a beam-stop, which partially blocks some of the scattered light, some information is lost, specifically in the low-angle scattering, which would normally be associated with larger objects. Smaller scatterers, such as narrower magnetic domains, would lead to larger angle diffraction not affected by the beam-stop [160].

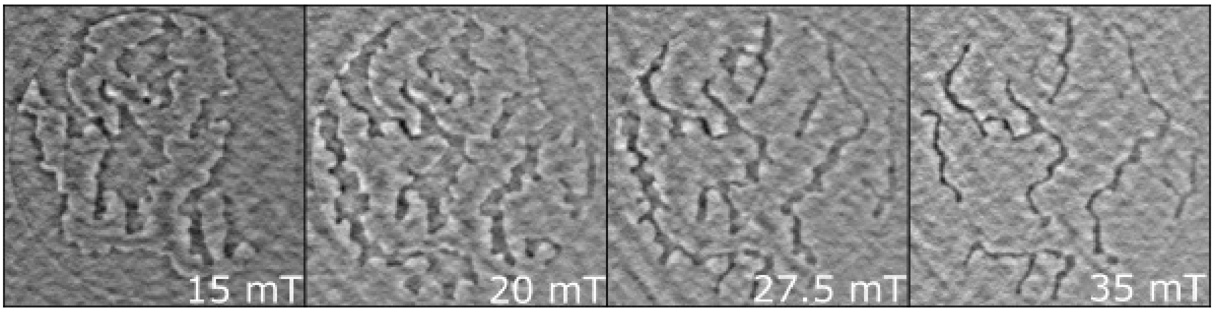

FIGURE 5.3: Magnetic domains formed on Ni within the free layer of the orthogonal pseudo spin-valve. The sample was saturated in the $-\hat{y}$ direction before an external magnetic field was applied in the $+\hat{y}$ direction (defined in inset of Figure5.2(c))with a magnitude of (a) 15 mT, (b) 20 mT, (c) 27.5 mT, and (d) 35 mT. The brighter (darker) regions correspond to magnetisation with a component in the $\hat{y}$ ($-\hat{y}$) direction. Bright regions overcome dark regions as expected as the magnetic field saturates the sample magnetisation in the $+\hat{y}$ direction.

Zero external field and current applied

An out-of-plane external field of 0.05 T was first applied to magnetically saturate the Co/Ni multilayer. DC currents ranging from -10 to -35 mA were then injected into the nano-contact at zero external magnetic field. It was observed that a single magnetic domain formed with magnetisation opposite to that of the rest of the sample. It is not possible to locate the exact position of the NC by optical or electronic means after the device is finished, but the location of the NC, and hence the maximum Oersted field generated by the current, is expected to be within the region where the reverse domains are nucleated. For the sample with 90 nm (110 nm) NC diameter this reverse domain first appears at -10 mA (-15 mA). Figure 5.4(a) shows how this domain grows in size as the amplitude of the DC current is increased. Due to the size of the magnetic domain formed, we suggest that its growth is driven by the Oersted field generated by the current passing through the NC. This field is large enough to locally modify the magnetisation as shown in Figure 5.4. This effect was also seen for positive current values. In contrast, the STT is not expected to contribute to domain formation outside of the NC region.

Low external field and current applied

Afterwards, to magnetically saturate the FL again, an out-of-plane field of 0.05 T was applied and then removed. A constant current of -33 mA was then applied to the sample with a 110 nm NC diameter at zero field. Small fields ranging from 20 to 50 mT were applied in the same out-of-plane direction to explore the interplay between the current and the external applied field. Under these conditions, a small C-shaped domain is observed at 20 mT that we infer to be nucleated from the NC. As the magnetic field was increased, the magnetic domain collapsed to a small region that was observed through all field steps. The same experiment performed instead with a current of -25 mA injected into the 110 nm contact (Fig. 5.4(b), bottom panel) showed a similar domain to that observed before at 25 mT and -33 mA, but in this case at 20 mT. This reverse domain vanished when the magnetic field was increased to 30 mT, such that the sample appeared to be in a state of uniform magnetic saturation (Figure 5.4(b), bottom panel for 40 and 50 mT).

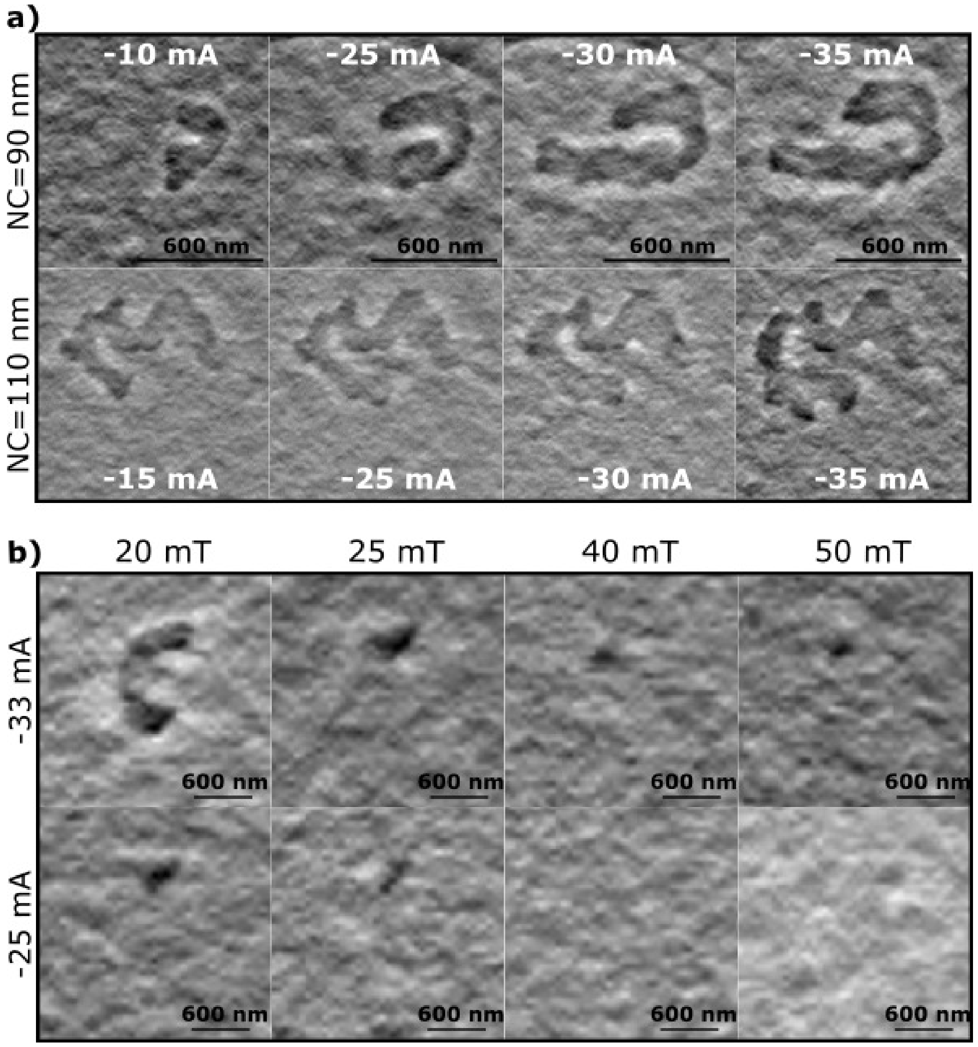

FIGURE 5.4: Magnetic structures observed for different fields and applied current values. The samples were saturated by an out-of-plane field of 0.05 T that was then reduced to zero. (a) The darker regions are the magnetic domains created by passing a DC current of -10, -15, -25, -30 and -35 mA through NCs of 90 (upper panel) and 110 nm diameter (lower panel) with zero external magnetic field. The nucleation of the domain is followed by small increments in its size as the amplitude of the DC current is increased. (b) The samples were magnetically saturated at 0.05 T and the field was then removed. The DC current injected through the 110 nm NC was fixed at values of -33 (upper panel) and -25 mA (lower panel) and HERALDO measurements were made with fields of 20, 25, 40 and 50 mT applied perpendicular to the sample plane in the direction of the initial saturation, parallel to the direction of the x-rays. The domain size decreases as the external magnetic field is increased, vanishing when the external magnetic field is sufficient to overcome the influence of the Oersted field produced by the current. Colormap: black and white correspond to a oposites direction of the out-of-plane magnetization.

Due to the available size and orientation of the magnetic field, all the former measurements were made on devices with a PL magnetized mostly in plane and a FL magnetically saturated out of plane. It was shown above that, for a NC of 110 nm diameter, the Oersted field generated by a current of -33 mA nucleated a reverse domain at zero field within a saturated sample, as shown in Figure 5.4. When an external field is applied, this effect is still visible but the size of the domain nucleated by the current is smaller than for the zero field case. As the external field is increased, it begins to dominate and the effect of the Oersted field is only seen at shorter distances from the nano-contact. The interplay between the external field and the Oersted field produced by the DC current modifies the local magnetic free energy, and therefore the reverse domain might still appear even for fields where the FL would otherwise be saturated, as can be seen in Figure 5.4(b).

Moderate external field and current applied

In order to work within the magnetic field range where transport measurements showed the nucleation of a droplet, an external field of -0.3 T was applied perpendicular to the plane of the sample with a 90 nm diameter NC. A localized reversal of the magnetisation was observed at -35 mA injected current at the location inferred for the NC (Figure 5.5 (b). This structure was not present in the images taken at smaller current values, while the value of -35 mA is in good agreement with that expected ($\sim$ -33 ma), from theory and transport measurements, for nucleation of a droplet in a 90 nm NC subject to a field of 0.3 T. In order to confirm the correlation between the structure observed and the nano-contact position, a yellow dashed line denoting the edge of a domain formed in the vicinity of the nano-contact at -10 mA without external field (Figure 5.5(a) is superimposed upon Figure 5.5(b). Figures 5.5(c)and (d) are a close-up of the region enclosed within the red square in Figure 5.5(b), where the black dashed line represents the possible position of a NC of 90 nm diameter.

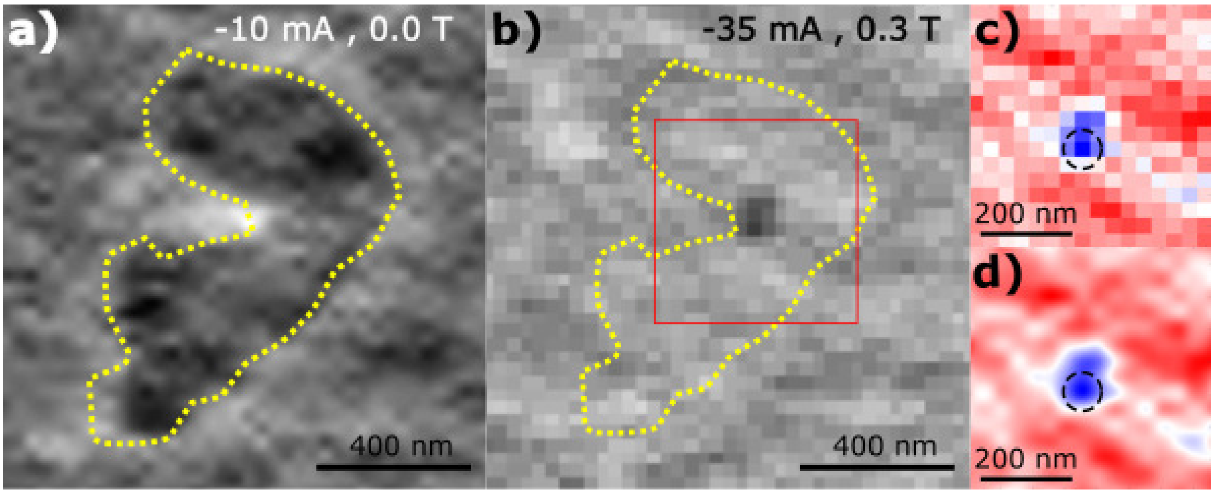

FIGURE 5.5: (a) Details of the magnetic contrast observed for the 90 nm NC sample for -10 mA injected current at zero external field shown in Figure 5.4(a),top left. The dashed line denotes the edge of the domain generated by the DC current. (b) The magnetic contrast obtained for -35 mA injected current and 0.3 T applied perpendicular to the sample is shown. The dashed line from (a) has been superimposed for comparison of the size and position of the magnetic features in (a) and (b). The black region in (b) is ascribed to a magnetic droplet soliton nucleated under the NC. The region enclosed by the red square in (b) is shown in (c) with a different colour scale, and in (d) after an interpolation and smoothing process. The black dashed line in (c) and (d) has 90 nm diameter and shows the suggested position of the NC within the sample. The centre of the NC was taken to be at the pixel with the greatest intensity. Colormap: black(blue) and white(red) correspond to a oposites direction of the in-plane magnetization.

We notice that the observed magnetic structure does not have the symmetrical circular shape expected of a droplet. It has been reported that canted magnetisation of the PL as well as the influence of the Oersted field [76, 83, 159] might affect the stability of the droplet so that it may extend beyond the region immediately beneath the NC or even drift away from it completely. It is possible that Figure 5.5(c) and (d) are showing the time averaged trajectory of the droplet as it deviates from the centre of the NC, but further measurements performed at different values of current and external field are needed to confirm this conjecture.

5.4 Conclusions.

The results shown in this paper are consistent with the local modification of the magnetisation around and beneath the NC due to the DC current. At zero field, and due to the size of the domains, we suggest that the modification of the magnetisation is due to the Oersted field produced by the DC current. When a small magnetic field is applied perpendicular to the sample plane, the interplay between the external field and the Oersted field modifies the size of the domains and erases them altogether when the external field becomes dominant, as can be seen in Figure 5.4. Finally, when the external field and the DC current are set to 0.3 T and -35 mA respectively, the magnetic contrast shows a magnetic structure with reversed magnetisation which we suggest is a droplet soliton. Since the exact position of the NC is unknown it is not possible to state unequivocally that the observed magnetic structure lies beneath the NC. However, the size of the structure, its position relative to the domains induced at other DC current values, and the correlation with separate electrical measurements, suggest that the nucleation of a droplet soliton has occurred.

Chapter 6

Spin Transfer Vortex Oscillators

6.1 Introduction

In chapter 2 we introduced the importance of STO and how multiple designs has been tested in order to improve two critical bottleneck issues for the realization of STO based devices: the phase stability and low power emission [161]. The implementation of NC on the top of the FL of a STO is a promising design due to its high tunability, high quality factor, and the ease by which it can be combined with conventional semiconductor technology.

When the magnetizations of the free and fixed layers lie in the plane of the film, the Oersted field produced by the DC current in the NC leads to the formation of a vortex in the FL, while the STT sustains vortex gyration. In this case the microwave emission of the NC-STO is driven by the gyrotropic motion of a vortex instead of magnetization precession. Vortex-based devices exhibit multi-octave frequency tunability and higher power output than precession based oscillators [61–63, 94]. However, the output power is still too low and the line width too broad for technological applications [35]. Phase-locked spin torque vortex oscillators (STVOs) formed from multiple NCs on a spin-valve mesa, are anticipated to exhibit enhanced microwave power and phase stability compared to single NC oscillators [65–67, 162, 163], providing a solution to the drawbacks of the NC-STO in the low frequency regime (100 MHZ to 1 GHz).

While the microwave emission due to the vortex gyration beneath the NC can be characterized by electrical measurements, the magnetization dynamics beyond the perimeter of the NC cannot. Knowledge of the spatio-temporal character of such dynamics is an essential prerequisite for successful mutual phase-locking of STVOs. In this chapter STVO devices with pairs of NCs of 100 nm diameter and center-to-center separation D = 200 to 1100 nm have been studied, by a combination of electrical measurements and time-resolved scanning Kerr microscopy (TRSKM)[164–167]. Microwave emission has been studied for the full range of D values, and the associated magnetization dynamics of the FL has been imaged with TRSKM for D = 200, 300 and 900 nm. It will be shown that vortices gyrate about the individual NCs for large D values and are visible outside the footprint of the top contact, while for small D values the dynamics are more tightly confined to the immediate vicinity of the NCs. Additional dynamic structures appear at the corners of the top contact that may result from the presence of anti-vortices.

6.2 Experimental Method

6.2.1 Sample details

All STVOs studied in the present work were formed on 16 × 8 μm spin valve mesas that were comprised of a Si/SiO$_2$ (thermally oxidized, 1 μm) substrate supporting a Pd(8)/Cu(15)/Co(8)/Cu(7)/Ni$_{81}$Fe$_{19}$(4.5)/Cu(3)/Pd(3) (thickness in nn) stack, as shown in Figure 6.1 (a). The Co, Cu(7), and Ni$_{81}$Fe$_{19}$ layers are the reference (RL), spacer (SL) and free layer (FL) respectively. A SiO$_2$(30) layer was deposited on top of the FL. Pairs of NCs of 100 nm nominal diameter and centre-to-centre separation D ranging from 200 to 1100 nm were then defined using electron-beam lithography, followed by reactive ion etching. Cu NCs were formed by the deposition of a Cu(1200)/Au(20) bilayer that also formed a coplanar wave guide that had a characteristic impedance of 50 Ω for microwave electrical contacts. A detailed explanation of the fabrication process can be found in the references [167].

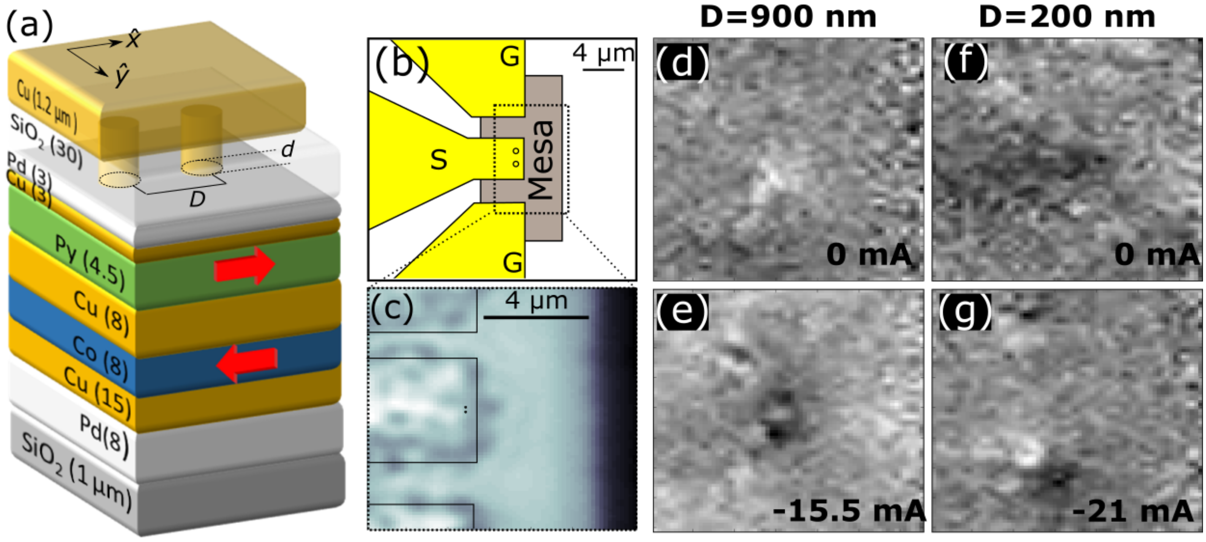

FIGURE 6.1: (a) Schematic of the spin valve mesa layer (thicknesses in nanometers) with NCs of diameter d and separation D. Co(8) and Py(4.5) are the reference and free layers respectively. The DC current is injected via a CPW and two NCs of 100 nm diameter. (b) CPW geometry with ground (G) and signal (S) electrical contacts. The circles close to the short edge of the signal contact show the estimated position of the NCs. (c) Reflectivity image of a typical device correspoding to the section enclosed in the dashed squared in (b). For a device with D =900nm, the change of the magnetization in the $\hat{\mathbf{x}}$ direction in the presence of a -10 dBm RF current is shown at (d) zero and (e) -15.5 mA DC current. Similarly, for D = 200 nm, the change in the magnetization in the $\hat{\mathbf{x}}$ direction is shown for I_{DC} = (f) 0 and (g) -21 mA. Colormap: black and white correspond to a oposites direction of the change of the in-plane magnetization in the $\hat{x}$ direcction.

6.2.2 Electrical Measurements

Electrical transport measurements were performed to probe the frequency of microwave emission stimulated by a DC electric current (I_{DC}). The current was supplied to the STVO via the CPW connected to a bias-tee that allowed the emitted microwave current to be separated from I_{DC} and directed into a spectrum analyser. To ensure that any initial non-uniform magnetic structure within the mesa was removed, an in-plane

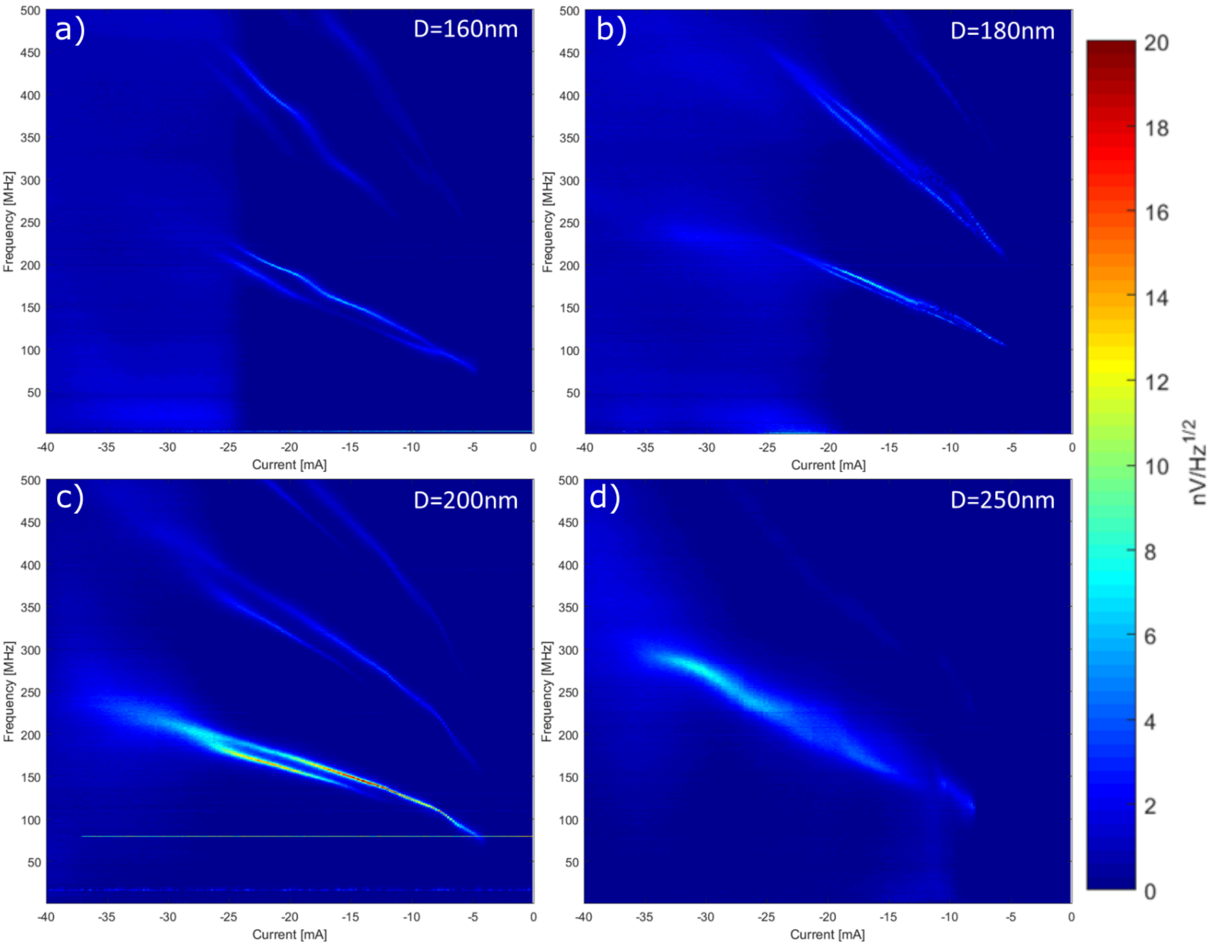

FIGURE 6.2: Voltage spectrum density of STVO with a pair of NCs separated by a) 160 nm, b) 180 nm, c) 200 nm and d) 250 nm

magnetic field of $\sim$ 20 mT was first applied parallel to the long edge of the mesa. The field was then reduced to a value of 0.3 mT before the current was applied. In order to phase lock the magnetisation dynamics of the STVOs for time-resolved measurements an additional microwave current (I_{RF}) was injected using a microwave synthesiser and a circulator. The amplitude of the I_{RF} current was typically 0.1 I_{DC}.

6.2.3 Time Resolved Scanning Kerr Microscopy

Time-resolved Kerr images were acquired using the laser pulses of a Ti:Sapphire oscillator generated with 100 fs duration, 80 MHz repetition rate,and 800 nm wavelength. The spatial resolution was previously determined to be $\sim$ 500 nm using the knife edge

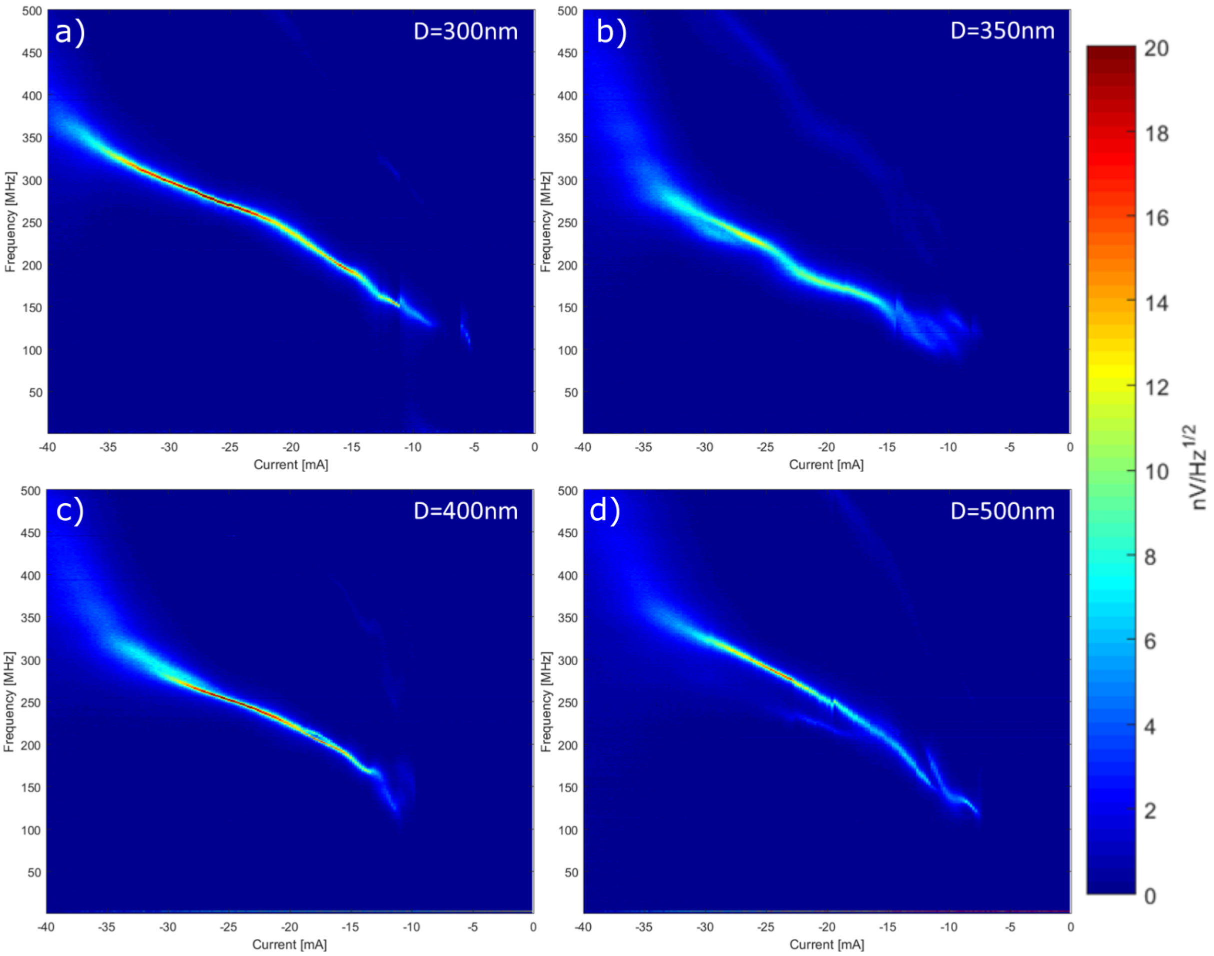

FIGURE 6.3: Voltage spectrum density of STVO with a pair of NCs separated by a) 300 nm, b) 350 nm, c) 400 nm and d) 500 nm

technique [168, 169]. In order to perform stroboscopic measurements, the laser and the microwave synthesizer used to inject I_{RF} to the STVO were phase-locked to an 80 MHz master clock. The frequency of I_{RF} was therefore required to be an integer multiple of 80 MHz. In the present work, the STVO was locked at a frequency of 160 MHz for time resolved measurements. The phase of I_{RF} was modulated through 180deg at ∼3 kHz so that the change in the magnetization could be recorded by lock-in detection. Each image was acquired at a fixed phase of the injected RF current, and the longitudinal and polar magneto-optical Kerr effect (MOKE) were used to recover the three spatial components of the dynamic magnetization simultaneously. All TRSKM measurements were performed with a 30 Oe bias field applied parallel to the x axis. A more detailed

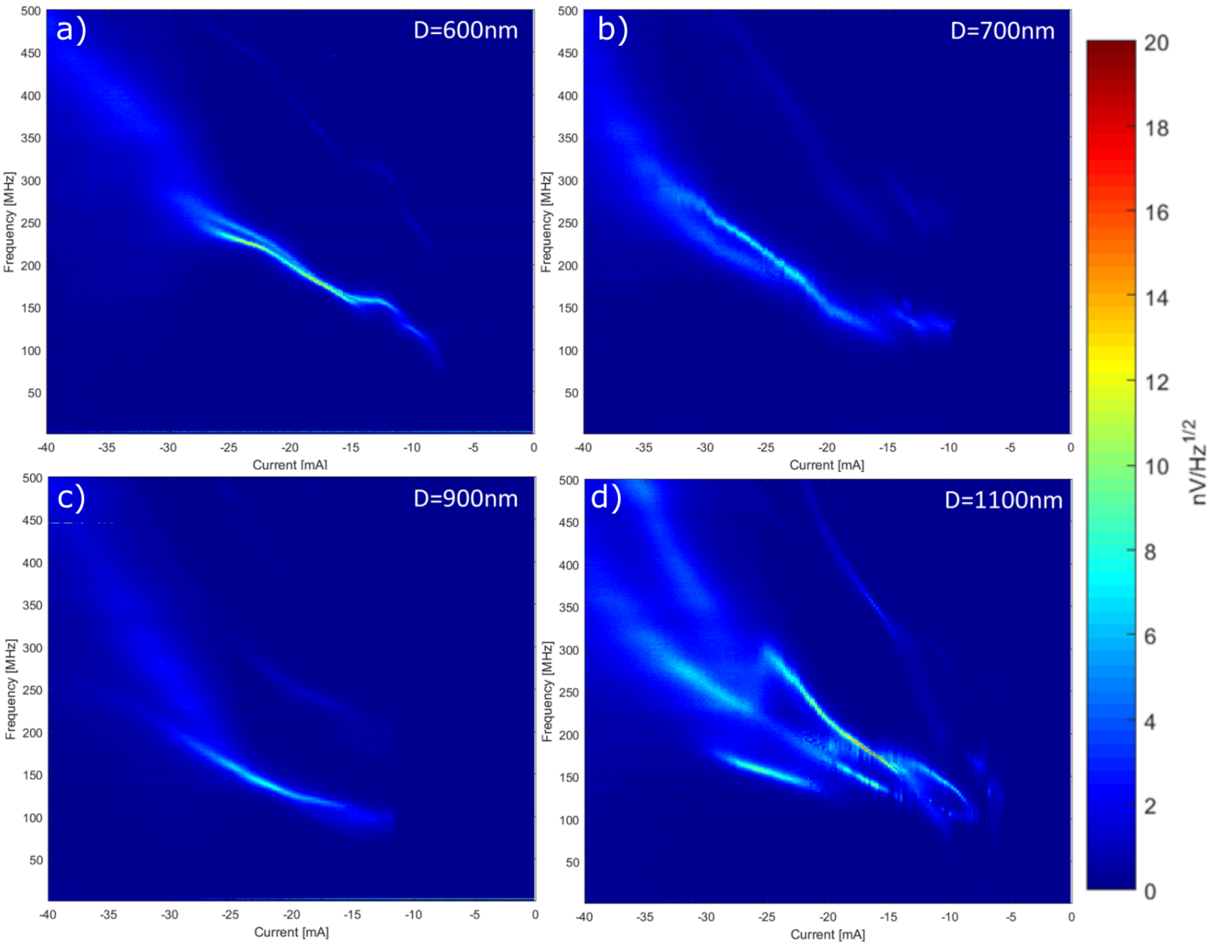

FIGURE 6.4: Voltage spectrum density of STVO with a pair of NCs separated by a) 600 nm, b) 700 nm, c) 900 nm and d) 1100 nm

explanation of the experimental technique has been provided previously [165–167].

6.3 Results

Electrical measurements were perfomed at remanent field (≤5 Oe) upon devices with values of D ranging from 160 to 1100 nm. The voltage density spectrum obtanied from these measurements are shown in Figures 6.2, 6.3, and 6.4. Figure 6.5 (a) shows the peak microwave emission (blue solid circles) and the current needed to observe such emission (red open circles) for different D values. The peak emission varies non-monotonically from 7.9 nV/$\sqrt{Hz}$ for D=160nm to 25.5 nV/$\sqrt{Hz}$ for D=300 nm. From these electrical measurements alone it is unclear why different current values of 15

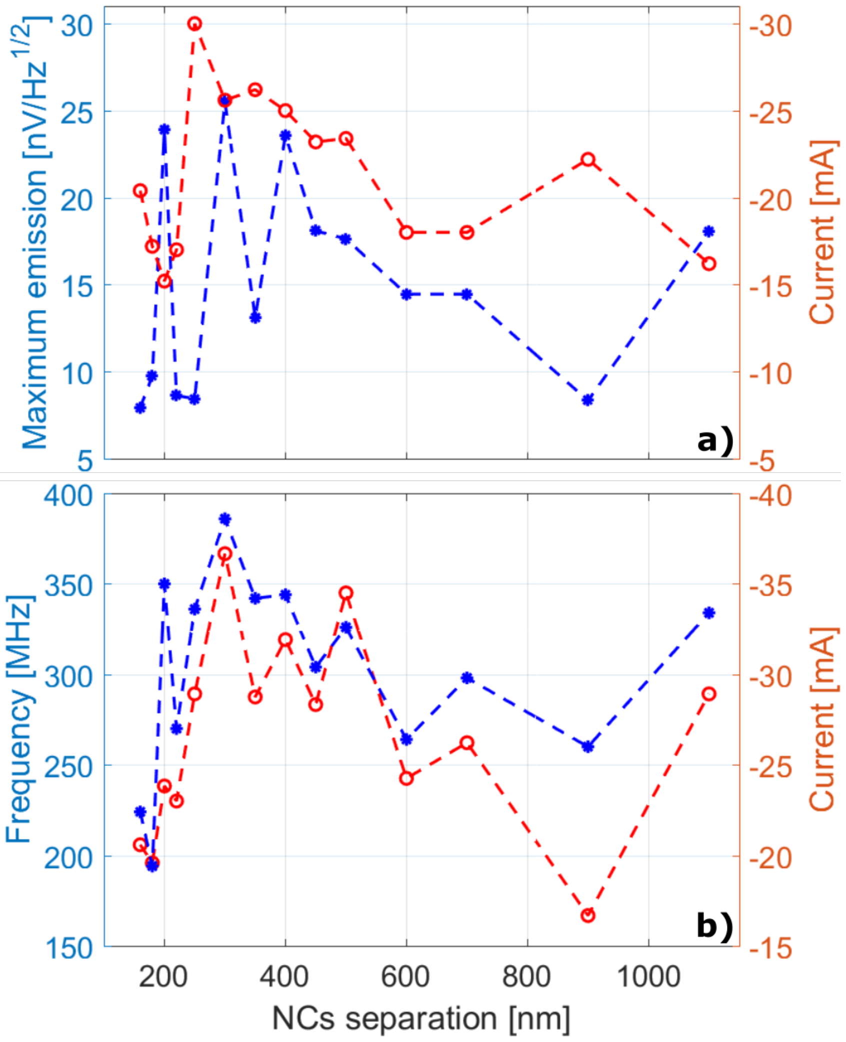

FIGURE 6.5: (a) Dependence of peak microwave emission (blue solid circles), and the current (open red circles) at which peak emission was observed, upon NC separation. (b) Frequency (blue solid circles) at which emission of greater than 5 nV/$\sqrt{Hz}$ was observed as I_{DC} was reduced from -40 to 0 mA, and the current (red open circles) value at which this occured.

mA and 25 mA are required to achieve emission with similar amplitude at D = 200 nm and D= 300 nm respectively. One speculative explanation could be that a single vortex gyrates about both NCs when D = 200 nm so that the magnetisation beneath each NC rotates in phase. In contrast, when D = 300 nm if a sepatate vortex is localised at NC, then a larger current maybe requred to phase-lock their dynamic response in the presence of their respective dynamic dipolar and exchange fields that may act to introduce a phase difference [168, 170]

Figure 6.5 (b) shows the frequency at which the amplitude of emission exceeds ($\geq$ 5 nV/$\sqrt{Hz}$) (blue solid circles) as I_{DC} is swept from -40 and 0 mA, and the value of the current (red open circles) at which this occurs. It is interesting to note that, in general, the non-monotonic variation of onset frequency follows that of the current at which the onset is observed. This is useful for applications since it shows the optimum device geometry for operation at the lowest current. For example when D = 200 nm it can be seen that the onset of auto-oscillation occurs at a relatively small current of ~24 mA compared to ~37 mA for D = 300 nm. At the same time Figure 6.5 (a) shows that the peak emission at D = 200 nm requires the minimum current. The larger current required at D = 300 nm may indicate an energetically unfavourable transition from small to large NC separations, that support single vortex and multiple vortices respectively.

From this initial screening, the devices chosen for TRSKM measurements were those with D = 200 and 300 nm, due to their large peak emission and higher frequency of operation, but quite different current requirements, and D = 900 nm on account of its small peak emission and lower frequency of operation, which may result from vortices gyrating on each NC with a significant phase difference. This choice of devices allows TRSKM to explore the suggestion that single and multiple vortices from at pairs of NCs with small and large values of D respectively.

Figure 6.6 (a) and (b) show the voltage spectral density (VSD) of the emission from devices with D = 200 and 900 nm respectively, with an external field of 0.3 mT applied parallel to the $\hat{x}$ axis. The value of I_{DC} was swept from the largest negative value to zero. For D = 200 nm, a single fundamental mode is observed for large negative I_{DC}, which splits at I_{DC} = -15.2 mA before disappearing at I_{DC} = -10.2 mA. The inset in Figure 6.6 (a) shows the VSD for the same device with zero external field, where a single broad mode splits into two modes at I_{DC} ~-25.5 mA. The lower frequency mode vanishes at I_{DC} ~ -15 mA while the higher frequency mode persists until I_{DC} ~ -3.8 mA. On the other hand, for D = 900 nm, again with 0.3 mT external field applied, two modes are observed that coexist between $I_{DC} \sim$ -24.5 mA and - 17.6 mA. Thereafter, only the higher frequency mode is observed until it disappears at $I_{DC} \sim$ -7.6mA. The inset in Figure 6.6 (b) shows the VSD of the same device for zero external field. In this case, two modes coexist until $I_{DC} \sim$ -7 mA, while the remaining mode vanishes at -5 mA.

The changes in mode frequency observed as $|I_{DC}|$ is decreased are associated with a change in the trajectory of vortex precession, which results from a reduction of the Oersted field that in turn modifies the equilibrium magnetization within the vicinty of the NC [154]. In a similar way, the mode character also depends upon the value of the external field [166]. It is interesting to note that, when an external field is applied, for I_{DC} = -21 mA and D = 200 nm, the two modes observed at zero field turn into a single mode with lower frequency, higher amplitude, and smaller linewidth, as can be seen in Figure 6.6.(e). This is consistent with the formation of a single vortex that gyrates about both NCs [171].

However, for a device with D =900 nm and I_{DC} = -12.9 mA, there are again two modes at zero field that turn into a single mode when the field is applied. At remanence the emission hops between single and multi-mode states when the magnitude of the current is reduced from approximately 16 mA to 8 mA. This suggests that, either the lower frequency mode corresponds to two vortices oscillating with a substantial and variable phase difference, such that when they oscillate out of phase, the emission vanishes, or that the system is hopping between a single and multi-vortex state [171]. However, it is not possible to determine the dynamic magnetization configuration of the sample from the electrical measurements alone.

Figure 6.1 (d), (e), (f) and (g) show the x component of the change in magnetisation observed in TRSKM measurements for devices with D = 200 and 900 nm. The x component has been chosen because it is easier to identify the main features of the dynamics. There are clear differences between the images acquired for finite (Figure 6.1 (d) and (f)) and zero (Figure 6.1 (e) and (g)) I_{DC} values. In both cases the value of I_{DC} has been

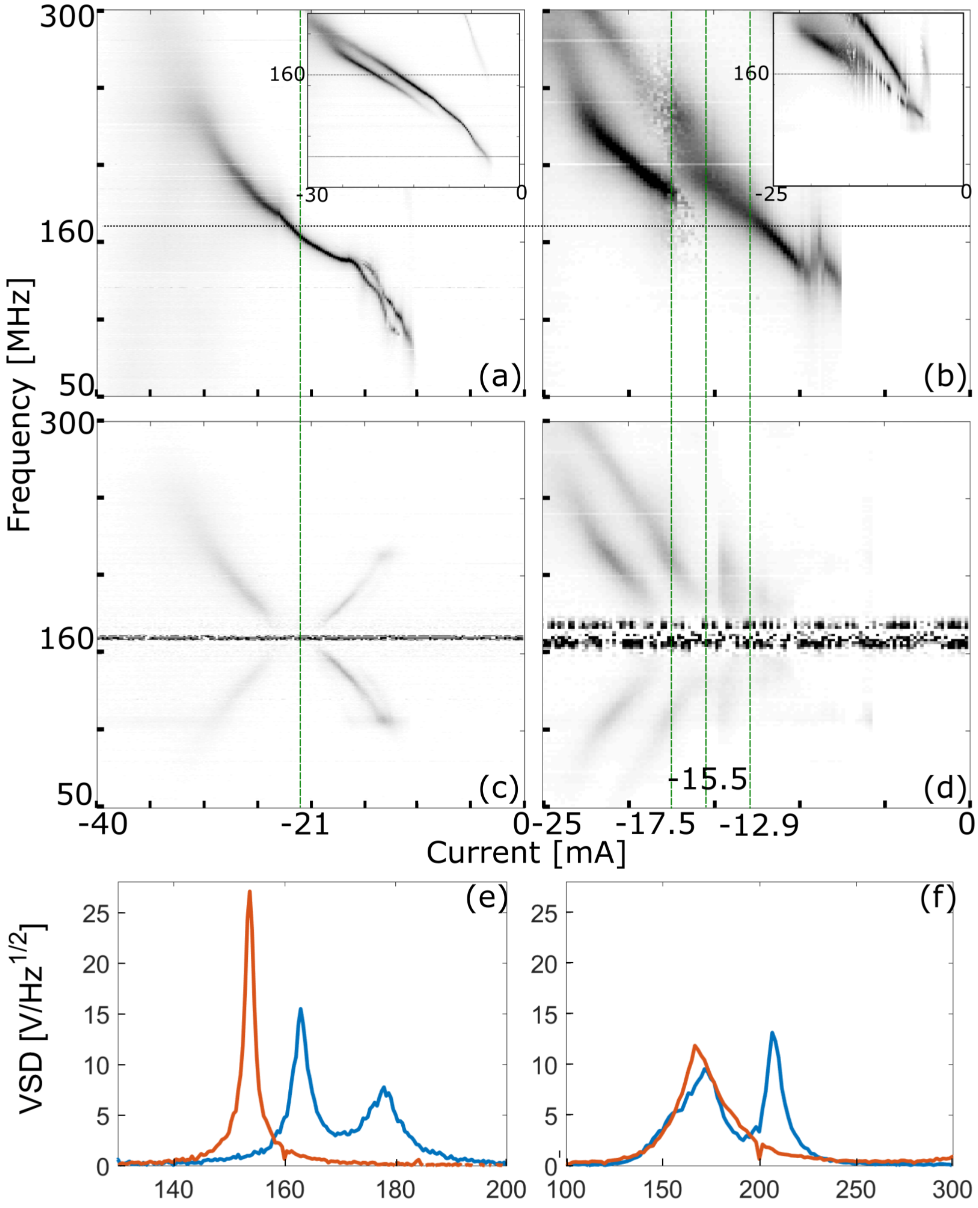

FIGURE 6.6: Voltage spectrum density (VSD) of the emission from devices with D = (a) 200nm and (b) 900nm, with an external magnetic field of $\sim$30 Oe applied parallel to the x axis. The inset figures show similar measurements made in zero external field. VSD of emission from devices with D = (c) 200nm and (d) 900nm when the vortex gyration frequency is injection-locked at 160MHz. The green dashed lines indicate the current values for which TRSKM images were acquired. Frequency dependence of VSD at (e) I_{DC} = -21 mA for D=200 nm, and (f) I_{DC} = -12.9 mA for D=900 nm, for I_{RF} = 0, and zero applied field (blue curve), and 30 Oe applied parallel to the x axis (red curve).

chosen to yield emission at 160 MHz. The images confirm that the dynamics observed in Figure 6.1 (e) and (g) are in response to STT delivered by I_{DC} and not excited by the I_{RF} Oe-field alone, as confirmed in [166]

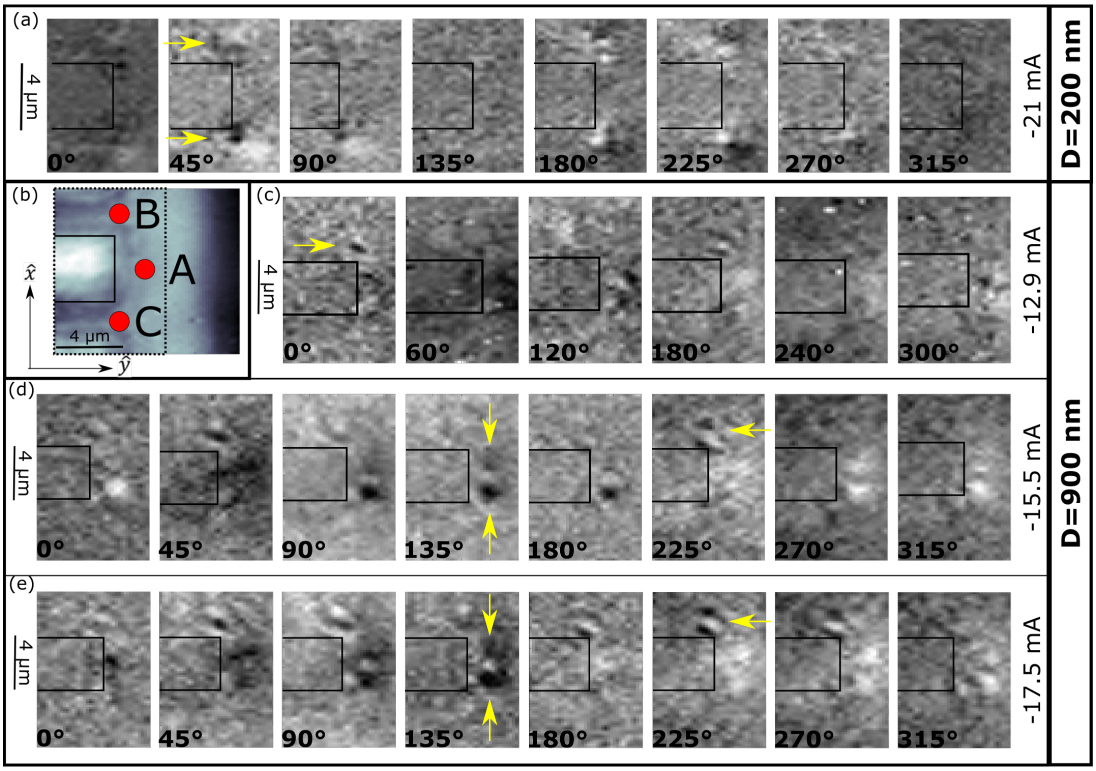

FIGURE 6.7: (a) TRSKM images acquired for different values of the phase of I_{RF}, with I_{DC} = -21 mA and a 30 Oe bias field applied parallel to the x axis, for a device with D = 200 nm. (b) Full reflectivity image of a typical device, where the dashed line shows the region studied in TRSKM measurements, and the red dots show regions of specific interest, with A being the region close to the NCs and B and C being close to the corners of the top contact. Similar measurements to those made in (a) were made upon a device with D = 900 nm for I_{DC} values of (c) -12.9 mA, (d)-15.5 mA, and (e) -17.5 mA. All images show the change of the x component of magnetization when the STVO is injection-locked at a frequency of 160 MHz. The gray scale represents the output voltage of the optical bridge detector. Each pixel in each image was normalized to its corresponding pixel in the reflectivity image for each phase. The reflectivity image was first normalized to a region in the mesa layer far away from the top signal contact. Yellow arrows point to spatial position of a significant change in contrast associated with magnetic structures such as vortices on anti-vortices. Colormap: black and white correspond to a oposites direction of the change of the in-plane magnetization in $\hat{x}$ direcction.

Figure 6.7 (a) shows TRSKM images obtained from the device with D = 200 nm and with I_{DC} = -21 mA. Two regions of strong contrast may be seen close to the corners of the signal contact of the CPW (regions B and C in Fig.6.7 (b)). The position of these regions suggest that they are related to the formation and subsequent drifting and pinning of anti-vortices created during nucleation of vortices at the nanocontacts. The electrical measurements shown in Figure 6.6 imply that, when the DC current is applied with zero external magnetic field, two magnetic vortices pairs are created within the vicinity of the NCs, each with its own characteristic frequency of gyration. However, when an external field of 0.3 mT is applied along the short edge of the top contact, the gyration of one vortex is favoured, while the other may be expelled and pinned in potential wells at the corners of the top contact. It is not possible to directly image the dynamics of the vortices when D = 200 nm because the dynamics are strongly localized and the dynamic magnetization does not extend as far as the edge of the top contact. While there is a small change in contrast in the middle of the short edge of the top contact, the spatial resolution is insufficient to characterize the motion. The observed change in electrical behaviour with the applied magnetic field is most likely due to one vortex remaining near the NC, perhaps with the trajectory of its core enclosing both NCs. This would yield the observed decrease in the observed frequency of gyration and the presence of only a single emission line.

For the device with D = 900 nm, there are three current values of interest when the microwave emission is locked at 160 MHz as shown in Figure 6.6 (d). For I_{DC} = -12.9 mA (Fig.6.7 (c)), the dynamics outside the short edge of the top contact (region A in Fig.6.7 (b)) are weak and inhomogeneous and not indicative of stable vortex gyration observed previously[166]. There is also a subtle change in contrast at the top corner of the top contact (Fig.6.7 (c) at 0 deg, see arrow). The amplitude of the Kerr signal of this region increases as I_{DC} is increased from -12.9 mA to -15.5 mA(Fig.6.7 (d)) and then to -17.5 mA (Fig.6.7 (e)), while along the short edge of the top contact pad localised dynamics emerge outside the vicinity of the NC. For these latter I_{DC} values, the observed contrast is consistent with the formation of a vortex on each NC [166]. The similar intensity of the two regions of localised dynamics at -17.5 mA is consistent with the interpretation that the pair of vortices gyrate in phase. At -15.5 mA a difference in the size and intensity of these two regions indicate that the vortices oscillate with a phase difference. Note that this will not appear as an out-of-phase mode because both NCs are injection locked by the same RF current, which forces similar phase of the gyration. Instead, the presence of dynamic interaction between two oscillators in the presence of the same RF source will introduce a phase difference in a similar way to that observed in Ref [168].

At -17.5 mA the enhanced contrast of the localised dynamics is consistent with enhanced STT due to the larger value of I_{DC} [166]. The enhanced STT will lead to a larger radius of gyration. The contrast of the localized regions will also be enhanced when their area becomes comparable to, or larger than the optical spot size, so that the contrast is no longer suppressed by the spatial resolution, as may be the case at -12.9 mA.

It is expected that gyration of the vortices about the NCs is driven solely by the STT. However, the magnetic structures localized at the corners of the top contact are also observed to oscillate, even though no STT is expected to act upon this region. It was also observed that there is a difference in the phase of oscillation between the dynamics near to the NC and those at the corners of the top contact, as can be seen by comparing regions A and B in Figure 6.7 (c), (d), and (e). Previously it was determined that such a phase difference exists between dynamics driven by STT and those driven by the RF Oe-field [166]. Since the dynamic features at the corners of the contact pad are not observed when $I_{DC} = 0$, we conclude that they are either anti-vortices, or additional vortices formed within the free layer in the process of vortex formation by the DC Oe-field, which then oscillate due to the amplitude modulation of the RF Oe-field.

It is interesting to note the number of modes observed in electrical measurements and the number of the dynamic features far from the NC. When $D = 900$ nm it is clear from the Kerr images that dynamics associated with a vortex gyrating are observed close to each NC (Figure 6.7 (d) and (e), arrows at 135 deg). At the same time there is a single dynamic feature pinned at the top corner of the centre contact pad (Figure 6.7 (d) and (e), arrows at 225 deg). Previously we ascribed this feature to an anti-vortex in accordance with micromagnetic simulations [151]. On the other hand when D = 200 nm two dynamic features are observed at the top and bottom corners of the contact pad (Figure 6.7 (a) arrows at 45 deg). Since a single mode was observed in the electrical measurements, this suggests that one of the vortices has been expelled from the NC region and become trapped in the electrostatic pinning potential of the top contact pad. While the magnetic character of the dynamic features cannot be determined from Figure 6.7 (a) the presence of an additional feature in comparison to the the device with D = 900 nm supports the interpretation of an expelled vortex. This is of particular importance when considering the arrangement of vortices and anti-vortices in continuous films for dynamic coupling of more than two NCs, such as that described in Reference [65].

6.4 Summary

In summary, combined electrical and time resolved scanning Kerr microscopy measurements have been performed on double NC STVOs. Time resolved images acquired for devices with centre-to-centre NC separation of D = 200 and 900 nm have been presented. The electrical measurements are richly featured, often exhibiting multiple modes and their harmonics. The frequency, output power, and value of I_{DC} all showed non-monotonic variation as the NC separation was reduced. In addition the Kerr images acquired from the two selected devices showed spatial contrast of very different character. For D = 900 nm, localized regions of magnetization dynamics were observed close to each NC, with each region having similar spatial character to that found within single NC devices, suggesting that a separate vortex had formed at each NC[165, 166]. However, for a pair of NCs with 200 nm separation, no dynamics were observed in the region close to the NCs. At the same time, large amplitude dynamics were also observed at a distance of some microns from the NCs. In accordance with the number of modes observed in electrical measurements we speculate that these dynamics are due to the oscillation of anti-vortices that are pushed away from the NCs, pinned by stray DC electromagnetic fields from the top signal contact, and then excited by the stray RF Oersted field. The images suggest that the dynamics near to the NCs are linked to the dynamics at the corners of the top contact through dynamic dipolar interaction or indeed through interaction within the film for particular equilibrium states in the presence of I_{DC}. However, to advance understanding of these dynamics, further experiments and simulations are needed. An improved understanding of the interaction of pairs of NC-STVOs is crucial for the realization of networks of phase-locked STVOs that share common magnetic layers.

Chapter 7

Future work

Producing images of *things* that we cannot observe with our naked eye has been always a fascinating endeavour, even more when these *things* are hidden to our eyes as the magnetism of an object. The development of imaging techniques to observe the magnetisation of an object has made possible to confirm Weiss' prediction of the existence of magnetic domains in the early 1900, to imaging and control of the direction of single atoms in 2010 [172]. It is not difficult to note that the development of these high resolution techniques has been made within a time averaged regime. Despite the techniques and the difficulty of them, I believe that it is safe to say that working in this regime does not imply major challenges.

However, the interest within the scientific community has moved from the static to the dynamic regime. Nowadays the hot topics in magnetism are racetrack memories, magnetic structures dynamics such as skyrmions, vortices and magnetic bubbles, ultrafast demagnetisation processes, and magnonics among others. The dynamic processes occurring in these devices are in the order of 10 to 10^3 MHz (10^9 MHz in ultrafast demagnetisation). As it has been shown in this thesis, when the magnetisation dynamics behaves in a periodical manner, it is possible to lock that behaviour to the probe frequency to perform time resolved imaging via stroboscopic measurements. This is possible for a limited number of systems. The biggest challenge here is to extend time resolved measurements to non-periodical dynamics in a similar manner to that we used to record a common video. In order to do this we should increase the amount of photons per pulse to obtain a single frame per pulse. Although this can be done by using an x-ray laser (XFEL) facility, the focused beam instantly vaporises the sample and destroys the possibility to study the reproducibility of the processes within the same sample. In addition to the increment of the brillance of the source, we would need to increase the frequency of the probe. However, I believe that the most challenging step to overcome is the development of high sensitivity and fast acquisition time cameras for x-rays. The current fastest camera in the world can capture 10^{12} frames per second [173]. Although the technique is compatible with most light-matter interactions, it has been tested just for laser based experiments.

If we are able to overcome the challenges previously mentioned, it would be interesting to perform time resolved measurements on the nucleation and dynamics on the magnetic droplets devices presented in this thesis in order to understand the spatial stability of the droplet within different external applied fields. Without any external locking, the nucleation of the droplet is a non-periodical ultra fast event. In any case, it would be interesting to try injection locking in these devices and perform stroboscopic measurements. Understanding the stability, drift and survival time outside the DC excitation area is key for the design of spintronic circuits and microwave oscillators. Another interesting challenge is to observe the magnetisation dynamics under the NCs using TRSKM, that is by using a transparent device substrate, such as a Si_3N_4 membrane, instead of Si/SiO_2. However, in order to probe the free layer magnetisation, the magnetic layer order has to be reversed and the free layer would have to be closer to the substrate. While it is yet unknown what kind of effect these modifications would have upon the formation of the vortices underneath the NC area, it is an interesting experiment that might allow TRSKM to study a whole new range of NC based devices.

Finally, one of the most interesting challenges that I have faced during my studies was not related to the image processing of the magnetic dynamics but to the electrical measurement and frequency of those dynamics. The devices studied in this thesis work in the GHz regime and even the fastest ferromagnet based STT devices do not go over 100 GHz. It has been predicted by A. Slavin that using antiferromagnet based devices will allow us to achieve THz frequencies. The GMR effect that produces the voltage changes (and therefore the microwave emission) in ferromagnet based devices occurs between two different magnetic layers while the THz dynamics in antiferromagnets occurs between two different atomic layers. Therefore, the average GMR effect in an antiferromagnet based device is zero. It has been predicted that breaking the symmetry between the antiferromagnetic atomic layers will produce an effective change in voltage, hence an effective THz emission. Overcoming this challenge is a task for material scientists and it will be a huge step towards using this technology in neuromorphic computing, simulating synopsis-like pulses and pushing the boundaries of the current computational paradigm to non-linear processing and brain-like systems.

Chapter 8

Publication and conferences

8.1 Publications

- **E. Burgos-Parra**, N. Bukin, S. Sani , A. I. Figueroa, G. Beutier, M. Dupraz, S. Chung, P. Dürrenfeld, Q. Tuan Le, S. M. Mohseni, A. Houshang, S. A. Cavill, R. J. Hicken, J. Åkerman, G. van der Laan, and F. Y. Ogrin. “Investigation of magnetic droplet solitons using x-ray holography with extended references.” *Scientific Reports* **8**, 11533 (2018)

- Bukin N, **Burgos-Parra E. O.**, McKeever C. J., Keatley P. S., Hicken R. J., Kruglyak V. V., Fripp K., Beutier G., Jaouen N., Popescu H. “Time-resolved imaging investigation of the domain walls dynamics in Landau domain pattern” 2017 IEEE International Magnetics Conference, INTERMAG 2017.

- N. Bukin, C. McKeever, **E. Burgos-Parra**, P. Keatley, R. Hicken, F. Ogrin, G. Beutier, M. Dupraz, H. Popescu, N. Jaouen, F. Yakhou-Harris, S. Cavill, and G. van der Laan, "Time-resolved imaging of magnetic vortex dynamics using holography with extended reference autocorrelation by linear differential operator." *Scientific Reports* **6**, 36307 (2016)

- R. A. J. Valkass, T. M. Spicer, **E. Burgos Parra**, R. J. Hicken, M. A. Bashir, Mark

A. Gubbins, P. J. Czoschke and R. Lopusnik, "Time-resolved scanning Kerr microscopy of flux beam formation in hard disk write heads", *J. Appl. Phys.* **119**, 233903 (2016)

- **E. O. Burgos Parra**; N. Bukin, M. Dupraz, G. Beutier, S. Sani, H. Pepescu, S. Cavill, J. Akerman, N. Jaouen, P. Keatley, R. J. Hicken, G. van der Laan, "Holographic imaging of magnetization in a single layer nano-contact spin transfer oscillator, *IEEE Trans. Magn.* PP, 99, (02/2016).

8.2 Conferences

———- Fourth Year (2017 - 2018) ———-

- International Conference on Magnetism - San Francisco, United States of America. July. 15th and 20th, 2018 (talk)
- Emerging Applications of Spin Transfer Torque - Exeter, UK. June. 28th and 29th, 2018 (talk)
- International Conference on Microwave Magnetics - Exeter, UK. June. 24th and 27th, 2018 (poster)
- Magnetism 2018 - Manchester, UK. Apr. 9th and 10th, 2018 (poster)

———- Third Year (2016 - 2017) ———-

- Magnetism 2017 - York, UK. Apr. 3rd and 4th, 2017 (talk)
- MMM 2016 - New Orleans, USA. Oct. 31th - Nov. 7th, 2016 (talk)

———- Second Year (2015 - 2016) ———-

- Joint European Magnetism Symposia 2016 - Glasgow ,UK. . Aug. 21th - 26th, 2016 (poster)
- International School on Magnonics, Exeter , UK. Jun. 19th and 24st, 2016 (poster)
- Magnetism 2016 - Sheffield, UK. Apr. 4th and 5st, 2016 (talk)
- 13th Joint conference MMM-Intermag - San Diego, United States of America. Jan 11th to Jan 15th, 2016 (talk)

———-First year (2014 - 2015)———-

- 22nd Latin American Symposium of Solid State Physics (SLAFES) - Puerto Varas, Chile. Nov. 30th to Dec. 4th, 2015 (talk)
- Optical Polarisation Conversion in the Near Field workshop - Exeter, Uk. Jun. 25th and 26th, 2015 . (poster)
- Magnetism 2015 - Leeds, UK. Mar. 30th and 31st, 2015 (co author poster

———-Invited talks———-

- -Nanostructures schools 2018 - Viña del mar, Chile. Jan. 7th'10th , 2018
- -University of Salamanca - Salamanca, España. Jul. 22th , 2016 (45 min)
- -Weekly Colloquiom at Deparment of Physics, University of Chile - Santiago, Chile. Jan. 6th , 2015 (45 min)
- -Center of Development of Nanoscience and Nanotechnology (CEDENNA), Deparment of Physics, University of Santiago. Dec 18th, 2015. (45 min)

- -Magnetism group (Alvaro Nuñez), Deparment of Physics, University of Chile. Dec , 2015.(45 min)

Bibliography

[1] J. C. Slonczewski. "Conductance and exchange coupling of two ferromagnets separated by a tunneling barrier". In: *Phys. Rev. B* 39 (10 1989), pp. 6995–7002. DOI: `10.1103/PhysRevB.39.6995`. URL: `https://link.aps.org/doi/10.1103/PhysRevB.39.6995`.

[2] Erick O. Burgos Parra et al. "Holographic Magnetic Imaging of Single-Layer Nanocontact Spin-Transfer Oscillators". In: *IEEE Transactions on Magnetics* 52.7 (2016), pp. 3–6. ISSN: 00189464. DOI: `10.1109/TMAG.2016.2528959`.

[3] E. Burgos-Parra et al. "Investigation of magnetic droplet solitons using x-ray holography with extended references". In: *Scientific Reports* 8.1 (2018), p. 11533. ISSN: 2045-2322. DOI: `10.1038/s41598-018-29856-y`. URL: `https://doi.org/10.1038/s41598-018-29856-y`.

[4] Charles Kittel. "Physical Theory of Ferromagnetic Domains". In: *Rev. Mod. Phys.* 21 (4 Oct. 1949), pp. 541–583. DOI: `10.1103/RevModPhys.21.541`. URL: `https://link.aps.org/doi/10.1103/RevModPhys.21.541`.

[5] L Tauxe et al. *Essentials of Paleomagnetism*. 5th Web Edition, 2018.

[6] A. Mardana, Stephen Ducharme, and S. Adenwalla. "The sweep rate dependence of the electrical control of magnetic coercivity". In: *Journal of Applied Physics* 111.7 (2012), p. 07C708. DOI: `10.1063/1.3673829`. eprint: `https://doi.org/10.1063/1.3673829`. URL: `https://doi.org/10.1063/1.3673829`.

[7] G. Rasic and J. Schwartz. “Coercivity Reduction in Nickel Ferrite ($NiFe_2O_4$) Thin Films Through Surface Patterning”. In: *IEEE Magnetics Letters* 5 (2014), pp. 1–4. ISSN: 1949-307X. DOI: 10.1109/LMAG.2014.2302246.

[8] J. C. Denardin et al. “Magnetic Properties of Co/Cu/Py Antidot Films With Different Pore Diameters”. In: *IEEE Transactions on Magnetics* 50.11 (Nov. 2014), pp. 1–4. ISSN: 0018-9464. DOI: 10.1109/TMAG.2014.2331973.

[9] L. F. Bates. *Modern Magnetism*. Cambridge University Press, 1961. ISBN: 0521091624. URL: https://www.amazon.com/Modern-Magnetism-L-F-Bates/dp/0521091624?SubscriptionId=0JYN1NVW651KCA56C102&tag=techkie-20&linkCode=xm2&camp=2025&creative=165953&creativeASIN=0521091624.

[10] P. Weiss. “L’hypothèse du champ moléculaire et la propriété ferromagnétique”. In: *J. de Phys.* 6 (1907), pp. 661–690.

[11] A. Aharoni. *Introduction to the Theory of Ferromagnetism*. International Series of Monogr. Clarendon Press, 2000. ISBN: 9780198508090. URL: https://books.google.co.uk/books?id=Ru-z9b3WcfMC.

[12] G. T. Rado and H. Suhl. “Magnetism: Statistical Models, Magnetic Symmetry, Hyperfine Interactions, and Metals”. In: vol. 2B. Chapter "Direct exchange between well-separated atoms" by C. Henrring. New York: Academic Press Inc, 1965, pp. 1–181. ISBN: 0125753020.

[13] C. S. Wang, R. E. Prange, and V. Korenman. “Magnetism in iron and nickel”. In: *Phys. Rev. B* 25 (9 May 1982), pp. 5766–5777. DOI: 10.1103/PhysRevB.25.5766. URL: https://link.aps.org/doi/10.1103/PhysRevB.25.5766.

[14] I V Solovyev. “Combining DFT and many-body methods to understand correlated materials”. In: *Journal of Physics: Condensed Matter* 20.29 (2008), p. 293201. URL: http://stacks.iop.org/0953-8984/20/i=29/a=293201.

[15] J. Zak et al. “Fundamental magneto-optics”. In: *Journal of Applied Physics* 68.8 (1990), pp. 4203–4207. DOI: `10.1063/1.346209`. eprint: `https://doi.org/10.1063/1.346209`. URL: `https://doi.org/10.1063/1.346209`.

[16] T. J. Silva, S. Schultz, and Dieter Weller. “Scanning near-field optical microscope for the imaging of magnetic domains in optically opaque materials”. In: *Applied Physics Letters* 65.6 (1994), pp. 658–660. DOI: `10.1063/1.112261`. eprint: `https://doi.org/10.1063/1.112261`. URL: `https://doi.org/10.1063/1.112261`.

[17] M. R. Scheinfein et al. “Scanning electron microscopy with polarization analysis (SEMPA)”. In: *Review of Scientific Instruments* 61.10 (1990), pp. 2501–2527. DOI: `10.1063/1.1141908`. eprint: `https://doi.org/10.1063/1.1141908`. URL: `https://doi.org/10.1063/1.1141908`.

[18] C. Schönenberger and S. F. Alvarado. “Understanding magnetic force microscopy”. In: *Zeitschrift für Physik B Condensed Matter* 80.3 (Oct. 1990), pp. 373–383. ISSN: 1431-584X. DOI: `10.1007/BF01323519`. URL: `https://doi.org/10.1007/BF01323519`.

[19] Harvey Brooks. “Ferromagnetic Anisotropy and the Itinerant Electron Model”. In: *Phys. Rev.* 58 (10 Nov. 1940), pp. 909–918. DOI: `10.1103/PhysRev.58.909`. URL: `https://link.aps.org/doi/10.1103/PhysRev.58.909`.

[20] L. F. Yin et al. “Magnetocrystalline Anisotropy in Permalloy Revisited”. In: *Phys. Rev. Lett.* 97 (6 Aug. 2006), p. 067203. DOI: `10.1103/PhysRevLett.97.067203`. URL: `https://link.aps.org/doi/10.1103/PhysRevLett.97.067203`.

[21] Hoffmann F. “Dynamic Pinning Induced by Nickel Layers on Permalloy Films”. In: *physica status solidi (b)* 41.2 (1970), pp. 807–813. DOI: `10.1002/pssb.19700410237`. eprint: `https://onlinelibrary.wiley.com/doi/pdf/10.1002/pssb.19700410237`. URL: `https://onlinelibrary.wiley.com/doi/abs/10.1002/pssb.19700410237`.

[22] Brad N. Engel et al. "Anomalous magnetic anisotropy in ultrathin transition metals". In: *Phys. Rev. B* 48 (13 Oct. 1993), pp. 9894–9897. DOI: `10.1103/PhysRevB.48.9894`. URL: `https://link.aps.org/doi/10.1103/PhysRevB.48.9894`.

[23] Brad N. Engel, Michael H. Wiedmann, and Charles M. Falco. "Overlayer-induced perpendicular anisotropy in ultrathin Co films (invited)". In: *Journal of Applied Physics* 75.10 (1994), pp. 6401–6405. DOI: `10.1063/1.355365`. eprint: `https://doi.org/10.1063/1.355365`. URL: `https://doi.org/10.1063/1.355365`.

[24] A.A. Hirsch, E. Ahilea, and N. Friedman. "Magnetic anisotropy induced by an electric field". In: *Physics Letters A* 28.11 (1969), pp. 763 –764. ISSN: 0375-9601. DOI: `https://doi.org/10.1016/0375-9601(69)90609-4`. URL: `http://www.sciencedirect.com/science/article/pii/0375960169906094`.

[25] Becker R. and Döring W. "Kinetische Behandlung der Keimbildung in übersättigten Dämpfen". In: *Annalen der Physik* 416.8 (1935), pp. 719–752. DOI: `10.1002/andp.19354160806`. eprint: `https://onlinelibrary.wiley.com/doi/pdf/10.1002/andp.19354160806`. URL: `https://onlinelibrary.wiley.com/doi/abs/10.1002/andp.19354160806`.

[26] N. Bukin et al. "Time-resolved imaging of magnetic vortex dynamics using holography with extended reference autocorrelation by linear differential operator". In: *Scientific Reports* 6.August (2016), p. 36307. ISSN: 2045-2322. DOI: `10.1038/srep36307`. URL: `http://www.nature.com/articles/srep36307`.

[27] M. N. Baibich et al. "Giant Magnetoresistance of (001)Fe/(001)Cr Magnetic Superlattices". In: *Physical review letters* 61.001 (21 Nov. 1988), pp. 2472–2475. DOI: `10.1103/PhysRevLett.61.2472`. URL: `https://link.aps.org/doi/10.1103/PhysRevLett.61.2472`.

[28] G. Binasch et al. "Enhanced magnetoresistance in layered magnetic structures with antiferromagnetic interlayer exchange". In: *Phys. Rev. B* 39 (7 Mar. 1989),

pp. 4828–4830. DOI: 10.1103/PhysRevB.39.4828. URL: https://link.aps.org/doi/10.1103/PhysRevB.39.4828.

[29] "The electrical conductivity of transition metals". In: *Proceedings of the Royal Society of London A: Mathematical, Physical and Engineering Sciences* 153.880 (1936), pp. 699–717. ISSN: 0080-4630. DOI: 10.1098/rspa.1936.0031. eprint: http://rspa.royalsocietypublishing.org/content/153/880/699.full.pdf. URL: http://rspa.royalsocietypublishing.org/content/153/880/699.

[30] E. Yu. Tsymbal and D. G. Pettifor. "Effects of band structure and spin-independent disorder on conductivity and giant magnetoresistance in Co/Cu and Fe/Cr multilayers". In: *Phys. Rev. B* 54 (21 Dec. 1996), pp. 15314–15329. DOI: 10.1103/PhysRevB.54.15314. URL: https://link.aps.org/doi/10.1103/PhysRevB.54.15314.

[31] J.C. Slonczewski. "Current-driven excitation of magnetic multilayers". In: *Journal of Magnetism and Magnetic Materials* 159.1-2 (June 1996), pp. L1–L7. ISSN: 03048853. DOI: 10.1016/0304-8853(96)00062-5. URL: http://linkinghub.elsevier.com/retrieve/pii/0304885396000625.

[32] L. Berger. "Emission of spin waves by a magnetic multilayer traversed by a current". In: *Phys. Rev. B* 54 (13 Oct. 1996), pp. 9353–9358. DOI: 10.1103/PhysRevB.54.9353. URL: https://link.aps.org/doi/10.1103/PhysRevB.54.9353.

[33] F. J. Albert et al. "Quantitative Study of Magnetization Reversal by Spin-Polarized Current in Magnetic Multilayer Nanopillars". In: *Phys. Rev. Lett.* 89 (22 Nov. 2002), p. 226802. DOI: 10.1103/PhysRevLett.89.226802. URL: https://link.aps.org/doi/10.1103/PhysRevLett.89.226802.

[34] J.-V. Kim. *Spin-Torque Oscillators*. Vol. 63. 2012, pp. 218–287. DOI: 10.1016/B978-0-12-397028-2.00004-7. URL: http://link.aps.org/doi/10.1103/PhysRevLett.100.257201.

[35] T.J. Silva and W.H. Rippard. “Developments in nano-oscillators based upon spin-transfer point-contact devices”. In: *Journal of Magnetism and Magnetic Materials* 320.7 (2008), pp. 1260 –1271. ISSN: 0304-8853. DOI: `https://doi.org/10.1016/j.jmmm.2007.12.022`. URL: `http://www.sciencedirect.com/science/article/pii/S0304885307010153`.

[36] Andrei Slavin and Vasil Tiberkevich. “Nonlinear auto-oscillator theory of microwave generation by spin-polarized current”. In: *IEEE Transactions on Magnetics* 45.4 (2009), pp. 1875–1918. DOI: `10.1109/TMAG.2008.2009935`.

[37] Klaus D Sattler. “Spin-Transfer Nano-Oscillators 38.1”. In: *Handbook of nanophysics: functional nanomaterials* (2010), pp. 38–1. ISSN: 2040-3364. DOI: `10.1201/9781420075533-45`.

[38] Claas Abert et al. “magnum.fe: A micromagnetic finite-element simulation code based on FEniCS”. In: *Journal of Magnetism and Magnetic Materials* 345 (2013), pp. 29 –35. ISSN: 0304-8853. DOI: `https://doi.org/10.1016/j.jmmm.2013.05.051`. URL: `http://www.sciencedirect.com/science/article/pii/S0304885313004022`.

[39] Claas Abert et al. “A three-dimensional spin-diffusion model for micromagnetics”. In: *Scientific Reports* 5 (Oct. 2015). Article, 14855 EP –. URL: `http://dx.doi.org/10.1038/srep14855`.

[40] M. Tsoi et al. “Excitation of a Magnetic Multilayer by an Electric Current”. In: *Physical Review Letters* 80.19 (May 1998), pp. 4281–4284. ISSN: 0031-9007. DOI: `10.1103/PhysRevLett.80.4281`. URL: `http://link.aps.org/doi/10.1103/PhysRevLett.80.4281`.

[41] Y Ji, C L Chien, and M D Stiles. “Current-induced spin-wave excitations in a single ferromagnetic layer.” In: *Physical review letters* 90.March (2003), p. 106601. ISSN: 0031-9007. DOI: `10.1103/PhysRevLett.90.106601`. arXiv: `0210116 [cond-mat]`.

[42] E. B. Myers et al. “Current-Induced Switching of Domains in Magnetic Multilayer Devices”. In: *Science* 285.5429 (1999), pp. 867–870. ISSN: 00368075. DOI: `10.1126/science.285.5429.867`. URL: `http://www.sciencemag.org/cgi/doi/10.1126/science.285.5429.867`.

[43] W. H. Rippard, M. R. Pufall, and T. J. Silva. “Quantitative studies of spin-momentum-transfer-induced excitations in Co/Cu multilayer films using point-contact spectroscopy”. In: *Applied Physics Letters* 82.8 (2003), pp. 1260–1262. DOI: `10.1063/1.1556168`. eprint: `https://doi.org/10.1063/1.1556168`. URL: `https://doi.org/10.1063/1.1556168`.

[44] J.-E. Wegrowe et al. “Current-induced magnetization reversal in magnetic nanowires”. In: *EPL (Europhysics Letters)* 45.5 (1999), p. 626. URL: `http://stacks.iop.org/0295-5075/45/i=5/a=626`.

[45] J.Z Sun. “Current-driven magnetic switching in manganite trilayer junctions”. In: *Journal of Magnetism and Magnetic Materials* 202.1 (1999), pp. 157 –162. ISSN: 0304-8853. DOI: `https://doi.org/10.1016/S0304-8853(99)00289-9`. URL: `http://www.sciencedirect.com/science/article/pii/S0304885399002899`.

[46] J. A. Katine et al. “Current-Driven Magnetization Reversal and Spin-Wave Excitations in Co /Cu /Co Pillars”. In: *Phys. Rev. Lett.* 84 (14 Apr. 2000), pp. 3149–3152. DOI: `10.1103/PhysRevLett.84.3149`. URL: `https://link.aps.org/doi/10.1103/PhysRevLett.84.3149`.

[47] J. Grollier et al. “Field dependence of magnetization reversal by spin transfer”. In: *Phys. Rev. B* 67 (17 May 2003), p. 174402. DOI: `10.1103/PhysRevB.67.174402`. URL: `https://link.aps.org/doi/10.1103/PhysRevB.67.174402`.

[48] F. B. Mancoff and S. E. Russek. “Spin-current-induced magnetotransport in Co-Cu-Co nanostructures”. In: *IEEE Transactions on Magnetics* 38.5 (Sept. 2002), pp. 2853–2855. ISSN: 0018-9464. DOI: `10.1109/TMAG.2002.802861`.

[49] S. Urazhdin et al. “Current-Driven Magnetic Excitations in Permalloy-Based Multilayer Nanopillars”. In: *Phys. Rev. Lett.* 91 (14 Oct. 2003), p. 146803. DOI: 10.1103/PhysRevLett.91.146803. URL: https://link.aps.org/doi/10.1103/PhysRevLett.91.146803.

[50] K. J. Lee et al. “Spin transfer effect in spin-valve pillars for current-perpendicular-to-plane magnetoresistive heads (invited)”. In: *Journal of Applied Physics* 95.11 (2004), pp. 7423–7428. DOI: 10.1063/1.1682872. eprint: https://doi.org/10.1063/1.1682872. URL: https://doi.org/10.1063/1.1682872.

[51] Yiming Huai et al. “Observation of spin-transfer switching in deep submicron-sized and low-resistance magnetic tunnel junctions”. In: *Applied Physics Letters* 84.16 (2004), pp. 3118–3120. ISSN: 00036951. DOI: 10.1063/1.1707228. arXiv: 0504486 [cond-mat].

[52] Yaowen Liu et al. “Current-induced switching in low resistance magnetic tunnel junctions”. In: *Journal of Applied Physics* 93.10 3 (2003), pp. 8385–8387. ISSN: 00218979. DOI: 10.1063/1.1543868.

[53] G. D. Fuchs et al. “Spin-transfer effects in nanoscale magnetic tunnel junctions”. In: *Applied Physics Letters* 85.7 (2004), pp. 1205–1207. DOI: 10.1063/1.1781769. eprint: https://doi.org/10.1063/1.1781769. URL: https://doi.org/10.1063/1.1781769.

[54] A. Deac et al. “Current driven resistance changes in low resistance x area magnetic tunnel junctions with ultra-thin Al-Oxbarriers”. In: *Journal of Applied Physics* 95.11 II (2004), pp. 6792–6794. ISSN: 00218979. DOI: 10.1063/1.1687533.

[55] V V Kruglyak, S O Demokritov, and D Grundler. “Magnonics”. In: *Journal of Physics D: Applied Physics* 43.26 (2010), p. 260301. URL: http://stacks.iop.org/0022-3727/43/i=26/a=260301.

[56] M. Madami et al. “Direct observation of a propagating spin wave induced by spin-transfer torque”. In: *Nature Nanotechnology* 6 (Aug. 2011), 635 EP –. URL: `http://dx.doi.org/10.1038/nnano.2011.140`.

[57] H. Ulrichs et al. “Spin-torque nano-emitters for magnonic applications”. In: *Applied Physics Letters* 100.16 (2012), p. 162406. DOI: `10.1063/1.4704563`. eprint: `https://doi.org/10.1063/1.4704563`. URL: `https://doi.org/10.1063/1.4704563`.

[58] M. A. Hoefer et al. “Theory of Magnetodynamics Induced by Spin Torque in Perpendicularly Magnetized Thin Films”. In: *Phys. Rev. Lett.* 95 (26 Dec. 2005), p. 267206. DOI: `10.1103/PhysRevLett.95.267206`. URL: `https://link.aps.org/doi/10.1103/PhysRevLett.95.267206`.

[59] Andrei Slavin and Vasil Tiberkevich. “Spin Wave Mode Excited by Spin-Polarized Current in a Magnetic Nanocontact is a Standing Self-Localized Wave Bullet”. In: *Phys. Rev. Lett.* 95 (23 Nov. 2005), p. 237201. DOI: `10.1103/PhysRevLett.95.237201`. URL: `https://link.aps.org/doi/10.1103/PhysRevLett.95.237201`.

[60] S. M. Rezende, F. M. de Aguiar, and A. Azevedo. “Magnon excitation by spin-polarized direct currents in magnetic nanostructures”. In: *Phys. Rev. B* 73 (9 Mar. 2006), p. 094402. DOI: `10.1103/PhysRevB.73.094402`. URL: `https://link.aps.org/doi/10.1103/PhysRevB.73.094402`.

[61] M. R. Pufall et al. “Low-field current-hysteretic oscillations in spin-transfer nanocontacts”. In: *Physical Review B - Condensed Matter and Materials Physics* 75 (2007), pp. 1–4. ISSN: 10980121. DOI: `10.1103/PhysRevB.75.140404`.

[62] V. S. Pribiag et al. “Magnetic vortex oscillator driven by d.c. spin-polarized current”. In: *Nature Physics* 3.7 (May 2007), pp. 498–503. ISSN: 1745-2473. DOI: `10.1038/nphys619`. URL: `http://www.nature.com/doifinder/10.1038/nphys619`.

[63] Q. Mistral et al. "Current-Driven Vortex Oscillations in Metallic Nanocontacts". In: *Physical Review Letters* 100.25 (June 2008), p. 257201. ISSN: 0031-9007. DOI: `10.1103/PhysRevLett.100.257201`. URL: `http://link.aps.org/doi/10.1103/PhysRevLett.100.257201`.

[64] a Dussaux et al. "Large microwave generation from current-driven magnetic vortex oscillators in magnetic tunnel junctions." In: *Nature communications* 1.1 (Jan. 2010), p. 8. ISSN: 2041-1723. DOI: `10.1038/ncomms1006`. URL: `http://www.ncbi.nlm.nih.gov/pubmed/20975671`.

[65] A Ruotolo et al. "Phase-locking of magnetic vortices mediated by antivortices." In: *Nature nanotechnology* 4.8 (Aug. 2009), pp. 528–32. ISSN: 1748-3395. DOI: `10.1038/nnano.2009.143`. URL: `http://www.ncbi.nlm.nih.gov/pubmed/19662017`.

[66] N. Locatelli et al. "Dynamics of two coupled vortices in a spin valve nanopillar excited by spin transfer torque". In: *Applied Physics Letters* 98.6 (2011), p. 062501. DOI: `10.1063/1.3553771`. eprint: `https://doi.org/10.1063/1.3553771`. URL: `https://doi.org/10.1063/1.3553771`.

[67] a. D. Belanovsky et al. "Phase locking dynamics of dipolarly coupled vortex-based spin transfer oscillators". In: *Physical Review B - Condensed Matter and Materials Physics* 85 (2012), pp. 1–4. ISSN: 10980121. DOI: `10.1103/PhysRevB.85.100409`. arXiv: `1202.5499`.

[68] W. H. Rippard et al. "Injection locking and phase control of spin transfer nano-oscillators". In: *Physical Review Letters* 95.6 (2005), pp. 10–13. ISSN: 00319007. DOI: `10.1103/PhysRevLett.95.067203`.

[69] R. Lehndorff et al. "Injection locking of the gyrotropic vortex motion in a nanopillar". In: *Applied Physics Letters* 97 (2010), pp. 30–32. ISSN: 00036951. DOI: `10.1063/1.3498009`.

[70] A. Dussaux et al. “Phase locking of vortex based spin transfer oscillators to a microwave current”. In: *Applied Physics Letters* 98.2011 (2011), pp. 2009–2012. ISSN: 00036951. DOI: `10.1063/1.3565159`. arXiv: `1009.4076`.

[71] Mrigank Sharad, Karthik Yogendra, and Kaushik Roy. “Dual pillar spin torque nano-oscillator”. In: *Applied Physics Letters* 103.15 (2013), p. 152403. DOI: `10.1063/1.4824419`. eprint: `https://doi.org/10.1063/1.4824419`. URL: `https://doi.org/10.1063/1.4824419`.

[72] a. Hamadeh et al. “Perfect and robust phase-locking of a spin transfer vortex nano-oscillator to an external microwave source”. In: *Applied Physics Letters* 104 (2014), pp. 3–6. ISSN: 00036951. DOI: `10.1063/1.4862326`. arXiv: `arXiv:1311.7096v1`.

[73] William Rippard, Matthew Pufall, and Anthony Kos. “Time required to injection-lock spin torque nanoscale oscillators”. In: *Applied Physics Letters* 103.18 (2013), p. 182403. DOI: `10.1063/1.4821179`. eprint: `https://doi.org/10.1063/1.4821179`. URL: `https://doi.org/10.1063/1.4821179`.

[74] William H. Rippard et al. “Spin-transfer dynamics in spin valves with out-of-plane magnetized CoNi free layers”. In: *Physical Review B - Condensed Matter and Materials Physics* 81.1 (2010), pp. 1–8. ISSN: 10980121. DOI: `10.1103/PhysRevB.81.014426`. arXiv: `0911.4077`.

[75] S M Mohseni et al. “Spin Torque – Generated Magnetic Droplet Solitons”. In: *Science* 339.March (2013), p. 1295. DOI: `10.1126/science.1230155`.

[76] M A Hoefer, T J Silva, and Mark W Keller. “Theory for a dissipative droplet soliton excited by a spin torque nanocontact”. In: *Physical Review B - Condensed Matter and Materials Physics* 82.5 (2010), pp. 1–14. DOI: `10.1103/PhysRevB.82.054432`.

[77] B. A. Ivanov and A. M. Kosevich. “Bound states of a large number of magnons in a ferromagnet with a single-ion anisotropy”. In: *Journal of Experimental and Theoretical Physics* 45.5 (1977), p. 1050. URL: http://www.jetp.ac.ru/cgi-bin/e/index/e/45/5/p1050?a=list{\%}5Cnhttp://www.jetp.ac.ru/cgi-bin/r/index/r/72/5/p2000?a=list.

[78] Ferran Macià, Dirk Backes, and Andrew D Kent. “Stable Magnetic Droplet Solitons in Spin Transfer Nanocontacts”. In: *Nature Nanotechnology* 9.12 (2014), pp. 1–19. ISSN: 17483395. DOI: 10.1038/nnano.2014.255. arXiv: 1408.1902. URL: http://arxiv.org/abs/1408.1902.

[79] Ezio Iacocca et al. “Confined dissipative droplet solitons in spin-valve nanowires with perpendicular magnetic anisotropy”. In: *Physical Review Letters* 112.4 (2014), pp. 1–5. DOI: 10.1103/PhysRevLett.112.047201.

[80] S M Mohseni et al. “Magnetic droplet solitons in orthogonal nano-contact spin torque oscillators”. In: *Physica B: Condensed Matter* 435 (2014), pp. 84–87. DOI: 10.1016/j.physb.2013.10.023.

[81] Sergi Lendínez et al. “Observation of droplet soliton drift resonances in a spin-transfer-torque nanocontact to a ferromagnetic thin film”. In: *Physical Review B* 92.17 (2015), p. 174426. DOI: 10.1103/PhysRevB.92.174426. URL: http://link.aps.org/doi/10.1103/PhysRevB.92.174426.

[82] Sunjae Chung et al. “Magnetic droplet solitons in orthogonal spin valves”. In: *Low Temperature Physics* 41.10 (2015), pp. 833–837. DOI: 10.1063/1.4932358. eprint: http://dx.doi.org/10.1063/1.4932358. URL: http://dx.doi.org/10.1063/1.4932358.

[83] P. Wills, E. Iacocca, and M. A. Hoefer. “Deterministic drift instability and stochastic thermal perturbations of magnetic dissipative droplet solitons”. In: *Physical Review B - Condensed Matter and Materials Physics* 93.14 (2016), pp. 1–9. ISSN: 1550235X. DOI: 10.1103/PhysRevB.93.144408. arXiv: 1601.00048.

[84] Sunjae Chung et al. “Magnetic droplet nucleation boundary in orthogonal spin-torque nano-oscillators”. In: *Nature communications* (2016), accepted. DOI: `10.1038/ncomms11209`.

[85] Dun Xiao et al. “Merging droplets in double nanocontact spin torque oscillators”. In: *Phys. Rev. B* 93 (9 Mar. 2016), p. 094431. DOI: `10.1103/PhysRevB.93.094431`. URL: `https://link.aps.org/doi/10.1103/PhysRevB.93.094431`.

[86] D. Xiao et al. “Parametric autoexcitation of magnetic droplet soliton perimeter modes”. In: *Phys. Rev. B* 95 (2 Jan. 2017), p. 024106. DOI: `10.1103/PhysRevB.95.024106`. URL: `https://link.aps.org/doi/10.1103/PhysRevB.95.024106`.

[87] D.V. Slobodianiuk, O.V. Prokopenko, and G.A. Melkov. “Eigenmodes of two-dimensional conservative droplet soliton”. In: *Journal of Magnetism and Magnetic Materials* 439.Supplement C (2017), pp. 144 –147. ISSN: 0304-8853. DOI: `https://doi.org/10.1016/j.jmmm.2017.04.093`. URL: `http://www.sciencedirect.com/science/article/pii/S0304885316306473`.

[88] B. Özyilmaz et al. “Current-Induced Excitations in Single Cobalt Ferromagnetic Layer Nanopillars”. In: *Phys. Rev. Lett.* 93 (17 Oct. 2004), p. 176604. DOI: `10.1103/PhysRevLett.93.176604`. URL: `https://link.aps.org/doi/10.1103/PhysRevLett.93.176604`.

[89] B. Özyilmaz and A. D. Kent. “Current-induced switching in single ferromagenetic layer nanopillar junctions”. In: *Applied Physics Letters* 88.16 (2006), p. 162506. DOI: `10.1063/1.2195780`. eprint: `https://doi.org/10.1063/1.2195780`. URL: `ttps://doi.org/10.1063/1.2195780`.

[90] C. Heide. “Spin Currents in Magnetic Films”. In: *Phys. Rev. Lett.* 87 (19 Oct. 2001), p. 197201. DOI: `10.1103/PhysRevLett.87.197201`. URL: `https://link.aps.org/doi/10.1103/PhysRevLett.87.197201`.

[91] C. Heide, P. E. Zilberman, and R. J. Elliott. "Current-driven switching of magnetic layers". In: *Phys. Rev. B* 63 (6 Jan. 2001), p. 064424. DOI: 10.1103/PhysRevB.63.064424. URL: https://link.aps.org/doi/10.1103/PhysRevB.63.064424.

[92] M L Polianski and P W Brouwer. "Current-induced transverse spin-wave instability in a thin nanomagnet." In: *Physical review letters* 92.January (2004), p. 026602. ISSN: 0031-9007. DOI: 10.1103/PhysRevLett.92.026602.

[93] M. D. Stiles, Jiang Xiao, and A. Zangwill. "Phenomenological theory of current-induced magnetization precession". In: *Phys. Rev. B* 69 (5 Feb. 2004), p. 054408. DOI: 10.1103/PhysRevB.69.054408. URL: https://link.aps.org/doi/10.1103/PhysRevB.69.054408.

[94] Sohrab Redjai Sani et al. "Microwave signal generation in single-layer nano-contact spin torque oscillators". In: *IEEE Transactions on Magnetics* 49.7 (2013), pp. 4331–4334. ISSN: 00189464. DOI: 10.1109/TMAG.2013.2250931.

[95] "Microscopy by reconstructed wave-fronts". In: *Proceedings of the Royal Society of London A: Mathematical, Physical and Engineering Sciences* 197.1051 (1949), pp. 454–487. ISSN: 0080-4630. DOI: 10.1098/rspa.1949.0075. eprint: http://rspa.royalsocietypublishing.org/content/197/1051/454.full.pdf. URL: http://rspa.royalsocietypublishing.org/content/197/1051/454.

[96] Emmett N. Leith and Juris Upatnieks. "Reconstructed Wavefronts and Communication Theory∗". In: *J. Opt. Soc. Am.* 52.10 (Oct. 1962), pp. 1123–1130. DOI: 10.1364/JOSA.52.001123. URL: http://www.osapublishing.org/abstract.cfm?URI=josa-52-10-1123.

[97] Yuri N. Denisyuk. "On the Reflection of optical properties of an object in a wave field of light scattered by it". In: *Doklady Akamedii Nauk SSSR* 6.144 (1962), pp. 1175–1278.

[98] Albert V. Baez. "A Study in Diffraction Microscopy with Special Reference to X-Rays". In: *J. Opt. Soc. Am.* 42.10 (Oct. 1952), pp. 756–762. DOI: `10.1364/JOSA.42.000756`. URL: `http://www.osapublishing.org/abstract.cfm?URI=josa-42-10-756`.

[99] J.T. Winthrop and C.R. Worthington. "X-ray microscopy by successive fourier transformation". In: *Physics Letters* 15.2 (1965), pp. 124 –126. ISSN: 0031-9163. DOI: `https://doi.org/10.1016/0031-9163(65)91304-1`. URL: `http://www.sciencedirect.com/science/article/pii/0031916365913041`.

[100] J.T. Winthrop and C.R. Worthington. "X-ray microscopy by successive Fourier transformation II. An optical analogue experiment". In: *Physics Letters* 21.4 (1966), pp. 413 –415. ISSN: 0031-9163. DOI: `https://doi.org/10.1016/0031-9163(66)90510-5`. URL: `http://www.sciencedirect.com/science/article/pii/0031916366905105`.

[101] G.W. Stroke et al. "Resolution-retrieving compensation of source effects by correlative reconstruction in high-resolution holography". In: *Physics Letters* 18.3 (1965), pp. 274 –275. ISSN: 0031-9163. DOI: `https://doi.org/10.1016/0031-9163(65)90332-X`. URL: `http://www.sciencedirect.com/science/article/pii/003191636590332X`.

[102] Rogers G. L. and Palmer J. "The possibilities of X-ray holographic microscopy". In: *Journal of Microscopy* 89.1 (), pp. 125–135. DOI: `10.1111/j.1365-2818.1969.tb00657.x`. eprint: `https://onlinelibrary.wiley.com/doi/pdf/10.1111/j.1365-2818.1969.tb00657.x`. URL: `https://onlinelibrary.wiley.com/doi/abs/10.1111/j.1365-2818.1969.tb00657.x`.

[103] John W. Giles. "Construction of a Plane-Grating X-Ray Hologram With the Electron Microprobe". In: *J. Opt. Soc. Am.* 59.6 (June 1969), pp. 778–779. DOI: `10.1364/JOSA.59.000778`. URL: `http://www.osapublishing.org/abstract.cfm?URI=josa-59-6-778`.

[104] G. C. Bjorklund, S. E. Harris, and J. F. Young. "Vacuum ultraviolet holography". In: *Applied Physics Letters* 25.8 (1974), pp. 451–452. DOI: `10.1063/1.1655544`. eprint: `https://doi.org/10.1063/1.1655544`. URL: `https://doi.org/10.1063/1.1655544`.

[105] Sadao Aoki and Seishi Kikuta. "X-Ray Holographic Microscopy". In: *Japanese Journal of Applied Physics* 13.9 (1974), p. 1385. URL: `http://stacks.iop.org/1347-4065/13/i=9/a=1385`.

[106] B Reuter and H Mahr. "Experiments with Fourier transform holograms using 4.48 nm X-rays". In: *Journal of Physics E: Scientific Instruments* 9.9 (1976), p. 746. URL: `http://stacks.iop.org/0022-3735/9/i=9/a=017`.

[107] A. M. Kondratenko and A. N. Skrinsky. "Use of radiation of electron storage rings in x-ray holography of objects". In: *Optics and Spectroscopy* 42 (Feb. 1977), pp. 189–192.

[108] Malcolm Howells and Janos Kirz. "Coherent soft x-rays in high resolution imaging". In: *AIP Conference Proceedings* 118.1 (1984), pp. 85–95. DOI: `10.1063/1.34649`. eprint: `https://aip.scitation.org/doi/pdf/10.1063/1.34649`. URL: `https://aip.scitation.org/doi/abs/10.1063/1.34649`.

[109] David Attwood and Anne Sakdinawat. "Introduction". In: *X-Rays and Extreme Ultraviolet Radiation: Principles and Applications*. 2nd ed. Cambridge University Press, 2017, 1–26. DOI: `10.1017/9781107477629.004`.

[110] V V Lider. "X-ray holography". In: *Physics-Uspekhi* 58.4 (2015), pp. 365–383. ISSN: 1063-7869. DOI: `10.3367/UFNe.0185.201504d.0393`. URL: `http://stacks.iop.org/1063-7869/58/i=4/a=365?key=crossref.8e768ddf86062703df3b83ddd0028f90`.

[111] Jorge Garcia-Sucerquia et al. "Digital in-line holographic microscopy". In: *Appl. Opt.* 45.5 (Feb. 2006), pp. 836–850. DOI: `10.1364/AO.45.000836`. URL: `http://ao.osa.org/abstract.cfm?URI=ao-45-5-836`.

[112] Tatiana Latychevskaia and Hans-Werner Fink. "Solution to the Twin Image Problem in Holography". In: *Phys. Rev. Lett.* 98 (23 June 2007), p. 233901. DOI: `10.1103/PhysRevLett.98.233901`. URL: `https://link.aps.org/doi/10.1103/PhysRevLett.98.233901`.

[113] Anne-Sophie Morlens et al. "Submicrometer digital in-line holographic microscopy at 32 nm with high-order harmonics". In: *Opt. Lett.* 31.21 (Nov. 2006), pp. 3095–3097. DOI: `10.1364/OL.31.003095`. URL: `http://ol.osa.org/abstract.cfm?URI=ol-31-21-3095`.

[114] N. Watanabe et al. "Soft-x-ray Gabor holography by use of a backilluminated CCD camera". In: *Appl. Opt.* 36.29 (Oct. 1997), pp. 7433–7436. DOI: `10.1364/AO.36.007433`. URL: `http://ao.osa.org/abstract.cfm?URI=ao-36-29-7433`.

[115] Norio Watanabe and Sadao Aoki. "Three-dimensional tomography using a soft X-ray holographic microscope and CCD camera". In: *Journal of Synchrotron Radiation* 5.3 (May 1998), pp. 1088–1089. DOI: `10.1107/S0909049597018943`. URL: `https://doi.org/10.1107/S0909049597018943`.

[116] T. Gorniak et al. "X-ray holographic microscopy with zone plates applied to biological samples in the water window using 3rd harmonic radiation from the free-electron laser FLASH". In: *Opt. Express* 19.12 (June 2011), pp. 11059–11070. DOI: `10.1364/OE.19.011059`. URL: `http://www.opticsexpress.org/abstract.cfm?URI=oe-19-12-11059`.

[117] R. Heine et al. "Digital in-line X-ray holography with zone plates". In: *Ultramicroscopy* 111.8 (2011), pp. 1131 –1136. ISSN: 0304-3991. DOI: `https://doi.org/10.1016/j.ultramic.2011.02.002`. URL: `http://www.sciencedirect.com/science/article/pii/S0304399111000702`.

[118] Jun Lim, Hyun Joon Shin, and Chung Ki Hong. "High-Resolution Soft X-ray Digital In-Line Holographic Microscopy". In: *Japanese Journal of Applied Physics*

50.7R (2011), p. 072504. URL: http://stacks.iop.org/1347-4065/50/i=7R/a=072504.

[119] A. Rosenhahn et al. "Vacuum-ultraviolet Gabor holography with synchrotron radiation". In: *Ultramicroscopy* 107.12 (2007), pp. 1171 –1177. ISSN: 0304-3991. DOI: https://doi.org/10.1016/j.ultramic.2007.01.010. URL: http://www.sciencedirect.com/science/article/pii/S0304399107000186.

[120] Axel Rosenhahn et al. "Digital In-line Holography with femtosecond VUV radiation provided by the free-electron laser FLASH". In: *Opt. Express* 17.10 (May 2009), pp. 8220–8228. DOI: 10.1364/OE.17.008220. URL: http://www.opticsexpress.org/abstract.cfm?URI=oe-17-10-8220.

[121] Ruth Barth et al. "Soft X-ray holographic microscopy of chromosomes with high aspect ratio pinholes". In: *Journal of Biotechnology* 149.4 (2010). BioImaging - Contributions from Biology, Physics and Informatics, pp. 238 –242. ISSN: 0168-1656. DOI: https://doi.org/10.1016/j.jbiotec.2010.03.017. URL: http://www.sciencedirect.com/science/article/pii/S0168165610001628.

[122] M Howells et al. "X-ray holograms at improved resolution: a study of zymogen granules". In: *Science* 238.4826 (1987), pp. 514–517. ISSN: 0036-8075. DOI: 10.1126/science.3659925. eprint: http://science.sciencemag.org/content/238/4826/514.full.pdf. URL: http://science.sciencemag.org/content/238/4826/514.

[123] Chris Jacobsen et al. "X-ray holographic microscopy using photoresists". In: *J. Opt. Soc. Am. A* 7.10 (Oct. 1990), pp. 1847–1861. DOI: 10.1364/JOSAA.7.001847. URL: http://josaa.osa.org/abstract.cfm?URI=josaa-7-10-1847.

[124] C. Fuhse, C. Ollinger, and T. Salditt. "Waveguide-Based Off-Axis Holography with Hard X Rays". In: *Phys. Rev. Lett.* 97 (25 Dec. 2006), p. 254801. DOI: 10.1103/PhysRevLett.97.254801. URL: https://link.aps.org/doi/10.1103/PhysRevLett.97.254801.

[125] Yoshiki Kohmura et al. “Phase retrieval with two-beam off-axis x-ray holography”. In: *Journal of Applied Physics* 96.4 (2004), pp. 1781–1784. DOI: `10.1063/1.1769098`. eprint: `https://doi.org/10.1063/1.1769098`. URL: `https://doi.org/10.1063/1.1769098`.

[126] S. Eisebitt et al. “Lensless imaging of magnetic nanostructures by X-ray spectro-holography”. In: *Nature* 432 (Dec. 2004), 885 EP –. URL: `http://dx.doi.org/10.1038/nature03139`.

[127] K. Nomura et al. “Development of Scanning-Type X-ray Fourier Transform Holography”. In: *AIP Conference Proceedings* 1365.1 (2011), pp. 277–280. DOI: `10.1063/1.3625358`. eprint: `https://aip.scitation.org/doi/pdf/10.1063/1.3625358`. URL: `https://aip.scitation.org/doi/abs/10.1063/1.3625358`.

[128] W. F. Schlotter et al. “Multiple reference Fourier transform holography with soft x rays”. In: *Applied Physics Letters* 89.16 (2006), p. 163112. DOI: `10.1063/1.2364259`. eprint: `https://doi.org/10.1063/1.2364259`. URL: `https://doi.org/10.1063/1.2364259`.

[129] Lorenz-M. Stadler et al. “Hard X Ray Holographic Diffraction Imaging”. In: *Phys. Rev. Lett.* 100 (24 June 2008), p. 245503. DOI: `10.1103/PhysRevLett.100.245503`. URL: `https://link.aps.org/doi/10.1103/PhysRevLett.100.245503`.

[130] In: ().

[131] Janos Kirz et al. “X-ray Microscopy with the NSLS Soft X-ray Undulator”. In: *Physica Scripta* 1990.T31 (1990), p. 12. URL: `http://stacks.iop.org/1402-4896/1990/i=T31/a=001`.

[132] Ian McNulty et al. “High-Resolution Imaging by Fourier Transform X-ray Holography”. In: *Science* 256.5059 (1992), pp. 1009–1012. ISSN: 0036-8075. DOI: `10.1126/science.256.5059.1009`. URL: `http://science.sciencemag.org/sci/`

256/5059/1009.full.pdf{\%}5Cnhttp://science.sciencemag.org/content/256/5059/1009.

[133] Wolfram Leitenberger and Anatoly Snigirev. “Microscopic imaging with high energy x-rays by Fourier transform holography”. In: *Journal of Applied Physics* 90.2 (2001), pp. 538–544. DOI: 10.1063/1.1378810. eprint: https://doi.org/10.1063/1.1378810. URL: https://doi.org/10.1063/1.1378810.

[134] Thomas a. Duckworth et al. “Magnetic imaging by x-ray holography using extended references”. In: *Optics Express* 19.17 (2011), p. 16223.

[135] Manuel Guizar-Sicairos and James R Fienup. “Holography with extended reference by autocorrelation linear differential operation.” In: *Optics express* 15.26 (2007), pp. 17592–17612. ISSN: 1094-4087. DOI: 10.1364/OE.15.017592.

[136] Diling Zhu et al. “High-resolution X-ray lensless imaging by differential holographic encoding”. In: *Physical Review Letters* 105.4 (2010), pp. 1–4. ISSN: 00319007. DOI: 10.1103/PhysRevLett.105.043901.

[137] H. Ade and B. Hsiao. “X-ray Linear Dichroism Microscopy”. In: *Science* 262.5138 (1993), pp. 1427–1429. ISSN: 0036-8075. DOI: 10.1126/science.262.5138.1427. eprint: http://science.sciencemag.org/content/262/5138/1427.full.pdf. URL: http://science.sciencemag.org/content/262/5138/1427.

[138] P Fischer et al. “Magnetic domain imaging with a transmission X-ray microscope”. In: *Journal of Magnetism and Magnetic Materials* 198-199 (1999), pp. 624 –627. ISSN: 0304-8853. DOI: https://doi.org/10.1016/S0304-8853(98)01210-4. URL: http://www.sciencedirect.com/science/article/pii/S0304885398012104.

[139] Gerrit van der Laan and Adriana I. Figueroa. “X-ray magnetic circular dichroism—A versatile tool to study magnetism”. In: *Coordination Chemistry Reviews* 277-278 (2014). Following Chemical Structures using Synchrotron Radiation,

pp. 95 –129. ISSN: 0010-8545. DOI: https://doi.org/10.1016/j.ccr.2014.03.018. URL: http://www.sciencedirect.com/science/article/pii/S0010854514000733.

[140] Joseph W Goodman. "Introduction to Fourier optics". In: *Introduction to Fourier optics, 3rd ed., by JW Goodman. Englewood, CO: Roberts & Co. Publishers, 2005* 1 (2005).

[141] H. He et al. "Use of extended and prepared reference objects in experimental Fourier transform x-ray holography". In: *Applied Physics Letters* 85.13 (2004), pp. 2454–2456. DOI: 10.1063/1.1795360. eprint: https://doi.org/10.1063/1.1795360. URL: https://doi.org/10.1063/1.1795360.

[142] M.R. Howells et al. "Toward a practical X-ray Fourier holography at high resolution". In: *Nuclear Instruments and Methods in Physics Research Section A: Accelerators, Spectrometers, Detectors and Associated Equipment* 467-468 (2001). Proceedings of the 7th Int. Conf. on Synchrotron Radiation Instru mentation, pp. 864 –867. ISSN: 0168-9002. DOI: https://doi.org/10.1016/S0168-9002(01)00498-3. URL: http://www.sciencedirect.com/science/article/pii/S0168900201004983.

[143] R. N. Bracewell. *The Fourier Transform and ITs Applications*. 2nd ed. New York: McGraw-Hill, 1978. ISBN: 007007013X.

[144] S. Streit-Nierobisch et al. "Magnetic soft x-ray holography study of focused ion beam-patterned Co/Pt multilayers". In: *Journal of Applied Physics* 106.8 (2009), p. 083909. DOI: 10.1063/1.3246724. eprint: https://doi.org/10.1063/1.3246724. URL: https://doi.org/10.1063/1.3246724.

[145] J. Wu, J.R. Moore, and R.J. Hicken. "Optical pump-probe studies of the rise and damping of ferromagnetic resonance oscillations in a thin Fe film". In: *Journal of Magnetism and Magnetic Materials* 222.1 (2000), pp. 189 –198. ISSN: 0304-8853.

DOI: https://doi.org/10.1016/S0304-8853(00)00537-0. URL: http://www.sciencedirect.com/science/article/pii/S0304885300005370.

[146] K. H. Bennemann. *Nonlinear Optics in Metals*. Oxford University Press, 1998. ISBN: 9780198518938. URL: https://www.bookdepository.com/book/9780198518938.

[147] P. S. Keatley. *Time-Resolved Magneto-Optical Investigations of Picosecond Magnetisation Dynamics in Arrays of Non-Ellipsoidal Ferromagnetic Nano-Elements*. Ph. D. thesis, University of Exeter, 2008. URL: http://hdl.handle.net/10036/33692.

[148] Paul Steven Keatley et al. "Imaging magnetisation dynamics in nano-contact spin-torque vortex oscillators exhibiting gyrotropic mode splitting". In: *Journal of Physics D: Applied Physics* 50.16 (2017), p. 164003. URL: http://stacks.iop.org/0022-3727/50/i=16/a=164003.

[149] Ye. Pogoryelov et al. "Spin-torque oscillator linewidth narrowing under current modulation". In: *Applied Physics Letters* 98.19 (2011), p. 192506. DOI: 10.1063/1.3588038. eprint: https://doi.org/10.1063/1.3588038. URL: https://doi.org/10.1063/1.3588038.

[150] Ye. Pogoryelov et al. "Frequency modulation of spin torque oscillator pairs". In: *Applied Physics Letters* 98.19 (2011), p. 192501. DOI: 10.1063/1.3588218. eprint: https://doi.org/10.1063/1.3588218. URL: https://doi.org/10.1063/1.3588218.

[151] Sebastien Petit-Watelot et al. "Commensurability and chaos in magnetic vortex oscillations". English. In: *Nature Physics* 8.9 (Sept. 2012), pp. 682–687. ISSN: 1745-2473. DOI: 10.1038/nphys2362.

[152] D. V. Berkov and N. L. Gorn. "Spin-torque driven magnetization dynamics in a nanocontact setup for low external fields: Numerical simulation study". In: *Phys. Rev. B* 80 (6 Aug. 2009), p. 064409. DOI: 10.1103/PhysRevB.80.064409. URL: https://link.aps.org/doi/10.1103/PhysRevB.80.064409.

[153] Thomas A. Duckworth et al. "Holographic imaging of interlayer coupling in Co/Pt/NiFe". In: *New Journal of Physics* 15 (2013). ISSN: 13672630. DOI: `10.1088/1367-2630/15/2/023045`.

[154] Gino Hrkac et al. "Magnetic vortex oscillators". In: *Journal of Physics D: Applied Physics* 48.45 (2015), p. 453001. URL: `http://stacks.iop.org/0022-3727/48/i=45/a=453001`.

[155] M. L. Polianski and P. W. Brouwer. "Current-Induced Transverse Spin-Wave Instability in a Thin Nanomagnet". In: *Phys. Rev. Lett.* 92 (2 Jan. 2004), p. 026602. DOI: `10.1103/PhysRevLett.92.026602`. URL: `https://link.aps.org/doi/10.1103/PhysRevLett.92.026602`.

[156] D Backes et al. "Direct Observation of a Localized Magnetic Soliton in a Spin-Transfer Nanocontact". In: *Physical Review Letters* 115.12 (2015), pp. 1–5. DOI: `10.1103/PhysRevLett.115.127205`.

[157] S. Bonetti et al. "Direct observation and imaging of a spin-wave soliton with $p-$like symmetry". In: *Nature communications* 6.May (2015), pp. 1–6. ISSN: 2041-1723. DOI: `10.1038/ncomms9889`. arXiv: `1504.0144`. URL: `http://arxiv.org/abs/1504.0144`.

[158] Sunjae Chung et al. "Direct observation of magnetic droplet solitons in all-perpendicular spin torque nano-oscillators". In: *eprint arXiv:1707.01595*. July 2017.

[159] S M Mohseni et al. "High frequency operation of a spin-torque oscillator at low field". In: *Physica Status Solidi - Rapid Research Letters* 5.12 (2011), pp. 432–434. DOI: `10.1002/pssr.201105375`.

[160] C. Tieg et al. "Imaging the in-plane magnetization in a Co microstructure by Fourier transform holography". In: *Opt. Express* 18.26 (Dec. 2010), pp. 27251–

27256. DOI: `10.1364/OE.18.027251`. URL: `http://www.opticsexpress.org/abstract.cfm?URI=oe-18-26-27251`.

[161] S. Kaka et al. “Mutual phase-locking of microwave spin torque nano-oscillators”. In: *Nature* 437.September (2005), p. 4. ISSN: 0028-0836. DOI: `10.1109/INTMAG.2006.375411`.

[162] Qiyuan Zhu et al. “Phase locking of moving magnetic vortices in bridge-coupled nanodisks”. In: *Journal of Applied Physics* 117.17 (2015), pp. 0–7. ISSN: 10897550. DOI: `10.1063/1.4919749`. URL: `http://dx.doi.org/10.1063/1.4919749`.

[163] Martin Kreissig et al. “Vortex spin-torque oscillator stabilized by phase locked loop using integrated circuits”. In: *AIP Advances* 7.5 (2017), p. 056653. DOI: `10.1063/1.4976337`. eprint: `https://doi.org/10.1063/1.4976337`. URL: `https://doi.org/10.1063/1.4976337`.

[164] W. K. Hiebert, A. Stankiewicz, and M. R. Freeman. “Direct Observation of Magnetic Relaxation in a Small Permalloy Disk by Time-Resolved Scanning Kerr Microscopy”. In: *Phys. Rev. Lett.* 79 (6 Aug. 1997), pp. 1134–1137. DOI: `10.1103/PhysRevLett.79.1134`. URL: `https://link.aps.org/doi/10.1103/PhysRevLett.79.1134`.

[165] P. S. Keatley et al. “Magneto-optical observation of mutual phase-locking in a pair of spin-torque vortex oscillators”. In: *2015 IEEE Magnetics Conference (INTERMAG)*. May 2015, pp. 1–1. DOI: `10.1109/INTMAG.2015.7156846`.

[166] P. S. Keatley et al. “Direct observation of magnetization dynamics generated by nanocontact spin-torque vortex oscillators”. In: *Phys. Rev. B* 94 (6 Aug. 2016), p. 060402. DOI: `10.1103/PhysRevB.94.060402`. URL: `https://link.aps.org/doi/10.1103/PhysRevB.94.060402`.

[167] P. S. Keatley et al. “Superharmonic injection locking of nanocontact spin-torque vortex oscillators”. In: *Phys. Rev. B* 94 (9 Sept. 2016), p. 094404. DOI: `10.1103/`

PhysRevB.94.094404. URL: https://link.aps.org/doi/10.1103/PhysRevB.94.094404.

[168] P. S. Keatley et al. “Bottom up Magnonics: Magnetization Dynamics of Individual Nanomagnets”. In: *Magnonics: From Fundamentals to Applications*. Ed. by Sergej O. Demokritov and Andrei N. Slavin. Berlin, Heidelberg: Springer Berlin Heidelberg, 2013, pp. 17–28. ISBN: 978-3-642-30247-3. DOI: 10.1007/978-3-642-30247-3_2. URL: https://doi.org/10.1007/978-3-642-30247-3_2.

[169] TRÄGÅRDH J. et al. “A simple but precise method for quantitative measurement of the quality of the laser focus in a scanning optical microscope”. In: *Journal of Microscopy* 259.1 (), pp. 66–73. DOI: 10.1111/jmi.12249. eprint: https://onlinelibrary.wiley.com/doi/pdf/10.1111/jmi.12249. URL: https://onlinelibrary.wiley.com/doi/abs/10.1111/jmi.12249.

[170] O. V. Sukhostavets et al. “Probing the Anharmonicity of the Potential Well for a Magnetic Vortex Core in a Nanodot”. In: *Phys. Rev. Lett.* 111 (24 2013), p. 247601. DOI: 10.1103/PhysRevLett.111.247601. URL: https://link.aps.org/doi/10.1103/PhysRevLett.111.247601.

[171] G. Hrkac et al. “Magnetic Vortex Core Oscillations in Multi Point Contact Spin Valve Stacks”. In: *IEEE Transactions on Magnetics* 48.11 (2012), pp. 3811–3813. ISSN: 0018-9464. DOI: 10.1109/TMAG.2012.2195301.

[172] David Serrate et al. “Imaging and manipulating the spin direction of individual atoms”. In: *Nature Nanotechnology* 5 (2010), 350 EP –. URL: http://dx.doi.org/10.1038/nnano.2010.64.

[173] Andreas Ehn et al. “FRAME: femtosecond videography for atomic and molecular dynamics”. In: *Light: Science &Amp; Applications* 6 (2017). Original Article, e17045 EP –. URL: http://dx.doi.org/10.1038/lsa.2017.45.